The Thermal and Hydrodynamic Behaviour of Submerged and Confined, Normally-Impinging, Laminar Slot Jets

UNIVERSITY *of* LIMERICK

OLLSCOIL LUIMNIGH

Andrew Sexton, BEng (Hons) Mech. Eng.

CONNECT, Stokes Laboratories

School of Engineering

Faculty of Science and Engineering

University of Limerick

Supervisors

Dr. Jeff Punch & Dr. Nicholas Jeffers

Submitted to the University of Limerick for the degree of

Doctor of Philosophy (PhD)

2017

Declaration

The substance of this thesis is the original work of the author, and due reference and acknowledgement has been made, where necessary, to the work of others. No part of this thesis has been submitted in candidature for any degree. Limerick, 2017.

Andrew Sexton (Candidate)

Dr. Jeff Punch (Supervisor)

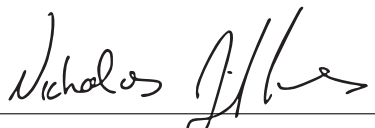

Dr. Nicholas Jeffers (Supervisor)

This thesis was defended on the 3^{rd} of May 2017.

Examination Committee

Chairman	Prof. Jeremy Robinson	University of Limerick
External Examiner	Dr. Jon Summers	University of Leeds
Internal Examiner	Dr. Pat Walsh	University of Limerick

Abstract

Optical networks are a critical element of contemporary communications infrastructure, due to their efficacy in transmitting high-speed data over large distances. Photonic integrated circuits (PICs) offer compelling advantages in terms of performance and miniaturization, but increasing the power density of these components, coupled with shrinking packaging footprint, presents a significant thermal management challenge. This has driven the need for the integration of liquid-based microfluidic cooling artefacts into next generation PIC packages. Liquid microjets are emerging as a candidate primary or secondary heat exchanger for such packages, however, the thermal-hydraulic behaviour of confined, low Reynolds number liquid slot jets is not comprehensively understood. The objective of this thesis is to characterise the influence of slot jet geometry modifications as a technique for the passive control and enhancement of single-phase convective heat transfer.

The slot jets investigated featured five different nozzle aspect ratios (L/W), and five different passive outlet structures in the form of tabs and chevrons. The investigation was carried out for slot jets in the laminar flow regime, over a Reynolds number range of $100 \leq Re_{Dh} \leq 500$ – and with a fixed confinement height to hydraulic diameter ratio (H/D_h) of 1. Particle - Image Velocimetry (PIV) and an isoflux foil technique were utilised to identify the fluidic mechanisms associated with each geometry and to understand their corresponding influence on the spatial temperature distributions along the heated surface. The hydrodynamic penalty of any enhancements in heat transfer achieved were then determined through the measurement of the pressure drop across each nozzle geometry.

It was found that increasing the jet nozzle aspect ratio from 1 to 8 resulted in enhancements in area-averaged Nusselt number (Nu_{Avg}) of up to 68%, and a corresponding decrease in head loss coefficient (K) of 12%. Within the stagnation zone, correlations extrapolated from the experimental results showed that the stagnation point Nusselt number (Nu_0) had a very weak dependency on the jet nozzle aspect ratio, but scaled with $Re_{Dh}^{0.55}$. This Reynolds number scaling was indicative of the potential core of the jet striking the impingement surface. Off-center peaks observed in the velocity flow fields of the impinging jets were postulated to be as a result of the stagnation zone fluid dynamics and local flow entrainment. When compared to the baseline case, all outlet tab geometries resulted in increased local and area-averaged heat transfer and, for the same pumping power, enhancements in Nu_{Avg} of up to 29% were achieved through the application of the major triangle outlet tab geometry. It was also determined that the geometry and location of the outlet tabs were found to influence the local heat transfer coefficients within both the stagnation and wall jet zones. It was concluded that the passive control and enhancement of an integrated microjet cooling solution could be achieved through geometry modification – without compromising the stringent design constraints of an integrated microfluidic package, such as confinement height, flow rate, and the required pumping power.

Acknowledgments

Firstly, I would like to extend my sincere gratitude to my supervisors, Dr. Jeff Punch, Dr. Nicholas Jeffers, and Dr. Jason Stafford, for allowing me the opportunity to pursue this research. Your knowledge and support was appreciated throughout the whole experience.

To all the staff of the Stokes Laboratories who I had the pleasure of working with, especially Paddy O'Regan and Fionnuala O'Connell, who are both embodiments of what makes Stokes Laboratories such a great place to work. To the many people who were members of the lunch groups over the years, such as Declan, Tim, Ciaran, Valeria, Betta, John, Michael, Padraic, Anthony, Jerry, Anne, Jane, Finola and Lisa. Those lunches always offered an entertaining release during some tough days, and I learned a lot during some of our stimulating conversations – not all of it useful knowledge, but always fact checked!

To my parents, Liam and Yvonne, I would like to thank you so much for your unwavering support with every venture we were interested in growing up – from the highs (finishing the mini) to the lows (failed attempt at learning guitar), your encouragement will never be forgotten. To my brothers Brian and David, and my uncles Stepehen and Richard, whose enquiries into my research and messages of support were always appreciated and never taken for granted. To all my friends and members of the Gluepot, I would like to thank you for being such great people and always supporting one another. We've created memories of some brilliant trips and nights out, and hopefully many more to come.

Finally, to Leanne, whose love and support got me through this whole endeavour with my sanity intact. You were always there for the many stressful days, and offered unending optimism and encouragement. You are a wonderful and inspiring person, and I look forward to our many adventures together.

To my parents, Liam and Yvonne, and my girlfriend Leanne, for all your support and belief

Contents

List of Tables

List of Figures

Nomenclature

Roman		**Units**
A	Area	m^2
D	Diameter	mm
D_h	Hydraulic diameter	mm
E	Error	-
H	Height	mm
h	heat transfer coefficient	W/m^2K
I	Current	A
K	Head loss coefficient	-
k	Thermal conductivity	W/mK
L	Length	mm
M	Mesh size	mm
N	Number of samples	-
Nu	Nusselt number	-
Pr	Prandtl number	-
$\dot{q}$	Heat flux	W/m^2
R	Derived experimental variable	-
Re	Reynolds number	-

R_{th}	Thermal resistance	°C/W
r	Radial distance	mm
T	Temperature	°C, K
t	Thickness	mm
t	Time	s
U	Velocity magnitude	mm/s
u,v,w	Instantaneous velocity	mm/s
V	Voltage	V
$\dot{V}$	Volumetric flow rate	m^3/s
W	Width	mm
x,y,z	Distance	mm
Greek		**Units**
β	Open area ratio	-
Δ	Change	–
δ	Boundary layer thickness	
μ	Dynamic viscosity	kg/sm
ξ	Porosity	-
ρ	Density	kg/m^3
σ	Stefan-Boltzman constant	W/m^2K^4
τ	Transmissivity	-
ω	Uncertainty	
Subscripts		
c	Conduction	-
cv	Convection	-

f	Foil	-
in	Input	-
lc	Lateral conduction	-
Max	Maximum	-
nc	Natural convection	-
p	Paint	-
px	pixel	-
R	Residual	-
ref	Statistical reference	-
W	Wall	-
0	Stagnation point	

Acronyms

ABS	Acrylonitrile Butadiene Styrene	-
CCD	Charged Coupled Device	-
CFD	Computational Fluid Dynamics	-
CMOS	Complimentary Metal Oxide Semiconductor	-
FFT	Fast Fourier Transform	-
IC	Integrated Circuits	-
IP	Internet Protocol	-
IR	Infrared	-
IoT	Internet of Things	-
PIC	Photonic Integrated Circuit	-
PIV	Particle – Image Velocimetry	-
SEM	Scanning Electron Microscope	-

TEC	Thermoelectric Cooler	-
TIM	Thermal Interface Material	-
TIPS	Thermally Integrated Photonics System	-
ZB	Zetabyte	-

Chapter 1

Introduction

This chapter introduces the motivations behind the work of this thesis, by outlining the demands facing the contemporary telecommunications industry. This is then followed by the introduction of a research topic with the potential to address some of the challenges concerning the introduction of next-generation telecommunication networks. The chapter will then conclude by outlining the role of this thesis within the research topic, as well as providing the primary objectives and thesis structure.

1.1 Motivations

The commercialization of the telephone and the establishment of the first telecommunication networks has seen society embark on a rapid path of cultural and economic development. This growth has seen the introduction of many new forms of media (radio, television, Internet), and the progression towards an informational society – as our interconnected world continues to embrace the globalisation nurtured by widespread access to telecommunication networks. However, with this, a data dependent culture has developed, and technological innovations in the health, finance and education sectors are becoming increasingly reliant on the availability of information sharing, and accelerated data processing. As a consequence, global markets and societal development have become intertwined with the efficiency of the worldwide telecommunications infrastructure.

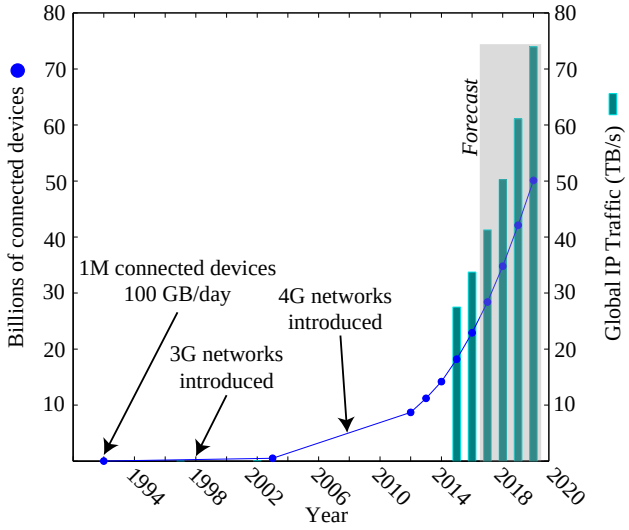

Figure 1.1: Actual and projected growth of global IP traffic (TB/s) and in the number of network connected devices between 1990 and 2020 [1; 2; 3].

Figure 1.1 illustrates the actual and forecast growth of both global IP traffic and connected devices between 1990 and 2020 [1; 2; 3]. It can be seen that the global demand for data is growing at a substantial annual rate, and this is predominantly due to the rapid growth in the number of consumer electronic devices such as smart phones, tablets and more recently, wearable devices – coupled with the emergence of new technologies in the form of the Internet of Things (IoT), cloud computing, and 4K video streaming. We have now entered what researchers are referring to as the 'Zetabyte Era' [2], with current projections showing that global Internet traffic will grow from 1.1 ZB per year ($1.1x10^{12}GB$) at the end of 2016, to 2.3 ZB per year by 2020. Concurrently, there will also be a substantial rise in the number of network connected devices, with recent projections forecasting as many as 50 billion by 2020, which will account for approximately 66% of the annual global IP traffic [2]. These numbers are only set to rise even further, with 5th generation mobile broadband (5G) set to roll out fully by 2020 [9].

As a result of this growth, global telecommunications networks are under continuous strain to meet the current and projected requirements. Consumer needs will surpass the network capacity, and performance improvements in technology will be impeded, unless the network capability begins to evolve at a rate greater

than or equalling demand. The development and maintenance of telecommunication networks represents a multi-scaled problem: from the large ships laying undersea fibre-optic cables which traverse the globe, to the microscale lasers at the source of the signal generation. Despite this difference in scale, it is well acknowledged that each component in the network hierarchy must undergo a significant evolution in efficiency, scale, and cost, in order to meet the projected data demands.

1.2 Photonic Integrated Circuits

One research topic which aims to achieve the necessary jump in demand capability, is the development of Photonic Integrated Circuits (PICs). PICs are the integration of multiple photonic functions into one package, and their primary application is in the field of fibre-optic communication. It is the efficient nature of PICs in transmitting data optically over large distances that has lead to their potential in meeting future demands. PIC packages are located at the source of the signal transmission, with current state-of-the-art systems comprising four packaging levels, detailed in Figure 1.2.

- ***Level 1***: This is the PIC itself, consisting of the active photonics, or laser-bars, which generate the transmitted signal. Currently these are manufactured out of III-V materials, such as Indium Phosphide. Each laser has a rated heat dissipation of approximately 100mW, but given their scale (10^{-6}m), they produce resultant heat fluxes in the order of $1kW/cm^2$. To achieve the required component miniaturization for next generation PIC packages, it is necessary to reduce the spacing between each laser (currently at 250μm [4]), resulting in further increases in device level heat fluxes. However, the thermal management of the photonic devices have much more stringent requirements when compared to the electronic components, as they must be maintained to a tolerance of within $\pm$0.1K of their operational temperature. Any fluctuation outside of this limit will result in a wavelength shift, causing a communication breakdown between incoming data and the receiver.

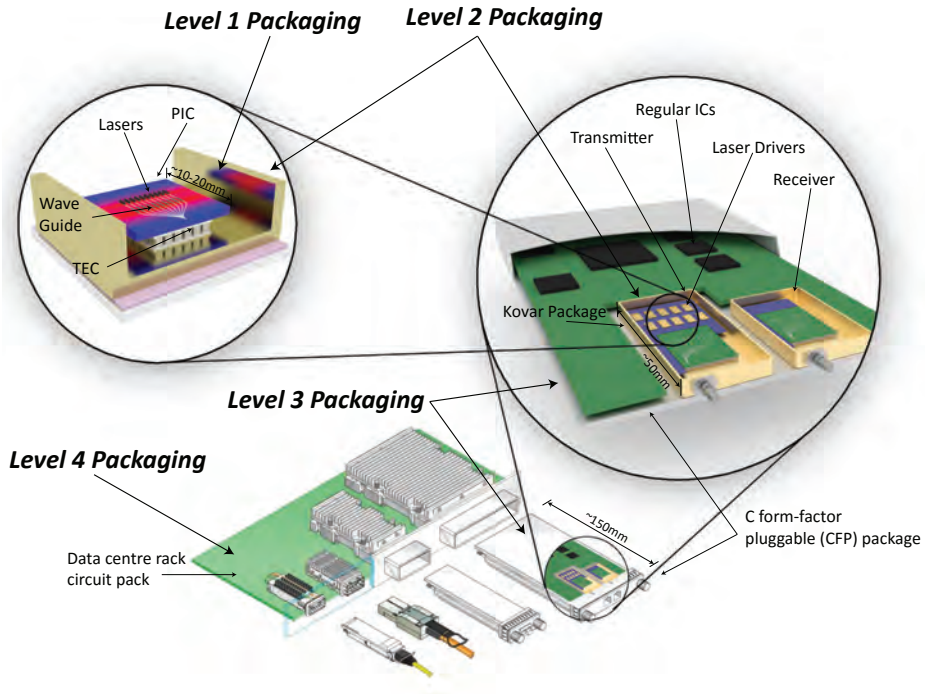

Figure 1.2: Illustration depicting the hierarchy of PIC packaging. [4]

- ***Level 2***: The level 2 packaging contains the optoelectronic device, with the active photonics placed on top of a thermoelectric cooler (TEC) and housed in a Kovar package. Resistive heaters are deposited in close proximity to the laser-bars, and coupled with the macro TECs, to allow for the required tuning of the lasers to their desired operational temperatures. The Kovar package also includes ancillary components such as the electronic ICs necessary to drive the lasers (thermally bonded to the package walls and wire bounded to the active photonics), and passive photonic components such as multiplexers, lenses and fibre-optic connections.

- ***Level 3***: For the third level of packaging, the Kovar packaged transmitter is combined with an optical receiver, and all necessary operational IC packages, into a C form factor pluggable (CFP) package.

- ***Level 4***: The fourth level allows for all preceding levels to be connected, via the pluggable CFP, into the circuit pack located in a data centre rack.

Conventional back-side heat removal strategies, such as heat sinks, air cooling and micro-channel cold-plates, are currently implemented to remove the thermal energy from these circuit packs. However, due to these strategies approaching their scaling and operational limits, they are proving to be unsuitable for the required package miniaturization.

In order to achieve the required evolution in the efficiency of next-generation PICs, it is necessary to increase the number of lasers within the arrays, whilst also shrinking packaging restrictions, and reducing cost. Integration of the photonic devices with the electronic ICs, could potentially enable this. However, this level of integration is not feasible within the current construction architecture. A possible solution to this lies in the use of silicon photonics, a methodology which takes advantage of the well established manufacturing technologies of the semiconductor industry, and allows full integration of the photonic and electronic components on the same wafer. This offers compelling advantages in terms of cost and scale, as complimentary metal oxide semiconductor (CMOS) technologies are already successfully being utilised to construct passive photonic components, such as low loss waveguides using Si/SiO_2. An issue with this technology arises in the fact that silicon is an indirect band gap material and, as such, constructing an active photonic light source using CMOS technology has yet to be realised. Consequently, researchers are currently pursuing a hybrid III-V/Si structure, where III-V based lasers are situated on a silicon substrate.

As well as the packaging and material science challenges detailed above, in realising the desired opto-electronic integration of PICs, removal of the thermal loads generated is one the most significant demands facing researchers. Thermal management has typically been one of the final steps in microelectronic package design, and was implemented primarily as a means of failure prevention, rather than performance. However, today it is classified as on of the biggest bottlenecks to releasing next-generation photonic systems [5]. In order to achieve the required level of integration, the PIC package must overcome the following thermal challenges:

- The poor thermal properties of silicon-on-insulator (SOI) separating the active components from the heat sink.

- The increase in thermal resistances due to the ridge-like composition of the wave guide, and the junction side up orientation of the laser bars.
- Controlling the temperature of each individual laser to within the tight thermal tolerances of ±0.1K of their defined operational limit.

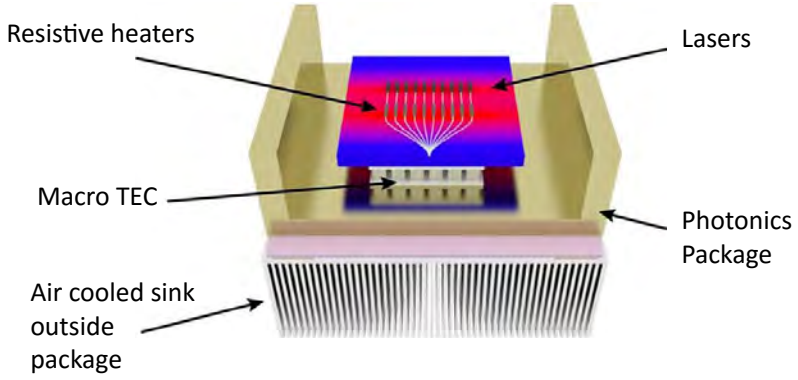

Figure 1.3: Illustration depicting the current state-of-the-art thermal management of PICs. [5]

Surface heat fluxes in the electronics industry have typically been held below $100 W/cm^2$ to facilitate air cooling. However, with the predicted increase in component level heat fluxes, and their large footprint, the heat removal strategies currently implemented in PICs, such as the macroTECs and the air-cooled heat sinks illustrated in Figure 1.3, are preventing device level power density increases – and their economic benefits no longer outweigh the introduction of more advanced cooling techniques. The proposed solution in overcoming this challenge is a Thermally Integrated Photonic System (TIPS), detailed in Figure 1.4. The TIPS project is a consortium of industry and academic research organisations working together to develop and demonstrate a smart and scalable, thermally-enabled, integrated optoelectronic platform, and is funded under the EU Horizons 2020 research and innovation programme (grant agreement No. 644453). It is believed that the application of a TIPS solution will enable the high heat flux removal rates necessary to achieve the decrease in scale and increase in functionality/power density associated with optoelectronic integration,

while also maintaining component level thermal stability. The approach currently being pursued utilises three techniques, detailed as follows:

- Reducing the thermal fluxes experienced at the active photonic components from $\approx 1kW/cm^2$ to $< 0.1kW/cm^2$, through the introduction of materials with improved solid-state thermal performance [5].
- Achieving the required operational thermal tolerances at the individual laser level, by replacing the macroTEC solution and resistive heaters detailed in Figure 1.3, with microTECs encasing each laser.
- Finally, to replace the traditional backside air cooled heat sink removal systems, with a fully integrated source-to-sink microfluidic cooling package. This will also allow for a substantial reduction in package footprint, and enable components to be stacked. Resulting in increased potential for further component level integration, miniaturization and, consequently, greater power densities.

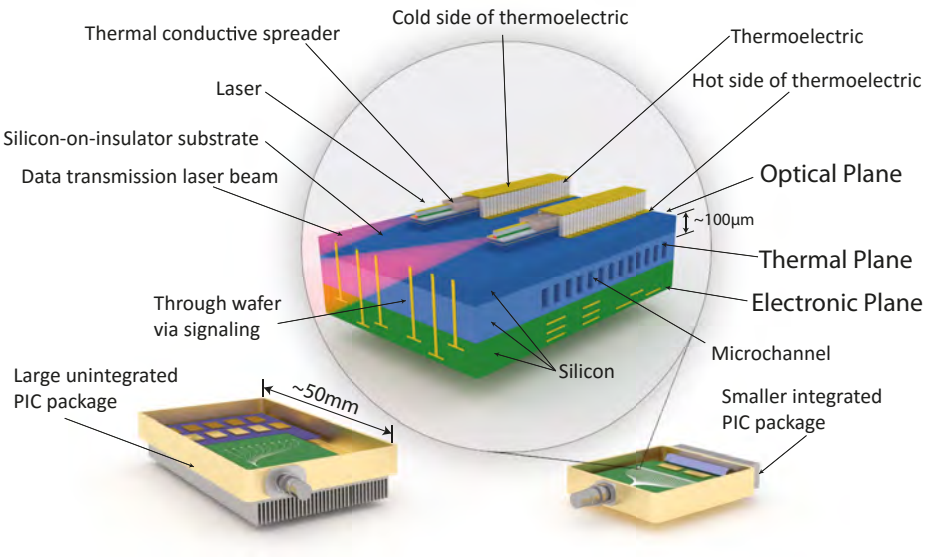

Figure 1.4: Illustration depicting the integration of microTECs and microfluidics in PICs. [4]

Within this context, this thesis will focus on the design and characterisation of a candidate primary or secondary heat exchanger for the proposed microfluidic cooling package.

1.3 Forced Liquid Cooling Solutions

Forced liquid cooling provides more than an order of magnitude higher heat transfer coefficients than air cooling techniques, and has been utilised as a means of high heat flux electronics cooling since the mid 1960s [10]. From 1964 to 1992, hybrid air-to-water cooling solutions were regularly used for the thermal management of high end computers and datacom facilities. However, the switch from bipolar to CMOS circuit technologies in the early 1990s led to a significant reduction in data centre power dissipation – and, with that, a return to the more cost effective air cooling methodologies. With module level heat fluxes for CMOS technologies recently beginning to surpass the level of water cooled bipolar technologies from the early 1990s [10], forced liquid cooling solutions have begun to re-emerge.

There are two primary types of forced liquid cooling solutions: direct and indirect. Direct cooling involves full immersion of the electronic components in a dielectric cooling fluid, and was prominent pre-1980s. Currently, direct cooling is limited to specialised systems, and once off builds. With indirect forced liquid cooling, the system can be single-phase or two-phase, but the coolant does not come into contact with the electronic components, or the substrate upon which they are mounted. Instead, the liquid is in contact with thermal interface materials (TIM) and heat spreading structures, which are used to remove the thermal load from the component surfaces. For the TIPS project, indirect cooling is the preferred solution, and the proposed system comprises a closed loop, single-phase microfluidic circuit, detailed in Figure 1.5. The system will incorporate three key components, which must be realised at the microscale:

1. ***Micropump***: Which circulates the liquid coolant through the system at a specified volumetric flow rate.

2. ***Primary heat exchanger***: Which removes the thermal load from the microelectronics, through the hot side of the thermoelectric material.

3. ***Secondary heat exchanger***: Which rejects the thermal energy in the liquid coolant outside of the package.

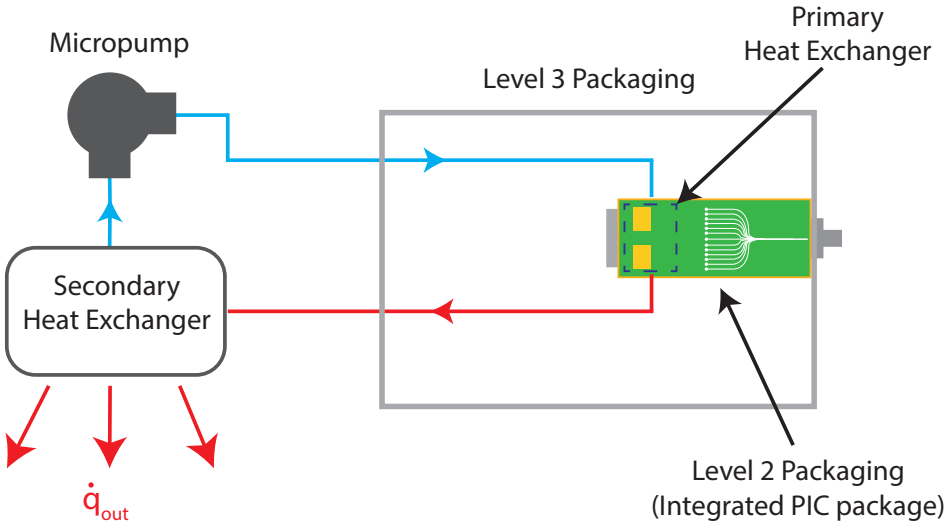

Figure 1.5: Schematic of the proposed closed-loop pumping system for the TIPS architecture.

The design of a suitable micropump is a significant challenge for the TIPS project, and is still an open topic of investigation. Given the critical nature of the PIC package, the required micropump must meet very stringent design considerations, which stipulate that the pump must have a small form factor ($<< 20cm^3$), a relatively long life expectancy, and be free from reliability concerns – whilst generating significant pumping performance ($>$ 5ml/min at 10kPa). An extensive review of micropumping technologies for microfluidic cooling systems was conducted by Singha *et al.* [11]. They categorically reviewed the available technology based on parameters such as: form factor miniaturisation potential, size, power required per unit flow rate, ease and cost of fabrication and, most importantly, suitability for electronics cooling. However, within the current state-of-the-art, no commercially available or research micropumps meet the defined TIPS criteria, and further information on the challenge faced in micropump selection, along

with a proposed novel multi-phase micropump, are detailed in Jeffers *et al.* [4]. The micropump performance specifications are dictated by the mass flow rates and pressure drops required for the chosen primary heat exchanger. As a result of this, the selection and design of a primary heat exchanger has become dependent on available micropump technologies.

Due to their proven high local heat flux removal rates in laminar single-phase microfluidic systems, microchannel and microjet impingement heat sinks have been proposed as hot spot removal techniques. Microchannel heat sinks are classified as low mass flow rate / high pressure drop systems, and their application for the thermal management of electronic components has been studied in great detail [12; 13; 14; 15]. Despite the fact that microchannel heat sinks have lower associated single-phase heat transfer coefficients than impinging jets, they offer compelling advantages in terms of microelectronics cooling, as they can be fabricated directly into the silicon die. This allows the cooling solution to be directly integrated into the electronic components, as detailed in Figure 1.4. Along with the integration possibilities, microchannel heat sinks also allow for a reduction in resistance to heat transfer – due to the decreased thickness in boundary layer profile [13] – and a larger effective surface area compared to impinging jets [16]. Despite this, however, the microelectronics industry has yet to fully embrace microchannel heat sinks. This is believed to be as a result of the increased complexity and cost of their manufacture, and the widespread disagreement amongst the reported literature in regards to their thermal and hydrodynamic behaviour – with studies either exceeding [17] or falling well below [18; 19], the established correlations. Morini [20] conducted a comprehensive investigation into reported thermal and hydrodynamic characteristics of single-phase microchannel heat exchangers. From a review of 29 published papers, experimentally examining the heat transfer coefficients and friction factors of microchannel heat sinks with hydraulic diameters of less than 1mm, it was determined that the Nusselt numbers and friction factors reported were not only in disagreement with the conventional theory for macrochannels for the majority of investigated studies, but they were also inconsistent with one another. Morini [20] concluded that further systematic studies were required to fully understand the transport mechanisms responsible for the observed deviations. Despite the obvious fact that microchannels are

still an open topic of research, from a chronological perspective, the deviations between results were found to be decreasing, as microfabrication tolerances and measurement technique resolutions continue to improve.

An alternative to microchannels, liquid microjets are characterised as high mass flow rate / low pressure drop solutions. They are recognised as a possible thermal management solution for the TIPS project, as they provide the highest recorded heat transfer coefficients for single-phase indirect forced liquid cooling [16] – while also being low cost, due to their ease of manufacture. Compared to microchannels, microjets do however have disadvantages – as it is not easy to integrate them into the substrate, they require much higher mass flow rates, and they have not been adequately characterised in the available literature. Robinson [16] conducted a comparative study on the thermal and hydrodynamic characteristics of liquid microchannels and jet impingement heat sinks, and concluded that both solutions were effective in obtaining the design constraint of dissipating 250 W/cm^2 with less than 0.1W of pumping power. From a practical perspective however, impinging jets were identified as the preferred solution, as they could achieve the necessary cooling requirement, but with increased reliability. This is a result of the lower operating pressures decreasing the risk of leakage, and the less complex manufacture. The higher mass flow rates associated with the jets were also deemed to be a desirable characteristic, as they will promote increased temperature uniformity over the heated surface.

Based on a review of the literature and, more specifically, the conclusions of Robinson [16], a breakdown of the advantages and disadvantages of the two hot spot removal techniques is detailed in Table 1.1. As a result of these attributes the primary focus of this thesis is on the understanding of the thermal and hydrodynamic characteristics of liquid microjets – and to identify their feasibility as a heat exchanger in a single-phase microfluidic cooling solution for PIC packages. Typically, impinging jets are of a circular or axisymmetric geometry, however, for this thesis it was decided to investigate the behaviour of slot jets. The primary reasons for this was that, when compared to axisymmetric jets, slot jets offer increased geometric compatibility with the PIC package (as opposed to using an array of axisymmetric jets), enhanced entrainment and mixing properties [21], and increases in surface heat transfer within the stagnation zone [22].

Table 1.1: Comparison of microchannel and microjet heat sinks.

Technique	Advantages	Disadvantages
Microchannel heat sink	Lower mass flow rates, integration, large body of literature	High pressure drop, cost and complexity, disagreement amongst literature
Microjet heat sink	Low pressure drop, ease of manufacture, scalable, geometric compatibility	High mass flow, limited research, thermal integration

1.4 Research Objectives

This thesis investigates the control and enhancement of confined, submerged, impinging slot jets, to asses their feasibility in the design of a single-phase microfluidic cooling solution. The influence of slot jet nozzle aspect ratio, and the application of passive outlet structures, were characterised both thermally and hydrodynamically, for a range of different Reynolds numbers. The main objectives are as follows:

- To capture the local velocity flow fields associated with each geometry, in order to understand the fluidic mechanisms influencing the surface heat transfer distributions.
- To measure both local and area-averaged heat transfer coefficients along the impingement surface, for each investigated geometry and flow rate.
- To conduct a pressure drop analysis on all investigated geometries and flow rates, in order to understand the hydrodynamic penalty associated with any potential enhancements in heat transfer achieved.

1.5 Thesis Compendium

The remaining chapters of this thesis are detailed as follows:

- *Chapter Two* reviews the background literature on the thermal and hydrodynamic characteristics of impinging jets, by discussing the previously conducted work and identifying regions where there are open questions as to their behaviour.
- *Chapter Three* describes the experimental methods utilised throughout the investigation.
- *Chapter Four* details and discusses the influence of jet nozzle aspect ratio on the thermal and hydrodynamic behaviour of a confined liquid slot jet in the laminar flow regime.
- *Chapter Five* details and discusses the passive control and enhancement of low Reynolds number slot jets, through the use of jet nozzle outlet modifications in the form of tabs and chevrons.
- *Chapter Six* draws conclusions and evaluates the investigated work. Lastly, it includes recommendations for possible future work.

Chapter 2

Impinging Jets

Impinging jets have found application as a thermal design solution for many engineering applications requiring high rates of convective heat transfer. The most common examples of these are turbine blade cooling [23], metal annealing [24], glass tempering [25] and, more specific to this thesis, the cooling of microelectronic components. As a result of their geometric flexibility, and scalability, the form of impinging jets is highly varied. Moreover, due to the effects of entrainment, stagnation zones, and streamline curvature, the thermal and hydrodynamic behaviour can be quite complex for even the most rudimentary impinging jet design. As a result of this, the application of impinging jet heat sinks requires detailed characterisation. This section details the relevant research previously conducted into impinging jets. The objectives are to identify areas where a fundamental understanding of impinging jet characteristics remains an open research question and, consequently, where any possible enhancements in convective heat transfer could be achieved.

This chapter is divided into four sections. The first section details the hydrodynamic behaviour of confined, submerged impinging jets, and the fluidic mechanisms which will define the surface temperature distributions. The second section follows on from this by introducing the characteristic regions of heat transfer associated with impinging jets. The third section introduces slot jets, along with their advantages and disadvantages for microelectronics cooling, and the fourth section concludes with the subject of passive structures, and their current application in impinging jets.

2.1 Hydrodynamic Characteristics

Impinging jets can be applied as a single jet or as an array, and there is extensive literature available on both. Given that single jets are the subject of this study, this section will focus on the hydrodynamic behaviour of such a jet. More information on multiple jet arrays can be found in Geers *et al.* [26] and Zuckerman and Lior [27]. For a single normally impinging jet, there currently exists comprehensive reviews – through both experimental and numerical methodologies – which determine and detail the fundamental fluid flow characteristics of both free and confined jets [28; 29; 30; 31; 32; 33]. Traditionally, jet nozzle designs are either round jets with an axisymmetric flow profile, or slot jets, which have a thin two-dimensional flow profile [27]. However, all impinging jet designs feature the same fundamental hydrodynamic zones, which are: the free jet zone, the stagnation zone, and the wall jet zone. Figure 2.1 details the location of these three zones, for a submerged impinging jet.

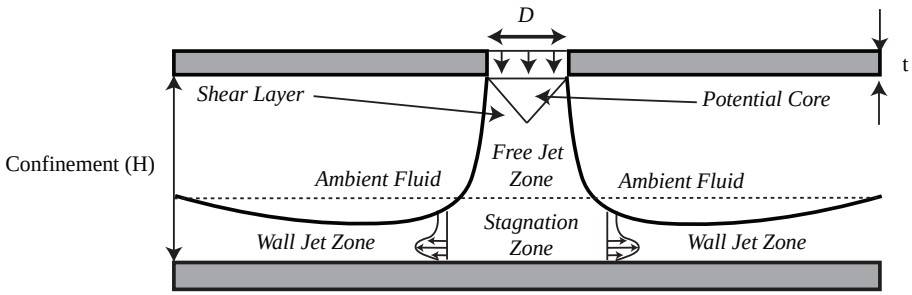

Figure 2.1: Characteristic zones associated with the hydrodynamic behaviour of confined submerged impinging jets.

For the majority of the literature on jet hydrodynamic behaviour, the flow fields are typically defined in terms of the jet exit Reynolds number (Re):

$$Re_L = \frac{\rho U_{mean} L}{\mu} \tag{2.1}$$

Where U_{mean} is the mean jet exit velocity, and L is some length scale which is typically based on the jet nozzle diameter (D) for axisymmetric jets or the hydraulic diamater (D_h) for non-axisymmetric jets.

2.1.1 Free Jet Zone

The flow in the free jet zone is axial in direction, and sufficiently far from the impingement surface that it is not influenced by its presence [34]. This results in a velocity profile similar to that of a free submerged jet. The free jet can be divided into two regions: the potential core and the lower velocity mixing layer [28]. Within the potential core of the jet, the velocity and turbulence intensity is equal to that of the exit velocity, and remains constant throughout. As the jet progresses downstream from the exit, the shear-driven interaction between the jet and the surrounding ambient fluid results in the formation of a shear layer. As the shear layer grows, it entrains ambient fluid and causes the jet to spread radially outwards, resulting in the gradual decrease in the width of the potential core. Eventually the shear layer reaches a point where it penetrates the jet centreline, and the axial velocity of the jet begins to decrease, while the turbulence intensity increases.

The length of the potential core depends on several factors such as: the Reynolds number [35], nozzle geometry (axisymmetric [36; 37], or slot jets [38; 39]), and the jet exit velocity profile [28; 40]. For slot jets, Martin [31] and Zhou and Lee [41] both found the potential core length to be up to four slot widths from the jet axis. Sfeir [42] and Quinn [38], found that the length of the potential core for slot jets is dependent on the jet nozzle aspect ratio (L/W). Quinn determined that increasing jet nozzle aspect ratios from 2 to 20 resulted in the length of the potential core decreasing from 2.86 to 1.03 times the hydraulic diameter. Predominantly, work has been conducted on submerged jets in the turbulent flow regime, however, Akaike and Nemoto [43] performed an experimental and numerical analysis of the free jet zone of a laminar submerged axisymmetric water jet. They found that the axial distance downstream from the nozzle exit where the potential core is fully diminished (x), can be estimated using the jet diameter (D), and Reynolds number (Re), such that: $0.04 = x/DRe$. Hrycak *et al.* [44]

experimentally investigated an axisymmetric air jet impinging on a flat surface. They found that the potential core length is dependent on the jet exit Reynolds number, and that increasing the Reynolds number from 300 to 500 results in the potential core length increasing from 14 to 21 nozzle diameters. Miyazaki and Silberman [45] theoretically analysed a two-dimensional confined, laminar, liquid jet discharging into ambient gas. They also concluded that potential core length was dependent on Reynolds number, and was found to increase from 6.6 nozzle widths at Re = 100, to 34 at Re = 500. Based on these reported results, it is postulated that for slot jet nozzles of aspect ratios between 1 and 8, over a Reynolds number range of 100 to 500, and a confinement to jet nozzle hydraulic diameter ratio of 1 – such as the geometries investigated in this thesis – the length of the potential core will be greater than the confinement height. This will therefore result in potential core impingement, and the identifying features of such behaviour will be investigated in this thesis.

2.1.2 Stagnation Zone

The target surface is found to have an influence upon the impinging jet at an upstream distance of 1.2 nozzle diameters [31; 46], and this initiates the beginning of the stagnation zone. Within this zone, the jet velocity decelerates axially, and is deflected radially outwards – characterised by the presence of strong velocity streamline curvature. Popiel and Trass [47] showed that the impingement of the jet on the target surface creates a region of positive pressure gradient within the stagnation zone. This positive pressure gradient results in the formation of a velocity boundary layer of near constant thickness (δ_{Hydro}) [46]; thus, affecting the local heat transfer distributions within the stagnation zone, which will be discussed further in Section 2.2.1. For the confinement ratio (H/D_h) of 1 used in this thesis the presence of potential core impingement is expected. Consequently, the formation of a thin boundary layer profile of near constant thickness is likely within the stagnation.

2.1.3 Wall Jet Zone

Due to the axial deceleration and radial deflection of the impinging jet in the stagnation zone, the flow moves radially outwards to form a wall jet along the target surface, illustrated in Figure 2.2. As previously mentioned, the hydrodynamic boundary layer begins in the stagnation zone and, as it moves radially outwards, the reduction in pressure gradient allows the boundary layer to develop and thicken [47]. As it progresses along the impingement surface, the increasing flow area and viscous effects result in a reduction in average velocity within the boundary layer, and the point of peak velocity moves closer to the liquid shear layer. This continues until the boundary layer has developed to the shear layer surface. Beyond this point, the wall jet flow begins to transition to a turbulent regime, forming the fully turbulent zone. Eventually, the wall jet reaches a point where – due to wall friction on one side and the shear-driven interaction between the wall jet and the ambient fluid on the other – the boundary layer velocity relative to the surface approaches zero. The wall jet then detaches from the impingement surface, and the flow is subject to local reversals and recirculation, resulting in the formation of vortical structures. Poreh *et al.* [48], investigated the velocities, turbulence intensities, and wall shear stresses, in the wall jet formed by an axisymmetric impinging jet. They determined the height of the wall jet and

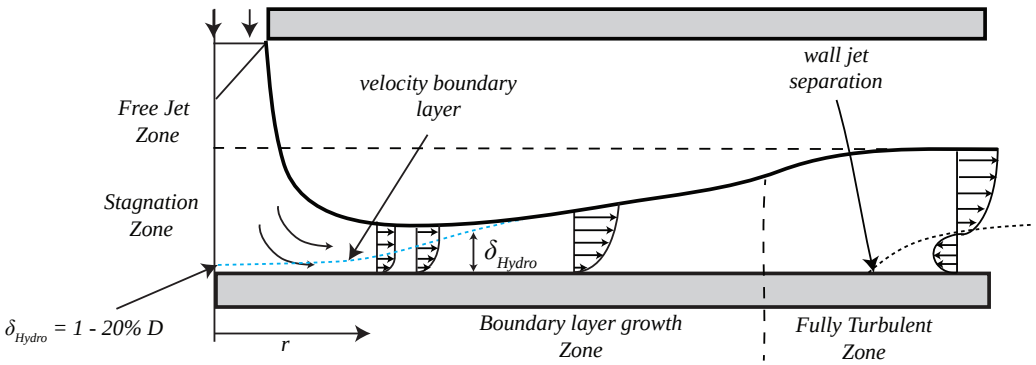

Figure 2.2: Detailed illustration of the wall jet zone for a confined submerged impinging jet.

maximum velocity achieved to be dependent on the jet exit velocity and radial distance from the stagnation point.

2.1.4 Influence of Jet Design

The hydrodynamic behaviour of impinging jets have been found to be dependent on various jet design variables. These variables have been utilised by researchers as a means of enhancing favourable hydrodynamic behaviour, and include: the application of a confinement plate, modifying nozzle geometry, changing the angle of impingement, and introducing turbulence generators.

- ***Confinement***: Confined impinging jets feature a plate surrounding the jet nozzle, which serves to confine the flow between the plate and the impingement surface and is illustrated in Figure 2.2. Fitzgerald and Rice [49] experimentally investigated the flow field of an axisymmetric, confined, submerged, turbulent jet, normally impinging on a flat plate. For confinement ratios (H/D) ratios of 2, 3, and 4, they found that when compared to a free jet, the confined case resulted in an increased potential core length, and a decrease in turbulence intensity. However, the confinement plate also resulted in a flow recirculation zone, which moves radially outwards from the stagnation zone with increasing Reynolds number. In agreement with Fitzgerald and Rice [49], Behnia *et al.* [50] also discovered a region of recirculation outside of the stagnation zone, resulting from the application of a confinement plate. They concluded that despite its proximity, it had a negligible impact upon the hydrodynamic behaviour of the wall jet. Ashforth-Frost *et al.* [39] found that for a turbulent slot jet at a Reynolds number of 20,000, the application of a confinement plate resulted in decreased entrainment and spreading and, therefore, an increase in potential core length when compared to a free jet. With regard to the limit of the influence of jet confinement, Gao and Ewing [51] found that for a fully developed turbulent, confined, axisymmetric jet, the presence of a confinement plate had no effect on the hydrodynamic behaviour of the jet for H/D $\geq$6.

- ***Nozzle geometry***: The initial jet exit velocity profiles and turbulence intensities are very much dependent on the jet nozzle geometry. Currently, there exists a large body of work on the influence of jet nozzle geometry on the exit velocity profiles of impinging jets. The three primary design modifications have been identified as: the ratio of the jet tube length to jet diameter (L/D) [52; 53; 54], the nozzle shape [55; 56], and the use of passive (see Section 2.4) or active outlet structures [57; 58]. Geers [54] states that for sharp-edged orifice plates with a low plate thickness to diameter ratio (t/D), the upstream contraction effects, or *vena contracta*, influence the velocity profile within the jet nozzle, such that the velocity at the edges is higher than that of the jet centerline. This hypothesis has been confirmed in the work of Lee and Lee [55] and Ashforth-Frost and Jumbanathan [37] – with Lee and Lee [55] further expanding on this by confirming the relationship between off-center peaks in the jet exit velocity profile, and associated peaks in heat transfer coefficient along the impingement surface. In line with this, Garimella and Nenaydyk [53] experimentally investigated the influence of the ratio of orifice plate thickness to jet diameter (t/D_h) for a range of geometries between $0.25 < t/D < 12$. They found that for $t/D_h < 1$, the contraction of the upstream flow results in a separation bubble forming at the inlet of the nozzle. This effect has a significant impact on the shape and magnitude of the jet exit velocity profile and, in turn, the local heat transfer coefficients along the impingement surface. By increasing t/D_h from 1 to 4, the separated flow begins to reattach within the nozzle, and the jet exit velocity profile progresses towards a more uniform profile.

  Lee and Lee [55] investigated the effect of nozzle inlet chamfering on the exit of an impinging axisymmetric air jet. They found that, when compared to the conventional square-edged jet, the variation of nozzle inlet chamfering alters the initial flow structure of the jet, and can be utilised as a passive control technique. They also concluded that increasing the chamfering angle results in higher velocity gradients and turbulence intensities at the jet exit. The application of tabs at the jet outlet have been found to control and enhance the flow field behaviour of jets, as they result in the formation of streamwise vortical structures, whilst also decreasing the

length of the potential core and influencing jet shear layer formation and spreading. When comparing axisymmetric or slot jet nozzle geometries, Ho and Gutmark [59] determined that slot jets, either elliptical or rectangular in shape, achieve entrainment rates significantly larger than those of axisymmetric jets, due to vortex self-induction effects – and concluded that slot jets were more favourable for applications which require enhanced mixing between the jet flow and the surroundings. The application of tab and chevron structures will be discussed further in Section 2.4.

- ***Angle of impingement***: The hydrodynamic behaviour of inclined or oblique impinging jets has been studied by many authors [60; 61; 62; 63]. Foss *et al.* [60] found that, for low angles of impingement (9°), the geometric location of the stagnation point is displaced from the centre of the jet, and spreads laterally beyond the location of maximum static pressure. However, for higher angles (45°) [61], this was no longer determined to be the case, with both points found to be coincident.
- ***Turbulence generators***: Zhou and Lee [64] experimentally examined the impact of mesh screens with varying solidity, upstream of the jet nozzle. For low nozzle-to-plate spacings ($H/D \leq 4$), they found that within the stagnation zone, the screens increased jet turbulence intensity while simultaneously decreasing static pressure. Nakod *et al.* [65] studied the effect of an axisymmetric air jet impinging upon a target surface containing fin structures, and vortex generators. They found that vortex generators located on a plate, at a fixed confinement height such that potential core impingement will occur, resulted in increased surface heat transfer compared to a plate absent of any structures. They attributed this to the vortex generators disrupting the jet prior to impingement, and increasing the turbulence intensity within the potential core. However, they did not conduct any flow field analysis to confirm this hypothesis.

For this thesis, the slot jets investigated will be fully confined and normally impinging sharp-edged orifice plates, with thickness to hydraulic diameter (t/D_h) and confinement (H/D_h) ratios of 1.

2.2 Thermal Characteristics

The thermal characteristics of impinging jets have been studied extensively [28; 66; 67; 68], and are typically presented in terms of the non-dimensional Nusselt number (Nu):

$$Nu = \frac{hL}{k} \tag{2.2}$$

where h is the heat transfer coefficient along the impingement surface, L is some characteristic length scale – typically given as the hydraulic diameter D_h for non-axisymmetric jets – and k is the thermal conductivity of the working fluid. The heat transfer coefficient (h) is defined by eq. (2.3), where q'' is the convective heat flux and T_W and T_{in} are the temperatures of the impingement surface and the jet inlet, respectively.

$$h = \frac{q''}{T_W - T_{in}} \tag{2.3}$$

When discussing the thermal characteristics of impinging jets, studies are typically divided into the stagnation, and wall jet zones. The Nusselt number distributions within these zones are dependent on the hydrodynamic characteristics of the approaching jet, and correlations provided in the literature are typically presented in the form of Nusselt number as a function of both Reynolds number and the fluid Prandtl number. The fluid Prandtl number is defined below:

$$Pr = \frac{C_p \mu}{k} \tag{2.4}$$

where C_p is the specific heat, μ is the dynamic viscosity, and k is the fluid thermal conductivity. As water was used in this thesis, the Prandtl number exponent of 0.4 is based on that most widely used in the literature for water jets [28; 66], and as a result the provided Nusslet - Reynolds number correlations were provided in the given form:

$$\frac{Nu}{Pr^{0.4}} = f(Re) \tag{2.5}$$

2.2.1 Stagnation Zone

The local maximum in stagnation zone heat transfer is typically found at the stagnation point, where r/D = 0. However, for a fixed Reynolds number, if the confinement ratio (H/D) separating the nozzle from the impingement surface is low enough, such that the potential core will strike the impingement surface, then the Nusselt number will remain mostly invariant within the stagnation zone [66; 68]. This is due to the constant axial velocity and turbulence intensity within the potential core. Increasing H/D to a distance beyond the potential

Table 2.1: Stagnation point Nusselt number correlations for axisymmetric jets (sorted by working fluid).

Author	Correlation ($Nu_0 =$)	Parameters
Li & Garimella [69]	$1.039Re^{0.515}Pr^{0.444}(l/D)^{-0.058}(D_{Heater}/D^{-0.246})$	$8{,}500 \leq Re \leq 23{,}000$ Water l/D = 2 $1 \leq H/D \leq 4$ Confined
Sun *et al.* [66]	$0.9553Re^{0.5}Pr^{0.4}$	$5{,}000 \leq Re \leq 36{,}000$ Water $2 \leq H/D \leq 10$ Free
Garimella & Rice [28]	$0.492Re^{0.585}Pr^{0.4}(l/D)^{-0.09}(H/D)^{0.024}$	4,000<Re<23,000 FC-77 l/D = 0.25 – 12 H/D = 1 – 5 Confined
	$0.513Re^{0.694}Pr^{0.4}(l/D)^{-0.04}(H/D)^{-0.56}$	4,000<Re<23,000 FC-77 l/D = 0.25 – 1 H/D = 6 – 14
Lytle & Webb [70]	$0.663Re^{0.53}(H/D)^{-0.248}$	$3{,}700 \leq Re \leq 30{,}000$ Air $0.1 \leq H/D \leq 0.5$ Free
Lee & Lee [55]	$0.641Re^{0.566}(H/D)^{-0.078}$	$10{,}000 \leq Re \leq 30{,}000$ Air $2 \leq H/D \leq 10$ Free
Li & Garimella [69]	$1.427Re^{0.496}Pr^{0.444}(l/D)^{-0.058}(D_{Heater}/D^{-0.272})$	$8{,}500 \leq Re \leq 23{,}000$ 0.7<Pr<25.2 l/D = 2 $1 \leq H/D \leq 4$ Confined

core will lead to a monotonic decrease in stagnation zone heat transfer, as the axial velocity of the jet is diminished. It has been reported that there exists a point just beyond the potential core length where the stagnation point Nusselt number can reach a maximum value [28; 46]. This maximum is attributed to the penetration of turbulence induced mixing from the shear layer to the centreline of the jet, which compensates for the slight reduction in peak axial velocity. From a review of the available literature, correlations for stagnation point Nusselt number for axisymmetric and slot jets are presented in Tables 2.1 and 2.2. For jets that have a H/D lower than the length of the potential core – such as in this thesis – the positive pressure gradient imposed on the surface is found to laminarise the flow within this initial region of the stagnation zone even for turbulent exit Reynolds numbers, resulting in a relatively thin thermal boundary layer of near constant thickness within the stagnation zone [31]. Therefore, the correlations found in the literature for stagnation point Nusselt numbers featuring potential core impingement are predominantly found to be proportional to $Re_{Dh}^{\sim 0.5-0.59}$, which is consistent with the presence of a laminar boundary layer [71]. For H/D ratios greater than the length of the potential core, the presence of the turbulence induced mixing results in the stagnation point Nusselt numbers scaling with $Re_{Dh}^{0.6-0.7}$ for transitional jets, and $Re_{Dh}^{\geq 0.7}$ for fully turbulent jets.

Table 2.2: Stagnation point Nusselt number correlations for slot jets (sorted by working fluid).

Author	Correlation ($Nu_0 =$)	Parameters
Vader *et al.* [72]	$0.28Re^{0.58}Pr^{0.4}$	$20{,}000 \leq Re \leq 90{,}000$ Water Aspect Ratio = 10.3 $9.1 \leq H/D \leq 12.9$ Free
Chen *et al.* [73]	$0.313Re^{0.573}Pr^{0.333}$	$600 \leq Re \leq 1{,}200$ Kerosene Aspect Ratio = 280 H/D = 2,4 Semi-Confined
Choo *et al.* [74]	$0.1Re^{0.74}(H/D_h)^{-0.15}$	$150 \leq Re \leq 2{,}500$ Air Aspect Ratio = 40 $1 \leq H/D \leq 10$ Free

2.2.2 Wall Jet Zone

In the presence of a heat flux applied to the impingement surface, a thermal boundary layer will form in conjunction with the hydrodynamic boundary layer. As the wall jet described in Section 2.1.3 progresses radially outwards from the stagnation zone, the thermal boundary layer will begin to develop and thicken, which is associated with a monotonic decrease in surface convective heat transfer coefficient [78]. When investigating the heat transfer over the stagnation and wall jet zones, researchers typically refer to the area-averaged Nusselt number. For both axisymmetric and slot jets, Tables 2.3 and 2.4 present correlations for area-averaged Nusselt number available in the literature. However, it is important to note that not all studies referenced defined the area over which they averaged,

Table 2.3: Area-averaged Nusselt number correlations for axisymmetric jets (sorted by working fluid).

Author	Correlation (Nu_{Avg} =)	Parameters
Li & Garimella [69]	$0.69Re^{0.555}Pr^{0.452}(l/D)^{-0.07}(D_{Heater}/D)^{-0.348}$	$8{,}500 \leq Re \leq 23{,}000$ Water l/D = 2 $1 \leq H/D \leq 4$ Confined
Garimella & Rice [28]	$0.16Re^{0.695}Pr^{0.4}(l/D)^{-0.11}(H/D)^{0.11}$	4,000<Re<23,000 FC-77 l/D = 0.25 – 12 H/D = 1 – 5 Confined
	$0.164Re^{0.773}Pr^{0.4}(l/D)^{-0.05}(H/D)^{-0.52}$	4,000<Re<23,000 FC-77 l/D = 0.25 – 1 H/D = 6 – 14
Goldstein *et al.* [75]	$Re^{0.76}(24 - \lvert H/D - 7.75\rvert)/(533 + 44(r/D)^{1.394})$	$61{,}000 \leq Re \leq 124{,}000$ Air $6 \leq H/D \leq 12$ Free
Martin [31]	$0.54Re^{0.667}(d/r)(1 - 1.11d/r)/(1 + 0.1(H/D - 6)D/r)$	$30{,}000 \leq Re \leq 120{,}000$ Air $6 \leq H/D \leq 12$ Free
Li & Garimella [69]	$0.978Re^{0.5259}Pr^{0.452}(l/D)^{-0.07}(D_{Heater}/D)^{-0.381}$	$8{,}500 \leq Re \leq 23{,}000$ 0.7<Pr<25.2 l/D =2 $1 \leq H/D \leq 4$ Confined

Table 2.4: Area averaged Nusselt number correlations for slot jets (sorted by working fluid).

Author	Correlation (Nu_{Avg} =)	Parameters
Zhou & Lee [41]	$0.162Re^{0.616}Pr^{0.4}$	2,715 $\leq Re \leq$ 24,723 Air Aspect Ratio = 4 $1 \leq H/D \leq 4$ Free
Lin *et al.* [76]	$4.229Re^{0.5}Pr^{0.333}$	190 $\leq Re \leq$ 1,537 Air Aspect Ratio = 1 $1 \leq H/D \leq 8$ Confined
Choo *et al.* [74]	$0.0784Re^{0.74}(H/D_h)^{-0.15}$	150 $\leq Re \leq$ 2,500 Air Aspect Ratio = 40 $1 \leq H/D \leq 10$ Free
Al-Sanea [77]	$0.08Re^{0.65}$	50 $\leq Re \leq$ 500 Air 1H/D = 4 Semi-Confined
Al-Sanea [77]	$2.84(H/D)^{-0.18}$	Re = 200 Air $1 \leq H/D \leq 2.5$ Semi-Confined
Al-Sanea [77]	$2.3(H/D)^{0.04}$	Re = 200 Air $2.5 \leq H/D \leq 5$ Semi-Confined
Al-Sanea [77]	$2.45Pr^{0.4}$	Re = 200 0.1 $\leq$ Pr $\leq$ 100 H/D = 4 Semi-Confined

and those who did mostly based this value on the heater size and did not maintain consistency with preceding studies. Nu_{Avg} is also dependent on other parameters such as the spatial resolution of the investigations i.e. whether any possible local peaks were captured. Given the eventual transition of the wall jet to turbulent flow, the correlations include both laminar and turbulent regions of the wall jet. Due to this, the Reynolds number exponent for the area-averaged Nusselt number correlations can vary from 0.5 to 0.76, depending on the experimental parameters. The fluid Prandtl number (Pr) is a dimensionless parameter which relates the thickness of both the thermal and hydrodynamic boundary layers. For

Pr > 1, such as the water jets used in this thesis, the thermal boundary layer will transition from surface to freestream temperature, at a larger radial distance than the point where the height of the hydrodynamic boundary layer reaches the shear layer. Therefore, the working fluid utilised in a jet system dictates the rate of thermal boundary layer growth, and hence, will influence the Nusselt number distributions along the wall jet zone.

2.2.3 Working Fluid

As mentioned above, the working fluid utilised in a jet system dictates the growth of the thermal boundary layer. The choice of working fluid utilised in a jet system is influenced by a range of factors, such as the jet scale and thermophysical properties of the fluid. Conventionally, jet impingement systems have been associated with air jets; however, with the emergence of high heat flux electronics at the microscale, air is no longer a viable working fluid for such applications. This is due to the associated relatively low convective heat transfer rates ($\sim 10 - 10^2 W/m^2K$), and acoustical concerns resulting from reported jet unsteadiness in the low Reynolds number regime [79; 80]. As a result of this, researchers have turned their focus towards liquid jets due to their superior thermal conductivity, specific heat, and Prandtl number. The effects of fluid Prandtl number on impinging jets has been studied for an extensive range of working fluids in previous studies [73; 81; 82; 83]; with predictive correlations for local and area-averaged Nusselt numbers presented for Prandtl numbers in the range of 0.7 to 262. Advances in nanotechnology and material science have also seen the application of nanoparticle seeded working fluids, with copper-water [84] and Al_2O_3-water [85] nanofluids. Manca *et al.* [86] conducted a numerical study into the thermal and hydrodynamic behaviour of confined slot jet flow with an Al_2O_3-water nanofluid. They found that the magnitude of the vortical structures formed, and the local Nusselt number distributions, were not just dependent on Reynolds number and confinement height, but also on the nanofluid concentration. Although some enhancement in heat transfer coefficient has been associated with these nanofluids, it is still a relatively new research topic. Due to this, more extensive reviews are required prior to their application in critical microelectronic

systems, and the focus of researchers remains on proven working fluids, such as water.

2.3 Impinging Jet for TIPS

For an impinging jet heat sink to be considered a suitable heat removal strategy for a thermally integrated photonics system, certain design criteria must be satisfied. The heat sink must be:

- Low profile ($\approx 400 - 500\mu m$ [4; 5]), due to the tight packaging restrictions, and to enable component stacking.
- In the laminar flow regime ($Re_{Dh} < 600$), defined by previous slot jet investigations [73; 76; 87] – to limit high velocity concerns at the microscale, such as increased system pressure drop [16; 79; 80].
- Operational with a proven working fluid for such high heat flux applications.
- Geometrically compatible with the PIC package.

Due to their enhanced mixing and entrainment rates [21], geometric compatibility with the PIC package, and increased area-averaged Nusselt number when compared to axisymmetric jets [22], impinging slot jets were identified as a candidate heat exchanger for the TIPS project. The thermal and hydrodynamic behaviour of confined submerged slot jets is determined by the: jet confinement height (H/D) [73; 74; 76; 88], flow rate, working fluid [73; 85; 89] and jet nozzle geometry [56; 90; 91]. As a result of the design criteria outlined above, the operational range of flow rates and confinement heights – as well as suitable working fluids – will be limited. Therefore, it is clear that any possible techniques for control and enhancement of the slot jet thermal and hydrodynamic behaviour must be extracted through modifications to the jet geometries. This section discusses the work currently completed into the design of low Reynolds number slot jets.

There is a large body of work completed on the effect of confinement ratio on the heat transfer behaviour of impinging slot jets [28; 30; 31; 92]. For microelectronics cooling, low profile design is a significant constraint due to stringent

packaging restrictions. Therefore, impinging jet packages for such applications utilise a fully confined configuration, with a confinement height as low as possible. Sivasamy *et al.* [6] conducted a numerical investigation into the flow behaviour of 2D low Reynolds number slots, confined by a parallel wall. They examined the influence of different confinement ratios ($2 < H/D_h < 5$) on the flow behaviour of a single, confined, laminar slot jet for a Reynolds number range of 100 to 500. They found that for all confinement heights, the shear-driven interaction between the exiting jet and the surrounding ambient fluid resulted in the entrainment of ambient fluid in towards the jet discharge, and the formation of a vortical structure. They called this the primary vortex, and it was found to elongate and move downstream with increasing Reynolds number. It was also observed that, at higher Reynolds numbers, a secondary vortical structure was present at the point at which the wall jet detached from the impingement surface. As with the primary vortex, this secondary structure also moved downstream with increasing Reynolds number. The flow was then found to reattach to the impingement plate further downstream. Beyond the point of reattachment the velocity streamlines

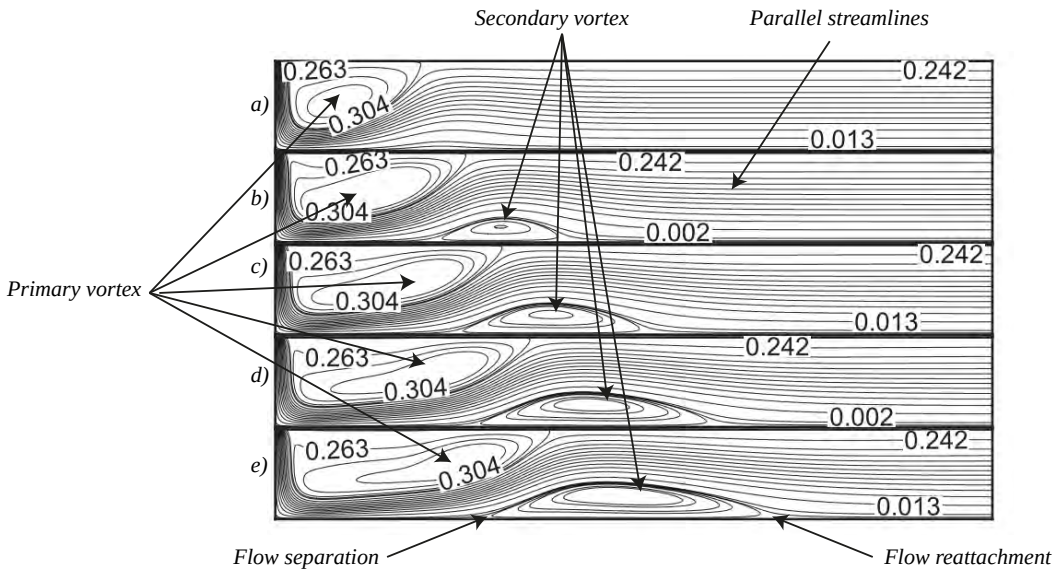

Figure 2.3: Velocity streamlines recorded by Sivasamy *et al.* [6] for a two-dimensional laminar slot with H/D = 5, over a range of Reynolds numbers: a) Re = 100, b) Re = 200, c) Re = 300, d) Re = 400, and e) Re = 500.

become parallel, and indicative of fully developed flow, similar to that in channel flow. The presence of all these fluidic mechanisms observed by Sivasamy *et al.* [6] are detailed in Figure 2.3.

Sahoo and Sharif [93], and Lee *et al.* [7], also conducted numerical investigations into the 2D velocity and temperature fields of confined low Reynolds number slot jets, with a Reynolds number range of between $50 < Re_{Dh} < 500$. As with Savisamy *et al.* [6], both studies also recorded the formation of a primary vortex due to the entrainment of ambient fluid at the jet exit, and a secondary vortex due to wall jet detachment. The magnitude and location of these vortices, and the point of wall jet reattachment, were found to be dependent on both Reynolds number and confinement height. It is interesting to note that, when examining the distribution of Nusselt numbers along the impingement surface, both Sahoo *et al.* [93] and Lee *et al.* [7], observed the presence of inflection points in the local Nusselt number profiles, as can be seen in Figure 2.4. Lee *et al.* [7] concluded these inflection points to be a result of the jet detachment from the impingement surface, and reattachment further downstream, which was associated with the presence of the secondary vortices. Although these studies examined the impact of confinement height on the thermal and hydrodynamic behaviour of confined low Reynolds number slot jets, all three utilised air as the working fluid, and were confined to two dimensional numerical investigations of a high aspect ratio nozzle geometry. It is evident that thermal and hydrodynamic behaviour of confined

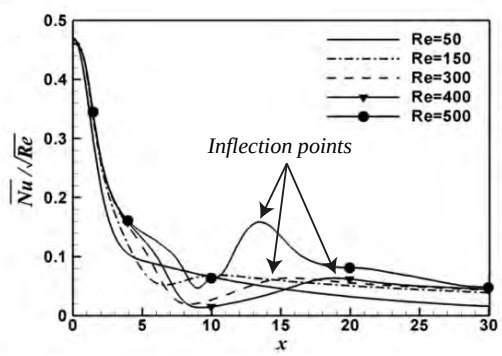

Figure 2.4: Distribution of time-averaged Nusselt number normalised by $Re^{0.5}$ along the impingement surface, recorded by Lee *et al.* [7].

liquid slot jets is still an open topic of investigation.

For impinging jet systems, heat transfer enhancements are typically achieved through the generation of higher jet velocity gradients, and the turbulent structures associated with increasing jet exit Reynolds number beyond the critical laminar-turbulent transition number ($600 \leq Re_{Dh} \leq 1225$ [73; 76; 87]). As specified in the TIPS design constraints, limitations are imposed on the flow rates of micro-scale jet systems in order to reduce high velocity concerns such as noise levels with air jets [79; 80], and impractical system pressure drops. Due to this, the systems are confined Reynolds numbers below 600 and, therefore, feature predominantly laminar flow regimes. With Reynolds numbers then becoming a fixed design constraint, researchers have begun to examine the influence of nozzle geometry on the local heat transfer distributions, and any possible enhancements that could be achieved through geometric modification. From a review of the literature, it was found that very few studies have addressed the influence of jet nozzle geometry on the thermal behaviour of low Reynolds number slot jets.

Sezai and Mohamad [8] numerically investigated the temperature and velocity fields of confined impinging slot jets in the laminar flow regime ($100 <$ Re < 500), for jet nozzle aspect ratios of 1 to 8. They noted the existence of pronounced off-center peaks in the streamwise velocity flow fields and local Nusselt number distributions along the long axis of rectangular jets, which resulted in the formation of what they termed as a "saddle-back" profile, as seen in Figure 2.5. This phenomena has been widely reported in turbulent slot jets, but it has been attributed to turbulent flow field effects, such as vortex ring shedding [56] and pressure induced secondary flows [94]. Sezai and Mohamad conducted a detailed examination of the pressure and velocity fields along the jet development plane, but they were unable to come to any definitive conclusions as to the exact cause of these off-center peaks in the laminar regime. Based on their investigated flow rates ($Re_{Dh} < 500$), and the application of a uniform velocity profile boundary condition at the nozzle exit, they concluded that the peaks were neither a result of turbulent flow structures, nor upstream conditions. However, by examining the pressure gradients at the jet exit, they discovered that a negative pressure gradient was induced around the nozzle exit cross-section, which entrained fluid from both the ambient surroundings and the jet core, towards two points located

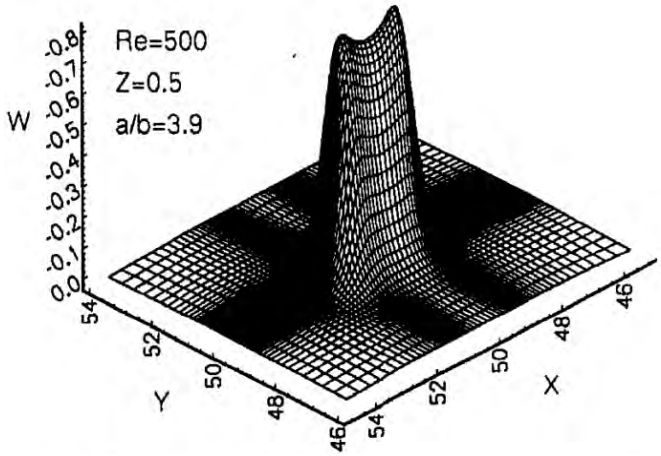

Figure 2.5: Jet velocity profile near the impinging plate, illustrating the saddle-back phenomenon for an aspect ratio of 4 slot jet with a Reynolds number of 500 and a confinement ratio of 0.5 [8].

at the ends of the major axis of the jet. They established that these points corresponded to the observed off-centre peaks, but did not definitively conclude them to be the cause. Chen and Yu [95] and Yu and Girimaji [96] conducted numerical investigations into effect of slot jet aspect ratio on low Reynolds number (<300) free slot jets, using 3D Lattice-Boltzmann modeling techniques. Both studies confirmed the formation of a saddle-back flow profile, in line with Sezai and Mohamad [8]. However, they determined the driving fluidic mechanism behind the flow structures to be far from clear, and attributed the formation of the off-center peaks to the sharp corners associated with rectangular slot jets, and the physical boundaries of their model.

Although these off-center peaks can be found to induce higher local heat transfer coefficients, they may also compromise the efficiency of impinging jets by inducing large temperature gradients along the long axis of the jet. Consequently, these may result in possible thermomechanical stresses within the microelectronics assembly, and eventual failure. Despite this however, there still exists much conjecture and disagreement as to the exact cause of these fluidic phenomena in laminar slot jets, and most work to date has been confined to numerical studies with low Prandtl number working fluids. In Chapter 4 of this thesis the presence of off-center peaks such as those described above are observed in the investigation

of low Reynolds number liquid slot jets. From the results of the heat transfer and flow velocimetry techniques utilised, conclusions are drawn upon the formation of these peaks.

2.4 Passive Structures

As mentioned in Section 2.1.4 for impinging jets, passive control devices involve the implementation of a structure at the jet exit to break down vortical flow structures, impacting jet shear layer spreading – which consequently allows for control and enhancement of surface heat transfer coefficients [97]. Iwana *et al.* [98] investigated the heat transfer and flow characteristics induced by four triangular tabs situated around the outlet of an axisymmetric jet. They found that for a fixed Reynolds number of 39,000 based on the pipe diameter, triangular tabs resulted in a strong longitudinal vortex formation, and stretching of the jet shear layer; enhancing mixing and diffusion of the jet. This in turn resulted in a 15% enhancement in local Nusselt number over the standard case. Gao *et al.* [99] performed experiments to characterise the heat transfer enhancement produced by arrays of 6, 10, and 16, 45° triangular tabs, at various protrusion distances into the flow field, at a Reynolds number of 23,000. They found that for fixed protrusion distances, the application of the tab arrays produced distinct regions of heat transfer enhancement due to localized velocity peaks between the tabs. In terms of heat transfer enhancement, the greater the number of tabs in the array, the greater the stagnation point and area-averaged Nusselt numbers. However, increasing the number of tabs in an array results in increased hydrodynamic losses, due to the associated higher pressure drops through the nozzle. By examining the pressure drops of the individual tab arrays and protrusion distances, Gao *et al.* [99] found that increasing the protrusion distance rather than the number of tabs in an array is a more effective means of heat transfer enhancement, as equivalent Nusselt numbers can be achieved for a lower head loss coefficient (K). Hayashi *et al.* [100] also investigated arrays of 2, 4 and 6 triangular tabs for three tab pitch angles of 45, 90 and 135° into the flow stream. For a fixed tab protrusion distance of 0.1D, a blockage ratio of 1.45%, and a Reynolds number of 39,000, the results indicated that a tab pitch angle of 90° promotes greatest area-averaged

heat transfer. As with Gao *et al.* [99], Hayashi *et al.* [100] also concluded that the greater the number of tabs, the higher the enhancement in heat transfer and, also, the more evident creation of distinct regions of peak Nusselt number corresponding to localized velocity peaks. It is important to note that all three studies utilised the orifice diameter as the length scale for all non-dimensional numbers, and this remained constant for the geometries with tabs.

The previous studies have investigated the influence of passive tabs on jet impingement heat transfer, but they have been limited to turbulent axisymmetric nozzles, which featured a very different flow structure to laminar slot jets [21]. The use of passive tabs in slot jets has been predominantly motivated by the field of jet propulsion in supersonic jets, as the effect of tabs on vortex evolution and shear layer growth has been found to suppress jet screech noise, enhance combustion efficiency and allow designers more control over thrust vectoring [21; 101; 102; 103; 104]. From a review of the literature, it was found that the application of passive structures can provide heat transfer enhancements for confined circular jets, and also – when applied to non-circular jets – passive structures promote the growth of vortical structures and the mixing characteristics of these jets. However, the impact of these passive structures on the temperature and velocity flow fields, of low Reynolds number, confined microscale slot jets, is still an open research question.

2.5 Closure

As discussed in this chapter, the thermal and hydrodynamic behaviour of impinging jets is dependent on many design variables. For the design of a microscale system required for the TIPS project, these design variables have been limited to nozzle geometry modifications. Slot jets offer compelling advantages, due to their proven enhanced mixing and entrainment, and geometric compatibility with the PIC package. However, from the literature to date, very little is understood of the behaviour of low confinement, submerged, liquid slot jets. This study aims to investigate the thermal and hydrodynamic behaviour of slot jets subject to the following fixed design limitations:

- Laminar flow, with Reynolds number ranges based on the hydraulic diameter of $100 < Re_{Dh} < 500$ [73; 76; 87].
- A jet confinement plate to impingement surface ratio (H/D_h) of 1, which will potentially result in the presence of potential core impingement.
- Deionised and degassed water as the working fluid, due to the beneficial thermophysical properties for microelectronics cooling applications.

In order to identify any means of passive control and enhancement, the nozzle geometries were varied. Based on a review of the literature, it was identified that there were gaps in the understanding of nozzle aspect ratio, and the application of passive structures on the temperature and velocity flow fields of confined, submerged, impinging slot jets. Prior to their application in a microfluidic cooling solution, a full thermal and hydrodynamic characterisation is required. The objective of characterisation is to identify any possible enhancements in heat transfer achieved through nozzle geometry modification, the hydrodynamic penalty of such enhancements, and the fluidic mechanisms which resulted in these. The experimentation techniques utilised in achieving the required thermal and hydrodynamic characterisation – as well as details of the tested nozzle geometries – are presented in Chapter 3.

Chapter 3

Experimental Methods

This chapter presents the experimentation and measurement techniques utilised to investigate the passive control and enhancement of a normally impinging, submerged and confined slot jet – through jet nozzle geometry modification. For thermal characterisation, the local and area-averaged heat transfer distribution across the impingement surface was measured through the application of the Joule-heated foil technique. For hydrodynamic characterisation, Particle – Image Velocimetry (PIV) and pressure-flow measurements allowed for the instantaneous and time averaged local velocity flow fields, along with the associated head losses, to be recorded. The experiments were carried out over a Reynolds number range based on the slot jet hydraulic diameter (D_h) of 100 to 500. The following sections detail the investigated slot jet geometries, experimental test facilities, data reduction, and uncertainty analyses.

3.1 Test Specimens

Due to the spatial resolution limitations of each experimental technique – as well as the cost and complexity of microscale fabrication techniques – the length scale of the test specimens was varied for each characterisation method. As the measurement of pressure drops associated with low Reynolds number milliscale systems can be quite low ($<$ 50 Pa), the test specimens were designed such that the recorded values would be sufficiently high to minimize experimental uncertainties in differential pressure measurement. For the PIV measurement

facility, however, uncertainties are dependent on many factors, such as the laser sheet thickness (≈1mm). Consequently, the nozzle geometries were designed with these limitations in mind. To enable geometric compatibility between the characterisation techniques – as well as the extrapolation of correlations – the results were presented in terms of relevant non-dimensional numbers. Reynolds scaling techniques allow for the comparison of the results, and to predict the thermal-hydraulic behaviour of the geometries when applied in a microfluidic system. For all dimensionless parameters, the hydraulic diameter of the slot jet (D_h) was chosen as the characteristic length scale and calculated using eq. (3.1):

$$D_h = 2LW/(L+W) \tag{3.1}$$

The hydraulic diameters were 4mm, 1mm, and 10mm for the Joule-heated foil, pressure drop and PIV measurement facilities, respectively. All slot jets tested were manufactured from orifice plates, with a thickness to hydraulic diameter ratio (t/D_h) of 1.

1. **Jet Nozzle Aspect Ratio**: For the investigation into the influence of slot jet nozzle aspect ratio, which is discussed in Chapter 4, five different nozzle geometries were chosen, and these are detailed in Table 3.1. For the heat transfer and velocimetry experiments, the samples were manufactured from Polycarbonate using a Datron M7HP CNC milling machine. The pressure drop test specimens were laser cut from 1mm thick 304 Stainless Steel using an LPKF G 6080 stencil cutting system.

2. **Tabs & Chevrons**: For the investigation into the influence of jet outlet structures in Chapter 5, six different nozzle geometries were tested and detailed in Figure 3.1. The test specimens included five different tab structures of varying geometry, and a conventional slot jet for comparison. These nozzle geometry designs were based on a review of the literature; more specifically, Zaman *et al.* [102] for the spreading characteristics of non-circular jets, and Violato *et al.* [105] and Zaman *et al.* [106] for their investigations into chevron technology on nozzle outlets. Detailed tab geometries and their associated flow blockages ($\beta = (A_{tab}/A_{slot})$) are presented in Figure 3.1 and

Table 3.2. For the Joule-heated foil and PIV experiments, the test specimens were manufactured out of ABS with a Viper Si2 stereo-lithography machine (rated resolution of $\pm 2.5 \mu m$). The test specimens were then fixed in a polycarbonate orifice plate for testing. The pressure drop specimens comprised two plates: the first was a slot jet with an aspect ratio of 4 as the base plate, and the second was a 0.25mm thick plate containing the outlet structures. For each test, the plate with the outlet structure was fixed on top of the base plate. As with the base plate, the plates containing outlet structures were also laser cut from 304 Stainless Steel using the LPKF G 6080 stencil cutting system.

Table 3.1: Geometries off all investigated test specimens for the aspect ratio study.

Aspect Ratio	1	2	4	6	8
PIV ($D_h = 10mm$)					
Length (mm)	10	–	25	–	–
Width (mm)	10	–	6.25	–	–
Heat Transfer ($D_h = 4mm$)					
Length (mm)	4	6	10	14	18
Width (mm)	4	3	2.5	2.33	2.25
Pressure Drop ($D_h = 1mm$)					
Length (mm)	1	1.5	2.5	3.5	4.5
Width (mm)	1	0.75	0.63	0.58	0.56

Table 3.2: Jet nozzle configuration and flow blockages for the passive structures.

Configuration	β
Baseline	0
Minor double tabs	0.1
Minor triangle	0.125
Major triangle	0.15
Major chevron	0.2
Major contours	0.295

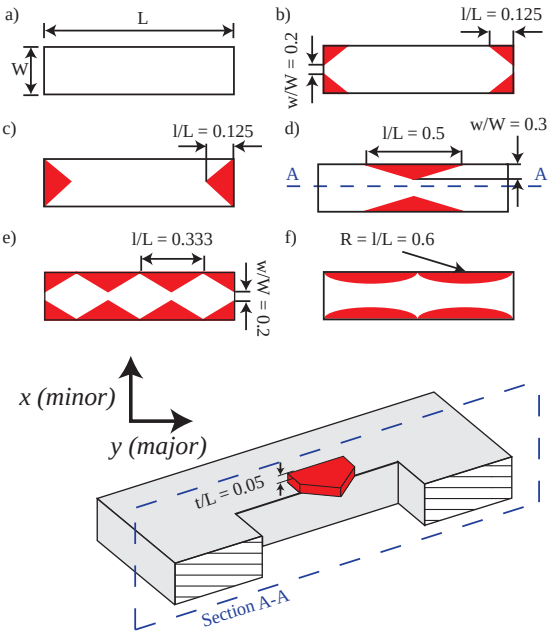

Figure 3.1: Schematic of tab geometries and locations for a) non-tab case, b) minor double tabs, c) minor triangle, d) major triangle, e) major chevron, and f) major contour.

All investigated geometries were verified using an Axioscope Zeiss microscope, a Hitachi TM-1000 Scanning Electron Microscope (SEM), and a Mitutoya digital calipers. Section 3.1 provides a sample image of the slot jet specimens for the (a) PIV (b) heat transfer and (c) pressure drop measurement facilities.

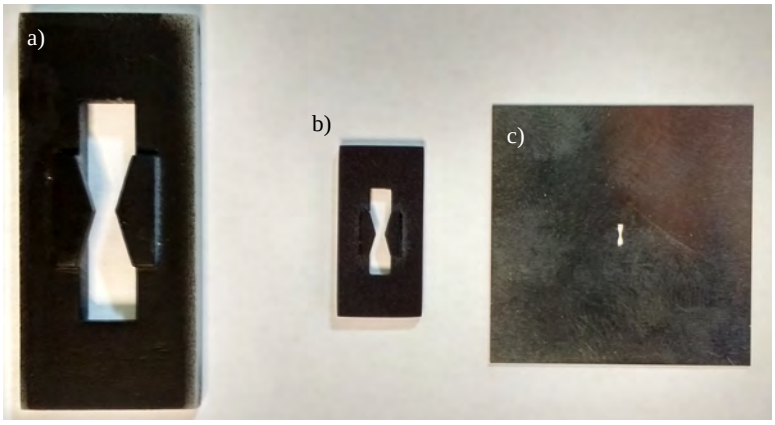

Figure 3.2: Example test specimens for the (a) PIV, (b) heat transfer and (c) pressure drop measurement facilities.

3.2 Velocimetry

PIV was used to capture the instantaneous and time-averaged 2D velocity flow fields, in order to understand the fluid dynamics associated with confined, submerged, impinging slot jets. By introducing tracer particles into a flow, a 2-D velocity vector field can be captured along a specified plane through the application of a high-power light source perpendicular to the plane and a Charge-Coupled Device (CCD) camera. Typically, Nd:YAG lasers are applied as the light source due to their ability to provide pulses of constant energy over a duration in the order of nanoseconds. The light source illuminates the plane twice, via two pulses separated by a specified time interval (Δt). The light scattered by the tracer particles is then captured over two frames, or one image pair, by the CCD. The investigated flow field is then divided into interrogation regions of sufficient size, and the displacement of a single tracer particle ($\Delta \boldsymbol{x}$) within the interrogation region can then be used to generate a local velocity vector ($\Delta \boldsymbol{x}/\Delta t$). The velocity vectors within each interrogation region can then be compiled to generate an instantaneous velocity vector field; and recording multiple image pairs allows for the analysis of time-averaged velocity vector fields. PIV offers many advantages as a non-obtrusive means of measuring the whole flow field, however, like any flow measuring technique, PIV does have associated disadvantages. Examples of such disadvantages are:

- The same time interval (Δt) between images is applied to the whole flow field, which can result in insufficient pixel displacements in low velocity regions.
- For highly three-dimensional flows, out-of-plane motion can become an issue, and result in interference in the measured data.

The setup of the PIV measurement facility, as well as the experimental procedure and methods to minimise the uncertainties in velocity measurement, are detailed in the following section.

3.2.1 Setup & Procedure

The PIV measurement facility is detailed in Figure 3.3. The PIV system comprised a Litron Nano L PIV double cavity Nd:YAG laser, 2 LPU1000 laser power

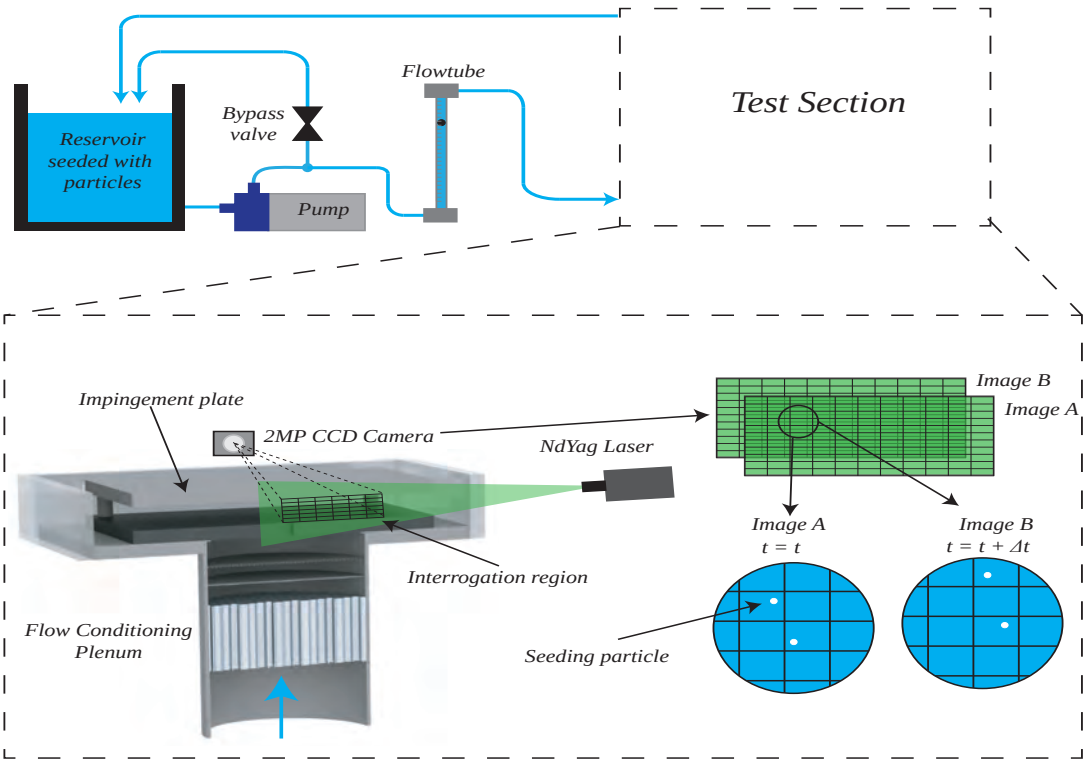

Figure 3.3: PIV experimental test facility.

supplies, a TSI Powerview 2 MP (30 Hz) camera, a 64 bit frame grabber, and a TSI laser pulse synchronizer (model no. 610035). A Sigma 105 mm f2.8 macro lens was used in conjunction with the CCD camera. The Litron laser emits 50 MJ of energy per pulse, over a duration of 5 – 9 ns and a wavelength of 532 nm. The 2D light sheet was generated from the laser beam through the application of spherical and cylindrical lenses, and the resulting light sheet had a thickness of ≈1mm at the focal length distance from the spherical lens (0.5m). TSI's Insight 3G software platform was then used for laser pulse control, camera synchronization, and image capturing and processing. The requirements for PIV tracer particles are that they must:

- Follow the flow accurately with a lag time lower than that of the flow time scales to avoid any false flow field behaviour.
- Have a density close to that of the working fluid to avoid particle settling within the captured planes.
- Provide the required intensity in light scattering to be captured by the CCD.

Silver coated hollow glass spheres with mean diameters of 10μm supplied by Dantec Dynamics were found to meet these criteria, and were utilised as the flow tracer particles.

Using a Totton DC40/10 centrifugal pump, water (Prandtl number of 6.78) containing a homogeneous mixture of tracer particles was drawn from a reservoir and pumped via a flow conditioning plenum into the test section. The water was deionised and degassed to prevent nucleation at the impingement surface. The plenum also contained flow straightening devices to minimize flow non-uniformities, such as turbulent eddies and lateral velocities [107] (see Section 3.2.2). To allow fine control of the mass flow rates, a bypass valve was used in conjunction with the power supply for the centrifugal pump, and the mass flow rates were recorded using a Cole-Parmer direct-reading flow tube. The specimens were fixed above the flow conditioning plenum using a rubber gasket to ensure a watertight seal. For this study, two types of PIV configurations were utilised

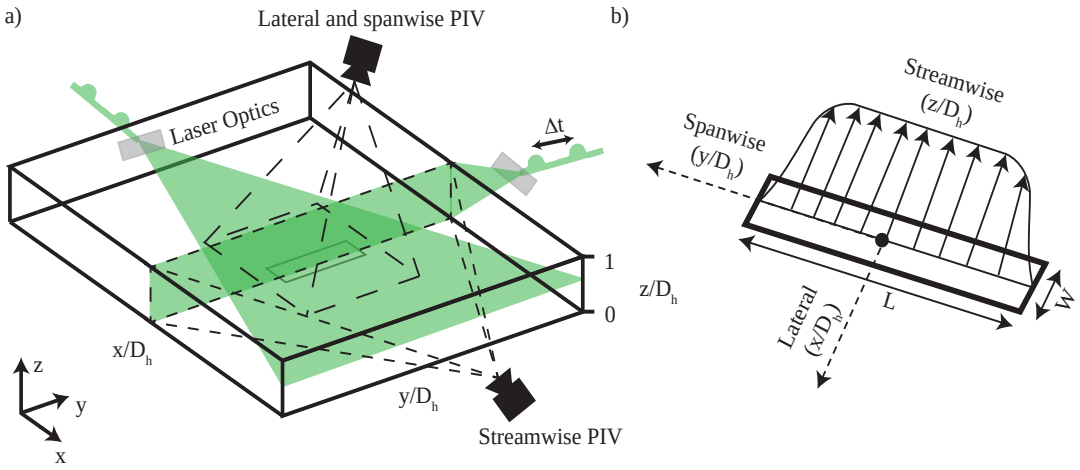

Figure 3.4: a) PIV investigation domain and b) flow field coordinate system.

to allow for velocity vector fields along the *xz, yz* and *xy* planes to be captured. These configurations were labelled as streamwise, and lateral and spanwise PIV, and are detailed in Figure 3.4 (a).

The are many PIV measurement parameters which will influence the validity of the resulting velocimetry data and these include: the time intercal between laser pulses; interrogation spot size; laser sheet thickness; particle size and concentration; length between each pixel (determined by camera magnification and resolution). With these paramters considered, the following guidelines established by Keane and Adrian [108] and TSI [109] were strictly adhered to:

- The interrogation region was chosen of sufficient size so that one vector reliably described the flow within that window.
- In-plane displacements of >25% of the interrogation region were avoided.
- Minimum in-plane displacement should be 2 particle image diameter.
- Out-of-plane displacements of >25% of the laser sheet thickness were avoided.
- The camera exposure and laser power should be balanced to provide clear particles in the images.

The PIV experimental parameters for both orientations are presented in Table 3.3. The number of image pairs captured was based on the application of the statistical analysis for time-averaged PIV presented by Stafford et al. [110], and further detailed in Section 3.5.3. For the Lateral and Spanwise PIV configuration, 250 image pairs was deemed more than sufficient, as the flow field captured is in the laminar flow regime, with the absence of any large velocity gradients and negligible turbulence intensities.

Table 3.3: PIV measurement parameters.

PIV Parameter	**Streamwise (*xz*,*yz*)**	**Lateral & Spanwise (*xy*)**
$\Delta t(\mu s)$	2,000 – 6,500	5,500 – 9,500
Interrogation region (pixels)	16 x 16	32 x 32
Investigated region (mm)	10 x 50, 10 x 30	30 x 30
Image pairs (-)	500	250
Capture frequency (Hz)	30	30

3.2.2 Flow Conditioning

In order to ensure high quality flow entering the orifice plates – that is flow free of turbulence and non-uniformities – it was necessary to implement a plenum or stagnation chamber containing flow conditioning devices upstream of the orifice plate. The use of plenums for impinging jet systems is known to dampen supply pressure oscillations, smooth supply velocity and temperature profiles, and can form an important part of the impinging jet system structure [27]. The plenum for this study contained two different flow conditioning devices: a honeycomb, and screens. Honeycombs are effective flow straightening devices which work by suppressing cross-stream or lateral components of turbulence by breaking up eddies larger than the cell size, thus increasing the rate of eddy decay. For complete turbulence suppression, a honeycomb matrix length of 5 to 10 cell diameters is recommended [107].

Flow conditioning screens were first proposed by Prandtl and, like the honeycomb, can reduce lateral velocity components. However, they are far more effective at reducing flow non-uniformities by imposing a static pressure drop proportional to the approaching velocity squared. Increased efficacy can be achieved

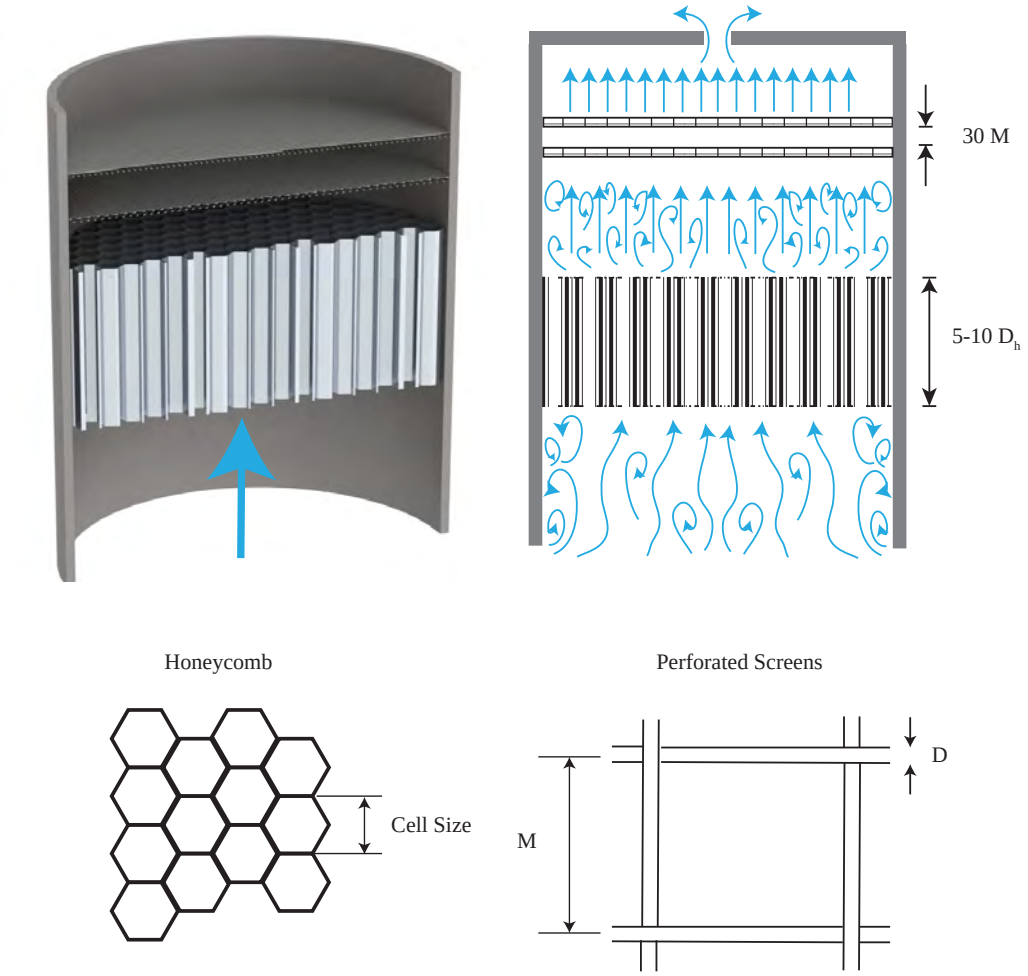

Figure 3.5: Sectioned views of the flow conditioning plenum, detailing the location and design of the flow conditioning devices.

by cascading multiple flow conditioning screens, but taking care to maintain a gap of 30 mesh sizes (M) between each screen – to ensure the sufficient decay of wire generated turbulence [111].

For the PIV measurement facility, a honeycomb device with cell size smaller than the smallest jet diameter, and a cell length of between 5 to 10 cell diameters based on the hydraulic diameter, was located upstream of two cascading screens, and is illustrated in Figure 3.5. The screens were then spaced at least 30 mesh sizes apart. Wieghardt's [112] formula for determining head loss coefficient (K)

through screens is accepted as the most satisfactory method, and is given by:

$$K = 6.5(\frac{1-\xi^2}{\xi})Re^{-\frac{1}{3}} \tag{3.2}$$

Where ξ is the porosity of the screens, which is based on the mesh size (M) and wire diameter (D):

$$\xi = (1 - \frac{D}{M})^2 \tag{3.3}$$

A screen with a loss pressure drop coefficient of at least two is recommended for removal of almost all longitudinal velocities [113], and this criteria was achieved for the flow conditioning plenum implemented.

3.2.3 Data Reduction

As previously mentioned, the TSI Insight 3G software platform was used to capture and process the raw image pairs (image A and image B), in order to produce instantaneous velocity vector fields. The data reduction within Insight 3G consisted of two steps. The first was to define the studied flow field into cartesian coordinates and determine the particle displacements within each grid using the available plug-in engines. The second step was to assess the validity of the resulting velocity flow field using post-processing techniques. These steps are further detailed below:

- **Image processing**: The first step in the image processing was to initialise the vector field for processing. A Nyquist grid engine was utilised, and images A and B were divided into a series of smaller spots or interrogation regions. The dimensions of these regions are detailed in Table 3.3, and the Nyquist grid engine within Insight 3G used a 50% overlap. To condition the spots for processing prior to image cross-correlation, a Gaussian spot mask engine was then applied. The spot mask engine multiplied the individual spots in images A and B by a weighting function, to make the center of the spot brighter and the edges darker – increasing the signal to noise ratio in the cross-correlation step. A Fast Fourier Transform (FFT) algorithm was then implemented to compute the cross-correlation between spots A and B. The resulting correlation map contained a correlation peak describing

the displacement vector between spots A and B, in pixels. The final step was a Gaussian peak engine, which located the peak within the correlation map to within sub-pixel accuracy, by fitting a Gaussian curve to the highest pixel and its four nearest neighbors. The application of a Gaussian peak threshold then allowed for any possible spurious peaks or vectors to be disregarded in the processing pass. Each interrogation region generated a single instantaneous displacement vector, and applying the processing pass to each region produced a field of displacement vectors.

A spatial calibration was completed to allow for the length of a pixel to be referenced against a known length scale and, therefore, giving a method to convert the displacement vectors to velocity (mm/s). This was achieved by capturing an image of a ruler within the measurement plane, and is detailed in Figure 3.6.

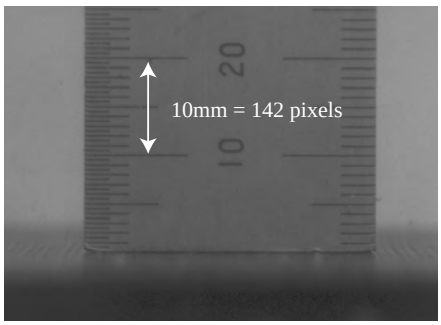

Figure 3.6: Ruler placed within the PIV measurement plane to allow for the spatial calibration within Insight.

- **Image post-processing**: With PIV it can be difficult to isolate and prevent the occurrence of some erroneous velocity vectors. These inaccurate vectors can be caused by reflections between the laser light sheet and the bounding walls, or through the seeding particles joining together into cluster formations – which will have a negative impact on particle advection. Consequently, a PIV post-processing pass was also implemented to evaluate the validity of the velocity vector fields produced by the processing steps detailed previously. The post-processing steps utilise two tools: local vector validation, and vector conditioning. The local vector validation

step assesses a 3 x 3 vector neighborhood around each vector against a user defined velocity threshold, which was configured to be the median of the velocities within this neighborhood. If the difference between the local vector and the reference vector is greater then the defined threshold, the local vector is considered to be invalid. Over the same neighborhood size, the vector conditioning tool then fills holes left in the velocity vector field. These holes were present because of failed signal to noise ratios in the image processing, or were considered to be invalid by the previous vector validation step. It is important to note that PIV post-processing steps were only implemented as a means of replacing a small number of invalid vectors. In cases where large holes existed in the vector field due to factors such as in-plane and out-of-plane motion, or low seeding densities, the test configuration was repeated until satisfactory conditions were achieved.

Upon completion of the processing steps, the instantaneous local velocity components ($u,\ v,\ w$), as well as their spatial coordinates ($x,\ y,\ z$), were exported. With Matlab, the instantaneous (U) and time-averaged velocity magnitudes ($\bar{U}$) were then determined using eqs. (3.4) and (3.5), respectively:

$$U = \sqrt{u^2 + v^2} \tag{3.4}$$

$$\bar{U} = \frac{1}{N} \sum_{i=1}^{N} U_i \tag{3.5}$$

Where N represents the number of captured image pairs.

The jet exit Reynolds number for all tested geometries was based on the hydraulic diameter and was given by eq. (3.6):

$$Re_{Dh} = \frac{\rho U_{Mean} D_h}{\mu} \tag{3.6}$$

Where U_{Mean} was the mean jet exit velocity.

3.2.4 Rig Characterisation

No applicable correlations exist for the velocity field distributions of low Reynolds number, confined, liquid slot jets. Therefore, a numerical model was developed using Star CCM+ version 9.06, a commercial CFD package [114]. Within Star CCM+, a three-dimensional model of the PIV facility was constructed. A mesh sensitivity study was carried out to ensure grid independence, and a steady state three-dimensional laminar simulation was performed using a segregated solver. Water at 25°C was used as the working fluid, and the properties were taken from Holman [71]. The geometry of the numerical model, including inlets and outlets, were maintained as close as possible to that of the experimental measurement facility, and detailed in Figure 3.7 (a). The mesh applied to the numerical domain, as well as the results of the corresponding mesh sensitivity study, are detailed in Figure 3.7 (b) and Table 3.4. The boundary conditions applied to the numerical model were:

- A constant mass flow boundary was applied at the inlet to the flow conditioning plenum, 35mm upstream of the orifice plate.
- A symmetry plane boundary was applied along the mid-section of the model to mirror the mesh and boundaries about the mid-plane, and to reduce computational time.
- A pressure outlet condition was applied at the flow outlet boundary.

The numerical model was then run until it achieved adequate convergence levels, detailed in Figure 3.8. Figure 3.9 plots (a) experimentally measured and

Table 3.4: Mesh sensitivity analysis for assessment of the PIV measurement facility.

Mesh	No. of cells	Difference in $\bar{U}_{Max}$ (%)
1	0.64 x 10^6	0.8%
2	1.44 x 10^6	0.1%
3	2.8 x 10^6	0.09%
4	4.5 x 10^6	0%

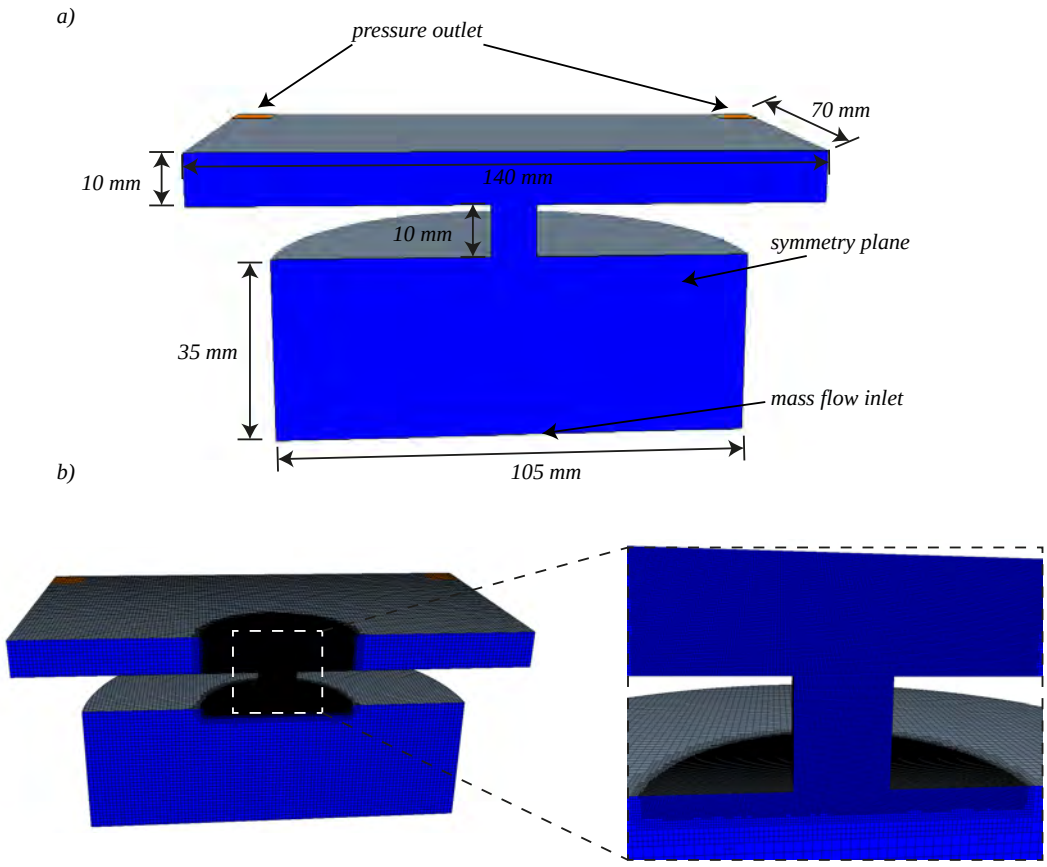

Figure 3.7: a) Geometry of PIV measurement facility modeled within Star CCM+ and b) Meshing criteria applied to the numerical model.

(b) numerically predicted velocity flow fields within the stagnation zone, and the initial formation of the wall jet zone. By examining the percentage difference between the two flow fields, in Figure 3.9 (c), it can be seen that the majority of velocities captured with the PIV facility are within the 9.4% maximum experimental uncertainty in the measurement of velocity (See Section 3.5.3). The highest % differences recorded are in areas of low or insignificant jet velocities, such as near-wall measurements, or in the jet shear layer and ambient surrounding fluid. Factors which could contribute to this variance include the assumptions in the numerical model – such as the use of a laminar viscous regime limiting the ability to capture any possible turbulent fluctuations in the jet shear layer – and

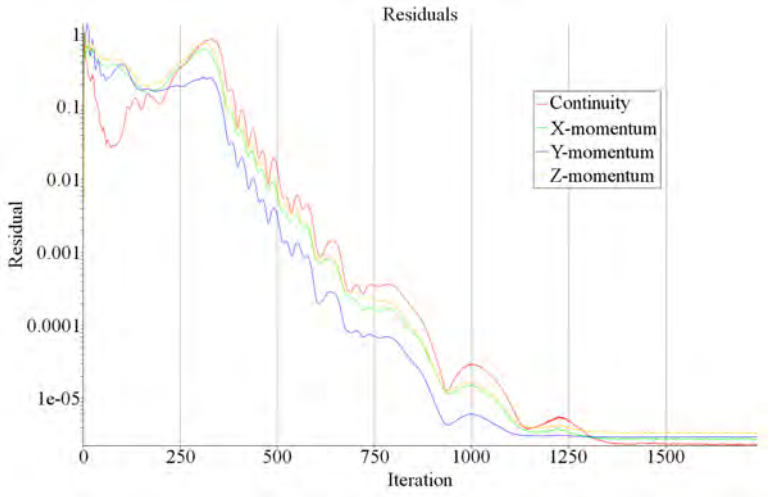

Figure 3.8: Convergence levels of the numerical simulation within Star CCM+, with respect to the number of iterations.

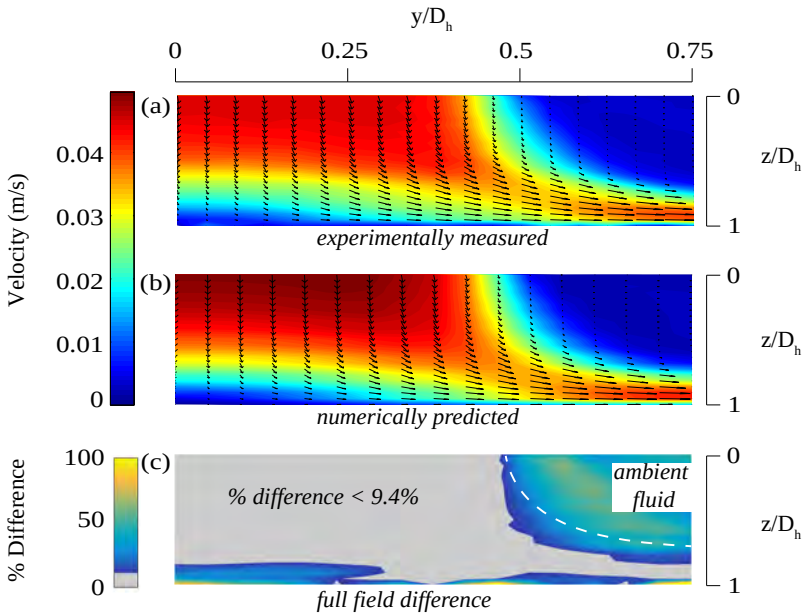

Figure 3.9: Assessment of the (a) experimentally measured flow field against (b) a numerical model, and (c) the % difference between the experimental and numerical results, for a slot jet with aspect ratio of 1 and a Reynolds number of 400.

the limitations of PIV in capturing near wall velocities. As a consequence, the PIV measurement facility was deemed to be sufficient in capturing the impinging and wall jet velocity flow fields. It is also important to note that CFD was used as a tool to assess the experimental measurement facility and, as such, discussion of the results in the following chapters are confined to what was recorded using the experimental measurement facility.

3.3 Heat Transfer Measurement Facility

3.3.1 Setup & Procedure

This section details the apparatus and procedure utilised for the Joule-heated foil test facility. The objective of the experimentation was to determine the convective heat transfer coefficient of low Reynolds number, confined, impinging slot jets, by measuring: power input to the foil, foil temperatures, and fluid mass flow rate. The experimental test facility used in this investigation is detailed Figure 3.10. The test facility comprised a closed loop pumping system with water as the working fluid. The fluid was deionized and degassed and a Lauda RE 104 water bath was used as the system reservoir, as it had both heating

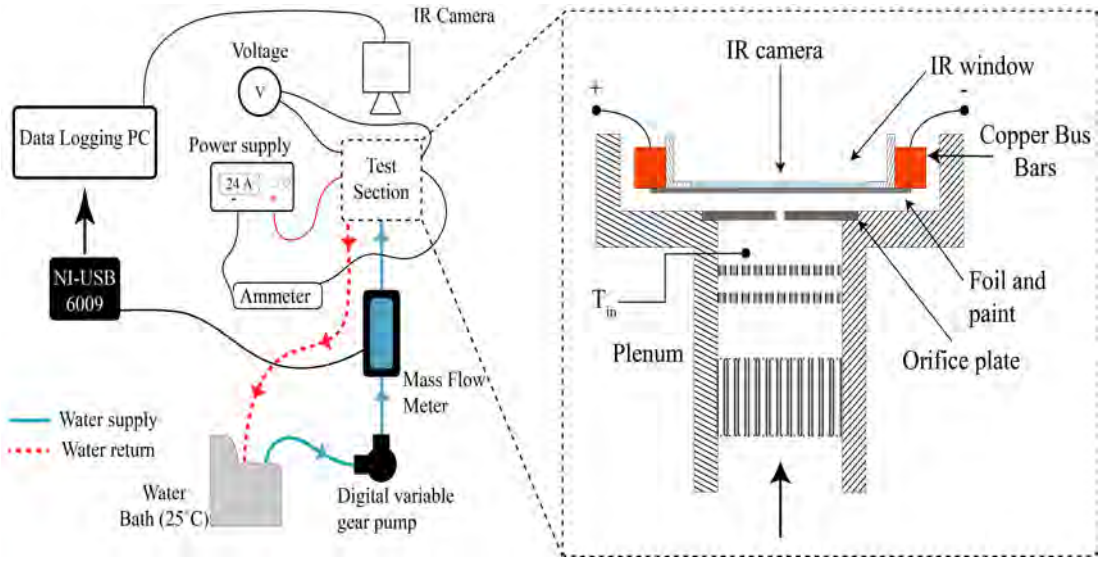

Figure 3.10: Configuration of the local heat transfer measurement facility.

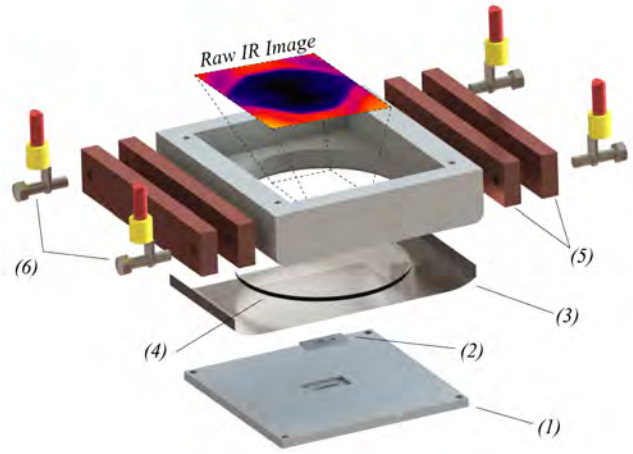

Figure 3.11: Detailed view of the heated thin-foil test section (1) nozzle orifice plate, (2) 3D printed tab, (3) stainless steel foil, (4) IR transparent glass, (5) copper bus bars, and (6) electrical input and tightening screws.

and chilling functionality to maintain the fluid reservoir temperature at 25°C. The fluid was supplied to the test section via a Cole-Parmer digital variable gear pump, and mass flow rate was recorded with a Bronkhurst Liqui-Flow mass flow meter (0 - 10 kg/hr). Prior to entering the test section, the flow passed through a flow conditioning plenum. The flow conditioning plenum was designed using the criteria detailed in Section 3.2.2, and had a cross-sectional area 108 times that of the largest jet nozzle, so that velocity in the plenum could be considered negligible compared to that at the jet exit. The heated thin foil test section consisted of a submerged and fully confined slot jet, normally impinging on $12.5\mu m$ thick stainless steel foil. Stainless steel foil was chosen as its high electrical resistivity promotes sufficient heat generation, while its low thickness and thermal conductivity (16.3 W/mK) limits lateral conduction in the foil – to produce a near isoflux condition for the experiment.

To capture the local temperature distribution of the heated foil, it was fixed over a Fluke C-Range 75mm infrared (IR) transparent window of high transmissivity ($\tau \approx 0.94$) [115]. The window was of sufficient area ($\approx 5 - 7D_h$) to determine heat transfer in the stagnation and wall jet regions. A layer of matte black paint separated the boundary of the foil and the IR window, to create

a high-emissivity diffuse surface for IR detection. A Flir Merlin series infrared camera, using ThermCAM Researcher 2.8 for image capturing and analysis, was then fixed above the heated foil test section. The gear pump was activated and a power input (≈138W) was supplied to the foil via the copper bus bars and a Sorensen DCS 80-37 power supply. For each investigated flow rate, the IR camera was configured to capture 250 images per sequence at a temporal resolution of 50Hz. The voltage drop across the foil and current input were recorded with a Fluke 45 digital multimeter and a Tenma 72-6185 clamp meter, respectively. The jet inlet temperatures (T_{in}) and the fluid mass flow rates were recorded with a data acquisition card and logged with LabView.

3.3.2 Data Reduction

This section details the steps taken to present the primary experimental heat transfer data in terms of the required non-dimensional terms. To assess the Joule-heated foil technique, an analysis was carried out on the heat flow through a single element of the foil subjected to the lowest recorded flow rate, similar to the analysis implemented by Stafford *et al.* [116]. The area of the studied element was equal to one pixel captured by the IR camera (0.333mm x 0.333mm) – containing the stainless steel foil, the layer of matte black paint, and the IR glass, as illustrated in Figure 3.12. The objective of the analysis was to isolate the heat transfer mechanisms present within the element, in order to accurately obtain the local forced convective heat transfer coefficient required to calculate Nusselt number. To effectively do so, any heat losses through the element via the secondary modes of heat transfer, such as conduction and radiation, had to be accounted for.

Based on an energy balance conducted using the heat flow map illustrated in Figure 3.12, the convective heat transfer rate (q''_{cv}) along the impingement surface was defined as eq. (3.7):

$$q''_{fc} = q''_{in} - q''_{c-nc-r} + q''_{lc} \tag{3.7}$$

Where q''_{in} is the heat flux generated within the foil through Joule-heating ($\mathrm{VI/A}_f$), and the losses via conduction through the foil-paint-glass and natural convection

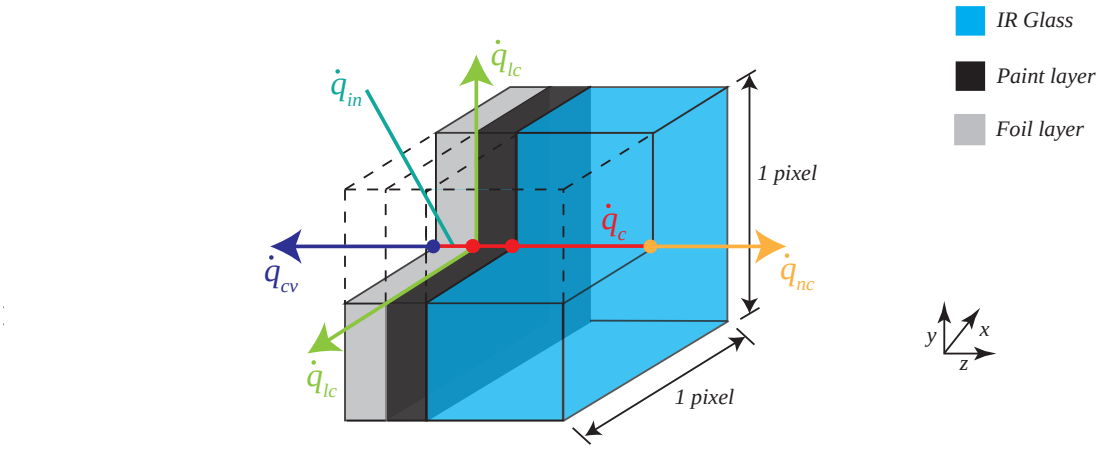

Figure 3.12: Analysis of the Joule-heated foil technique, by investigating a single pixel element, captured by the IR camera.

to the surroundings (q''_{c-nc-r}), as well as lateral conduction between elements (q''_{lc}), are also included.

To calculate the losses via conduction, it was necessary to know the thickness and thermal conductivities of the foil, paint, and glass layers, respectively. The thickness of the glass was recorded with a Mitutoya digital calipers and found to be 4mm. The IR glass was determined to be made from magnesium aluminate, or spinel, a commonly used material in high performance optical components, such as lenses and IR windows. However, no value for the thermal conductivity or the precursor powders and sintering techniques were supplied by the manufacturer. The thermal conductivity was taken to be 13.4 W/mK, based on the investigation of the mechanical and thermal properties of spinel conducted by Sanghera *et al.* [117]. The thermal conductivity of the Stainless Steel foil was given by the manufacturer as 16.3 W/mK [118], and Raghu and Philip [119] determined the thermal conductivity of matte black paint as 1.38 W/mK. In order to accurately capture the thickness of the foil and paint layers, a section of the painted foil was clamped in a specimen holder, covered in epoxy resin, and ground and polished, to allow for it to be examined under an optical microscope. A silicon reference piece was used as a spatial calibration for this analysis, with the length of the reference piece measured using a Hitachi TM-1000 SEM, and detailed in Figure 3.13 (a).

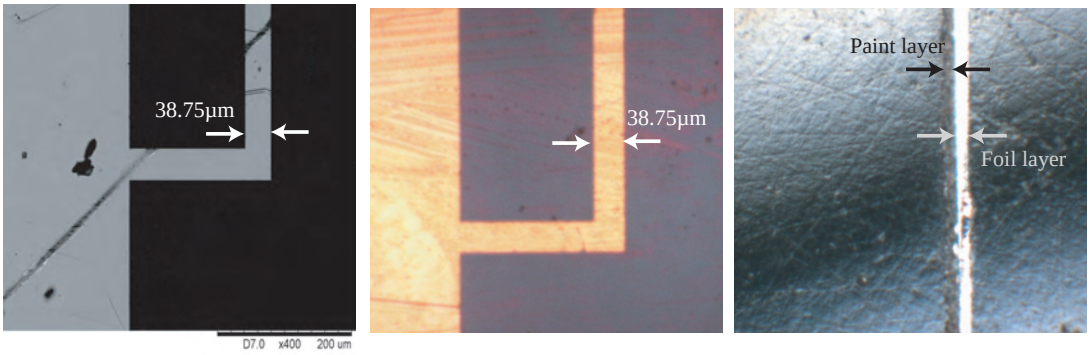

Figure 3.13: a) Silicon reference length in SEM microscope b) Silicon reference length in optical microscope c) Cross-section of foil and paint layers in optical microscope.

The silicon reference piece and the foil and paint cross-section were then viewed under an Axioskopp Zeiss microscope with a CCD camera, and the captured images shown in Figure 3.13 (b) and (c). The thickness of the foil and paint layers were found to be $t_f = 13.7\mu m$ and $t_p = 19.2\mu m$, respectively. Even though there would be deviations in the thickness of the paint layer across the foil, it was deemed to be acceptable to neglect these and assume a constant thickness for the calculation of conduction in the paint layers due to the low thermal conductivity of the paint. This was proven to be acceptable by Stafford [120].

From a thermal resistance analysis (detailed in Appendix B), the relatively high thermal resistance ($\sim 10^6$ °C/W) associated with the losses through conduction and natural convection (q''_{lc}), resulted in them representing ~0.1% of q''_{in}. They were therefore determined to be negligible. The losses through lateral conduction would be relatively small due to the thermal differential between foil elements, nonetheless, they were still included in calculating the convective heat transfer coefficient and were determined using the method presented by Stafford *et al.* [116]. They stated that once the thermal conductivity (k_f, k_p) and thickness (t_f, t_p) of both the foil and paint layers are known – and the Biot number is sufficiently small (< 0.1) so that the foil and paint layers have uniform temperature fields – the lateral conduction in a heated thin-foil experiment can be given

as:

$$q''_{lc} = (k_f t_f + k_p t_p)(\frac{\partial^2 T_W}{\partial x^2} + \frac{\partial^2 T_W}{\partial y^2}) \tag{3.8}$$

The convective heat transfer coefficient (h) was then determined using eq. (3.9), where T_W and T_{in} are the wall and jet inlet temperatures, respectively:

$$h = \frac{q''_{fc}}{T_W - T_{in}} \tag{3.9}$$

With the Nusselt number given by eq. (3.10):

$$Nu_{Dh} = \frac{hD_h}{k} \tag{3.10}$$

The area-averaged Nusselt numbers were taken as the average of the local Nusselt number distributions over an area of $576mm^2$ along the impingement surface – based on a square with sides of length $6D_h$.

3.3.3 Rig Characterisation

To effectively capture IR images, the camera required an accurate measurement of object surface emissivity corrected for environmental conditions, specifically the atmospheric transmittance between the test section and the camera, including the IR glass. The most effective method of correcting for all atmospheric and surface influences on the captured image sequences was deemed to be an *in situ* calibration of the IR camera, similar to the methods utilised by Sargent [121] and Waddell *et al.* [122]. For the calibration, three thermocouples were referenced to a Fluke 1504 thermistor probe (uncertainty of ±0.01K, see Figure C.6) and fixed to the center of the impingement surface. The experimental rig was configured as it would be for testing, and water was pumped into the test section at 12 different temperatures between $20 - 75°C$ – which were set using the Lauda RE104 water bath. Once thermal equilibrium was reached, a sequence of 250 images was captured with the thermal camera and the temperatures of the three thermocouples were logged. The averaged raw IR data for each sequence was then plotted against the combined average of the three thermocouples – which had a variance of $< 10^{-4}$ K – and a fourth degree polynomial calibration curve

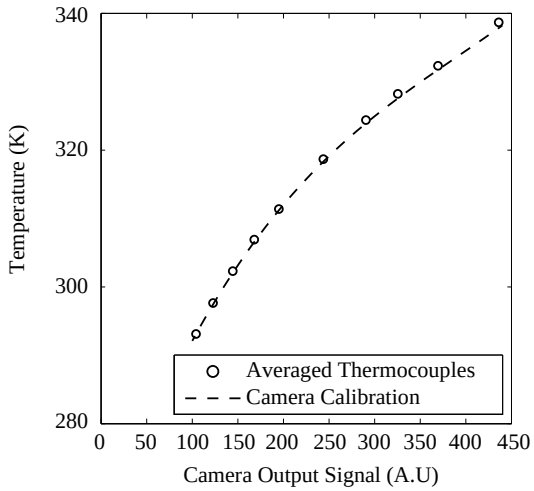

Figure 3.14: Calibration of the IR camera output signal.

was fitted to the data using Matlab. The camera calibration curve is detailed in Figure 3.14.

From a review of the literature, no acceptable correlations for stagnation point or area-averaged Nusselt numbers for confined liquid slot jets in the range of Reynolds numbers for this investigation, were found. However, well established correlations exist for confined liquid axisymmetric jets in the turbulent flow regime, using similar experimental techniques to this study. Based on this, the experimental heat transfer test facility was validated against the closest available theory. A 4mm diameter axisymmetric nozzle, with fixed confinement (H/D) and orifice plate thickness (t/D) ratios of 1, was fixed in the test section. The nozzle was then tested over a Reynolds number range of 1,000 to 6,000, and compared to the established correlations for stagnation point Nusselt number (Nu_0) presented by Sun et. al [66], and Garimella and Rice [28]. The results of this validation exercise are presented in Figure 3.15, and the uncertainty bars plotted are based on a separate uncertainty analysis conducted on the heat transfer validation configuration. It can be seen that within the experimental uncertainty, the heat transfer facility is in good agreement with the literature. Factors which could contribute to the variance include the differences in the experimental configurations used in the literature, and their associated uncertainties. The resulting correlation for

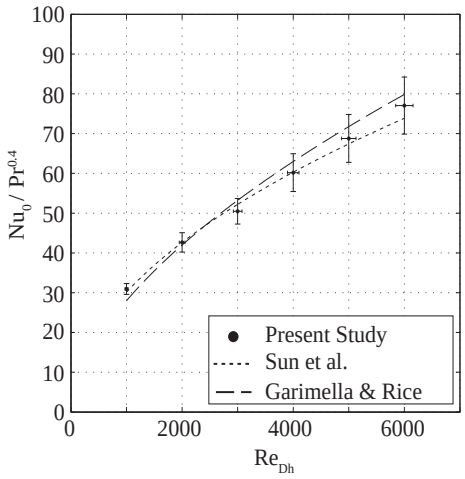

Figure 3.15: Validation of the heat transfer measurement facility against established correlations from the literature.

stagnation point Nusselt number, which had an R^2 value of 0.994, is given by eq. (3.11):

$$Nu_0/Pr^{0.4} = 0.764Re^{0.528} \tag{3.11}$$

The Reynolds number exponent of 0.528 was found to be consistent with the presence of a laminar boundary layer within the stagnation zone, and is in agreement with what was reported in the literature [28; 56; 83] – indicating the presence of potential core impingement.

3.4 Pressure Drop

3.4.1 Setup & Procedure

For the experimental pressure drop (ΔP) measurement facility detailed in Figure 3.16, a Cole-Parmer digital variable gear pump was used to draw water from a Lauda RE 104 water bath and pump it through a flow conditioning plenum and into the test section. Within the test section, the working fluid passed through the tested geometry before entering an outlet chamber and returning to the reservoir. The pressure drop was measured between two points. The first was located upstream of the jet nozzle geometry, and at least one flow development length

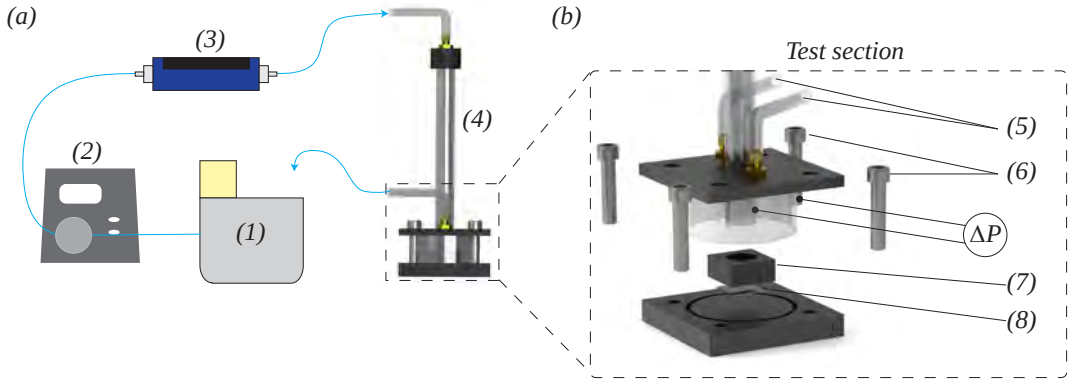

Figure 3.16: a) Schematic of the pressure drop measurement facility. (1) Lauda RE 104 water bath at 25°C, (2) Cole-Parmer digital gear pump, (3) Bronkhurst mass-flow meter, (4) flow conditioning plenum, and (b) detailed view of the test section (5) flow outlet to reservoir, (6) tightening screws, (7) test specimen holder, and (8) Stainless Steel test specimen.

from the plenum inlet ($L_{ld} = 0.06 Re_D D$ [123]). The second was at the outlet chamber wall, and detailed in Figure 3.16 (b). The pressure drops and mass flow rates were measured with an Omega PX2300-2DI transducer and a Bronkhurst Liqui-Flow mass flow meter, respectively. All measurements were recorded with a data acquisition card and logged with LabView.

3.4.2 Data Reduction

As the pressure drop rig was of a different length scale to that of the heat transfer rig, to allow for comparison of the two data sets, the pressure drop results were presented in the form of the non-dimensional head loss coefficient (K), given by eq. (3.12):

$$K = \frac{2\Delta P}{\rho U_{mean}^2} \tag{3.12}$$

The pressure differential (ΔP) was measured between the pressure ports detailed in Figure 3.16, and U_m was the mean jet exit velocity which was based on the baseline jet nozzle when examining the tab and chevron outlet modifications. As mentioned in Section 1.3, the required pumping power performance is a critical

performance parameter in the design of a microfluidic cooling solution, and was defined by eq. (3.13):

$$P_{Pump} = \dot{V}\Delta P \tag{3.13}$$

Where $\dot{V}$ was the volumetric flow rate. Once determined, the required pumping power would allow for any possible enhancements in heat transfer to be compared to their practical cost.

3.4.3 Rig Characterisation

In order to calibrate the transducer used, a pressure drop calibration facility was assembled, and detailed in Figure 3.17 (a). To begin the calibration, the valve (3) was opened to allow the two columns of water to reach equilibrium and the value for the zero reading was recorded. The valve was then closed, and a Festo EGSK-20-6P linear guide was used in conjunction with an EMMS-ST-42 stepper motor (2) to move one column of water (4) above the other (5), in increments of 1mmH_2O, or 9.81Pa. The electromechanical stage had rated resolutions of $\pm 10\mu m$, and $\pm 1.8° \pm 5\%$, respectively. For each increment in height, the voltages

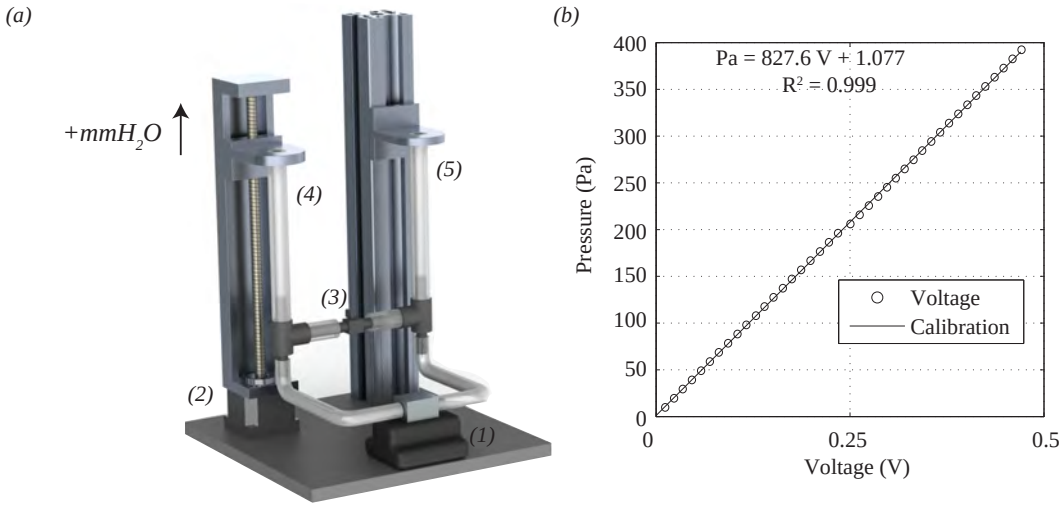

Figure 3.17: (a) Transducer calibration facility detailing the (1) Omega PX2300-2DI transducer (2) linear stage (3) valve (4) mobile head of water (5) static head, and (b) Pressure drop calibration results.

were recorded with a Native Instruments data acquisition card (NI-USB6009) and logged in LabVIEW – with 20,000 samples captured for each height to limit the impact of experimental noise. As can be seen in Figure 3.17 (b), the rig was calibrated between 0 to 392Pa and a polynomial calibration line was fitted using Matlab.

Similar to the velocimetry investigation, there are no appropriate correlations for the pressure drop through confined liquid slot jets in the laminar or turbulent regime. Therefore, the pressure drop facility was assessed against a numerical model, with the same boundary conditions, flow physics, and solver as for the PIV assessment in Section 3.2.4. Taking the jet nozzle aspect ratio of 4 as the assessment geometry, a three-dimensional model of the pressure drop facility was constructed within Star CCM+, and detailed in Figure 3.18 (a). The meshed numerical model is illustrated in Figure 3.18 (b), and a mesh sensitivity study was carried out to ensure the model achieved grid independence – with the results of this study detailed in Table 3.5.

Table 3.5: Mesh sensitivity analysis for assessment of the pressure drop measurement facility.

Mesh	No. of Cells	Difference in ΔP (%)
1	1.9 x 10^6	7.3%
2	2.3 x 10^6	3.11%
3	4 x 10^6	0.4%
4	5.9 x 10^6	0%

A steady state three-dimensional laminar simulation was performed using a segregated solver. Water at 25°C was used as the working fluid, and the properties were taken from Holman [71]. The model was run until acceptable convergence levels were achieved, and this is detailed in Figure 3.19. Within the numerical model, two point probes were established to measure pressure scalar values, and their locations corresponded to those of the pressure probes within the experimental facility. The numerical model was then run for the range of Reynolds numbers investigated, and the results of this assessment are detailed in Figure 3.20. The difference between the experimental and numerical results range between 2% –

6.8%, which is within the experimental uncertainty in pressure drop measurement (See Section 3.5.5). Consequently, the experimental measurement facility was found to provide valid data.

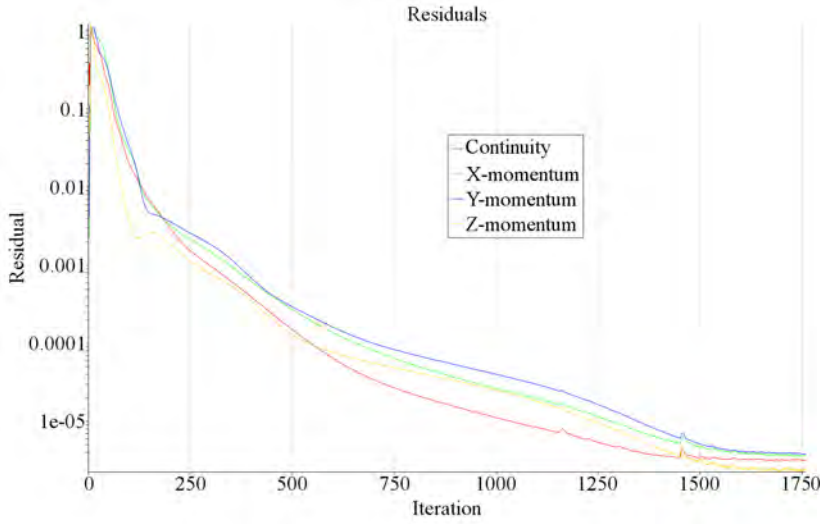

Figure 3.19: Convergence levels of the numerical simulation within Star CCM+, with respect to the number of iterations, for the pressure drop facility.

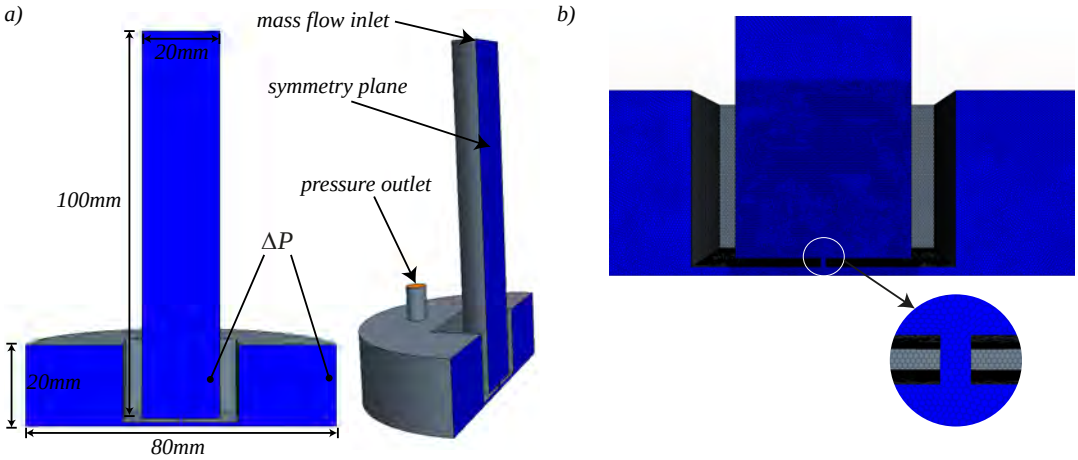

Figure 3.18: a) Geometry of the pressure drop measurement facility modeled within Star CCM+ and b) Meshing criteria applied to the numerical model.

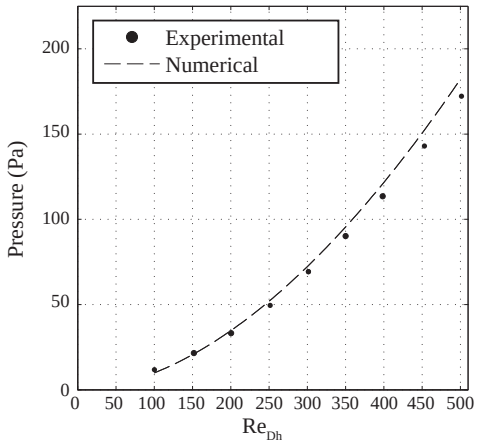

Figure 3.20: Assessment of the experimental pressure drop facility against the numerical simulation.

3.5 Uncertainty Analysis

An uncertainty analysis was carried out on all primary measurands to determine how these would influence the derived variables reported in the results. The procedure for evaluating these uncertainties, as well as the associated results, are presented in this section.

3.5.1 Experimental Uncertainties

For a derived experimental variable, R, which is a given function of independent primary measurands, as in eq. (3.14):

$$R = R(x_1, x_2, x_3, \cdots, x_n) \tag{3.14}$$

Once the uncertainties in the individual primary measurands have been defined, Kline and McClintock [124] presented a method of estimating the uncertainty in the derived experimental variable, ω_R, given by eq. (3.15):

$$\omega_R = \left[\sum_{i=1}^{n} \left(\frac{\delta R}{\delta x_i} w_i \right)^2 \right]^{1/2} \tag{3.15}$$

In many cases the function in eq. (3.14) can take the form of a product or additive function, seen in eqs. (3.16) and (3.17), respectively:

$$R = x_1^{a_1}, x_2^{a_2}, x_3^{a_3}, \cdots, x_n^{a_n} \tag{3.16}$$

$$R = a_1 x_1 + a_2 x_2 + a_n x_n = \sum a_i x_i \tag{3.17}$$

Where this is the case, Holman [125] expanded on this work, to present the uncertainty in the derived variables for product and additive functions as eqs. (3.18) and (3.19), respectively:

$$\omega_R = R\left[\sum_{i=1}^{n}\left(\frac{a_i \omega_{x_i}}{x_i}\right)\right]^{1/2} \tag{3.18}$$

$$\omega_R = \left[\sum_{i=1}^{n}\left(a_i \omega_{x_i}\right)^2\right]^{1/2} \tag{3.19}$$

The primary uncertainties in the experimental facilities used in this study are detailed in the following section, and will be used to determine the uncertainties in the derived functions present in the results.

3.5.2 Primary Uncertainties

The primary measurands for this study, and the reduction of their uncertainties, are as follows:

- ***Temperature***: For fluid temperature measurements, a Lauda RE 104 water bath was used in conjunction with a Fluke 1504 thermistor probe (See calibration certificate in Figure C.6) to calibrate the K-type thermocouples used. The thermocouples were calibrated over a range of 12 data points, from 20°C to 75°C. For each measurement, the system was given adequate time to ensure steady state conditions were achieved.

- ***Mass flow***: For the mass flow rates, two different pumps were used. A Cole-Parmer digital variable gear pump (model no. 07002-14) was used for the heat transfer and pressure drop analyses. The primary uncertainty

associated with this pump was deemed to be $\pm 5.56x10^{-6}$ kg/s. For the PIV measurement facility, a Totton DC40/10 centrifugal pump was used with a Cole-Parmer direct-reading flowtube, calibrated from 0 – 0.022 kg/s. This had an associated uncertainty of $\pm 7.89x10^{-5}$ kg/s.

- ***Length/Width/Height***: Where possible, all measurement lengths were verified using a Mitutoya digital calipers accurate to ±0.05 mm, and a Mitutoya micrometer accurate to ±0.01 mm. Uncertainties in internal dimensions – where these instruments were no longer feasible – were verified using an Axioskopp Zeiss microscope and a Hitachi TM-1000 SEM.

- ***Pressure***: Using the pressure calibration facility described in Section 3.4.3, the uncertainty in the pressure drop measurements was determined to be ±1.38 Pa, based on the accuracy of the linear stage and the large sample size reducing the influence of experimental noise.

The following subsections present the propagation of these primary uncertainties into the derived variables for the velocimetry, heat transfer, and pressure drop results sections.

3.5.3 Uncertainties in Velocimetry

For a PIV system, the accuracy of a single velocity measurement is dependent on the uncertainties within the data capturing and processing software, as well as the measurement of mass flow rate. Uncertainties in other less significant parameters, such as laser sheet thickness, tracer particle seeding, etc., were reduced through diligent experimentation, and by adherence to the system guidelines. In the PIV data processing techniques, to determine the velocity of a single particle, the following primary variables are required: the distance travelled by the tracer particle (x_{px}), measured in pixels; the pixel length scale (L_{px}), to convert x_{px} to metres; and the time taken for the particle to cover the measured distance (δt). With the velocity u given as:

$$u = \frac{x_{px} L_{px}}{\Delta t} \tag{3.20}$$

The uncertainties x_{px}, L_{px}, and Δt, propagate into the uncertainty in a single measured velocity. By applying eq. (3.18), the uncertainties in a single velocity measurement can be estimated using eq. (3.21):

$$\frac{\omega_u}{u} = \left[\left(\frac{\omega_{x_{px}}}{x_{px}} \right)^2 + \left(\frac{\omega_{L_{px}}}{L_{px}} \right)^2 + \left(\frac{-\omega_{\Delta t}}{\Delta t} \right)^2 \right]^{1/2} \tag{3.21}$$

The uncertainties in x_{px}, L_{px}, and Δt, were determined as follows:

- $\boldsymbol{x_{px}}$: Where β and σ are the bias error and precision errors, respectively, Forliti *et al.* [126] defined the uncertainty of a single pixel displacement measurement in any direction for a 95% confidence level as:

$$\omega_{x_{px}} = [\beta^2 + (2\sigma)^2]^{1/2} \tag{3.22}$$

  For this study, based on the Gaussian sub-pixel matching algorithm used in the vector processing, the bias error and precision errors were both ±0.03 px [126]. This gives an uncertainty of ±1.85% in x_{px}.

- $\boldsymbol{L_{px}}$: For the spatial calibration of the PIV measurement facility, 10 mm was found to equal 142 pixels. The uncertainty in capturing a point within the image processing software was deemed to be ±1 pixel. From this, the uncertainty in L_{px} was found to be 70.42μm ±1.38%.

- $\boldsymbol{\Delta t}$: Uncertainties in the synchronizer timing ($<$ 0.5 x $10^{-6}s$) and laser beam jitter ($<$ 0.5 x $10^{-6}s$) were found to be negligible, due to the Δt values used ($\Delta t \sim 10^{-3}s$).

From eq. (3.21), the uncertainty in a single velocity measurement (u,v,w) measured within Insight 3G was calculated to be ±2.3%.

As the PIV data is presented in terms of time-averaged velocity flow fields ($\bar{U}$), the measurement sample size, or number of image pairs captured, will influence the magnitude of uncertainty in $\bar{U}$. Stafford *et al.* [110] presented a statistical analysis for time-averaged flow fields using PIV. They proposed a method of monitoring the convergence of flow field data by measuring the residual error (E_R) with increasing sample size. They defined the residual error as the relative

error of the time-averaged data using N experimental samples, compared to the maximum number of samples recorded. By applying their analysis, the residual error in time-averaged velocity for a given number of samples, over the studied region of interest, was determined using eq. (3.23), where $\bar{U}_{ref}$ was a statistical reference quantity taken to be the spatial average over the region of interest.

$$E_R(\bar{U}_N) = 100\frac{\bar{U}_N - \bar{U}_{N,max}}{\bar{U}_{ref}} \tag{3.23}$$

Equation (3.23) was then used to plot the residual error in $\bar{U}$, for an aspect ratio of 1 slot jet at a Reynolds number of 500, against sample size (N), as detailed in Figure 3.21. Figure 3.21 presents the local residual errors (E_R) in $\bar{U}$, against the 1,000 sample average for a selected number of samples. With increasing sample size, the convergence in the error is apparent, as errors decrease from 65% at N=10 to <1% for N=950. It is difficult to accurately determine the error at each sample size with such a large quantity of samples in each vector field, however, the distribution of the errors about the mean is quite narrow. Due to this, the convergence of the relative error over the 1,000 samples for a 95% confidence level, is presented in Figure 3.22. The overall uncertainties in the velocimetry results are then detailed in Table 3.6.

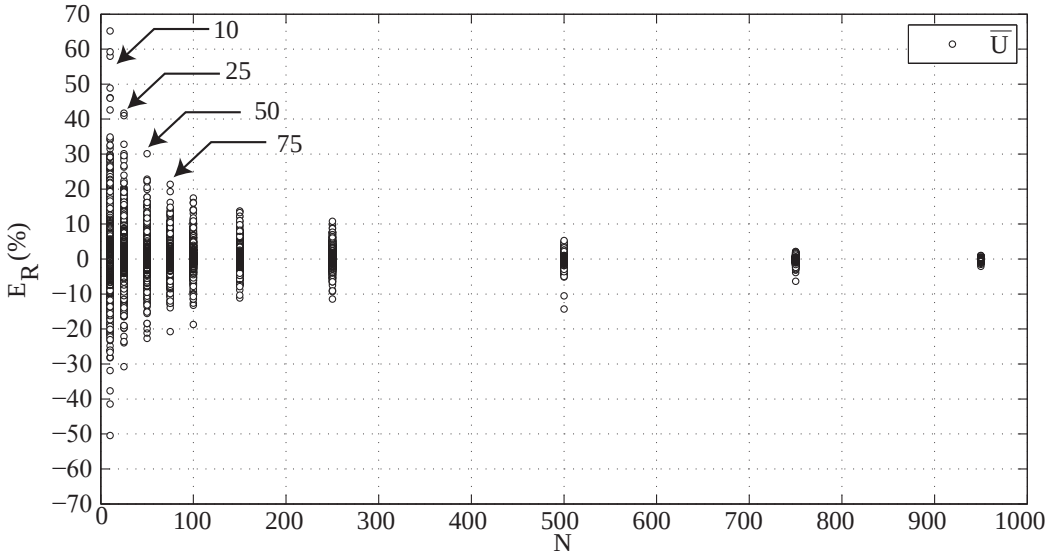

Figure 3.21: Local residual errors in $\bar{U}$ against the sample size (N), for an aspect ratio of 1 slot jet at a Reynolds number of 500.

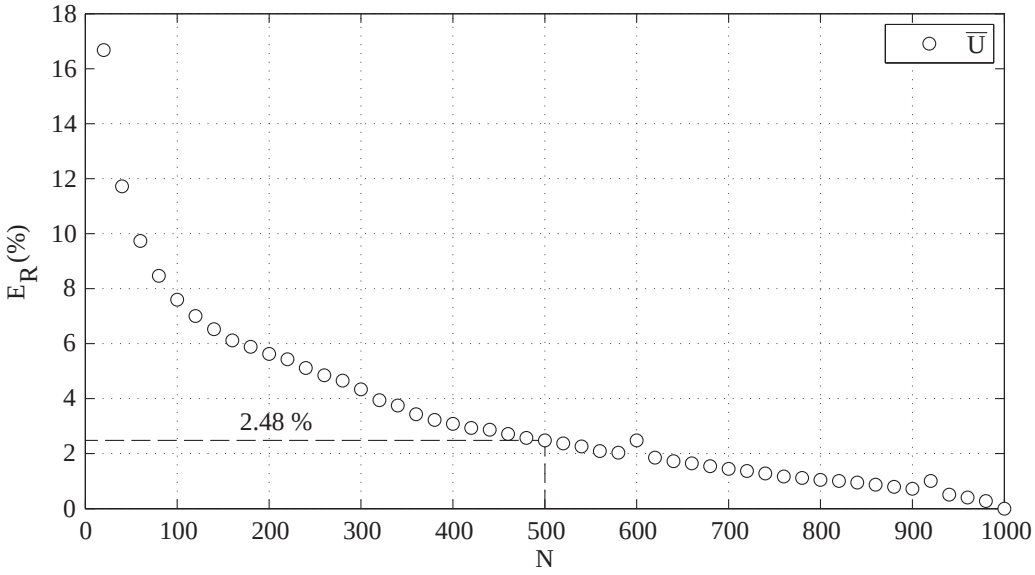

Figure 3.22: Convergence of residual error in $\bar{U}$ for a 95% confidence level as functions of sample size (N), for an aspect ratio of 1 slot jet at a Reynolds number of 500.

Table 3.6: Uncertainties in the velocimetry experiment.

Variable	Uncertainty
D_h	±1%
H	±0.5%
Area	± 0.7 – 0.8%
Re_{Dh}	±2.3 – 11.2%
u,v,w	±2.3%
U	±3.54 – 9.4%
$\bar{U}$	±2.48%

3.5.4 Uncertainties in Heat Transfer

The uncertainties in the derived variables for the Joule-heated foil measurement facility described in Section 3.3, are given in Table 3.7. The uncertainties in temperature difference (ΔT) along the foil were determined to be ±0.14°C, based

on the thermocouple and IR camera calibration. Uncertainties in power input to the foil to measure heat flux were dependent on the uncertainties in voltage (V) and current (I) measurements. These were recorded with a Fluke 45 multimeter and a Tenma 72-6185 clamp meter (calibration certificates located in Figures C.1 to C.4), with the uncertainties defined as ±0.05V and ±0.05A, respectively.

Table 3.7: Uncertainties in the Joule-heated foil experiment.

Variable	Uncertainty
ΔT	±1.42 – 5.12%
H	±1.25%
D_h	±2.5%
Area	±1.76 – 2.2%
$\dot{q}_{in}$	±1.48%
h	±1.47 – 5.38%
Re_{Dh}	±1.64 – 4.48%
Nu_{Dh}	±1.93 – 5.53%

3.5.5 Uncertainties in Head Loss

The uncertainties in the derived variables for the pressure drop measurement facility described in Section 3.4, are given in Table 3.8. Given the scale of the test pieces, uncertainties in the internal geometries – used in calculating D_h and Area – were based on the use of the microscopes to verify length and width. Given

Table 3.8: Uncertainties in the head loss experiment.

Variable	Uncertainty
D_h	±2%
H	±1%
Area	±1.4 – 1.8%
ΔP	±0.77 – 12.1%
K	±1.51 – 12.33%
Re_{Dh}	±1.65 – 7.97%

the resolution of the electromechanical stage used in the transducer calibration facility, the uncertainty in pressure measurement was deemed to be ±0.981 Pa, resulting in an uncertainty in ΔP of ±1.38 Pa.

3.6 Closure

This chapter details the test specimens investigated, as well as the design, setup, and data reduction utilised, in order to obtain full thermal and hydrodynamic characterisation of the specimens. Where possible, the experimental facilities were validated against established correlations from the literature. However, where these were not available, the facilities were assessed against numerical models to ensure that they were recording valid data. All uncertainties in the primary measurands were identified and, through the application of an uncertainty analysis, the propagation of these uncertainties into the derived secondary variables were identified, prior to obtaining the results. The results of this thesis are divided into two separate chapters, with Chapter 4 detailing the influence of slot jet aspect ratio on the thermal and hydrodynamic behaviour of the impinging jets, and Chapter 5 investigates the effect of the tab and chevrons on the aspect ratio of four slot jet, making comparisons to the results in Chapeter 4.

Chapter 4

Results & Discussion: Part I – Aspect Ratio

The velocity flow fields, heat transfer and pressure drop measurements for all jet nozzle aspect ratios and flow rates investigated in this thesis are detailed in this chapter. The velocimetry results are presented as velocity magnitude contour plots with streamlines overlaid, as well as the jet exit and wall jet velocity profiles. Results for heat transfer and pressure drop measurements are presented in non-dimensional terms – allowing for development of correlations.

4.1 Velocimetry

In order to understand the fluidic mechanisms which dictate the temperature distributions along the impingement surface, local velocity flow fields were captured using PIV. As previous studies did not observe a significant difference in the velocity flow fields when varying jet nozzle aspect ratio [8; 55], the investigation of one square jet and one rectangular (aspect ratio of 4) was deemed sufficient for this study.

4.1.1 Jet nozzle aspect ratio of 1

For the slot jet with an aspect ratio of 1 and a Reynolds number of 500, Figure 4.1 displays instantaneous and time averaged velocity contour plots. For the instan-

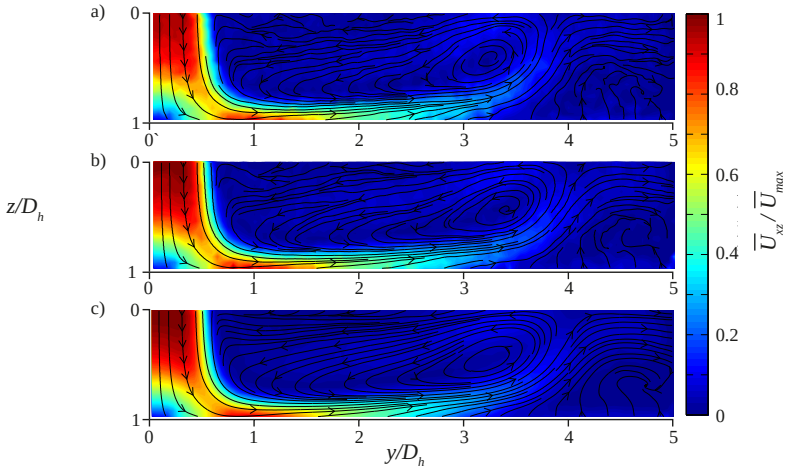

Figure 4.1: Instantaneous (a) and (b), and time averaged (c) velocity contour plots for the slot jet with an aspect ratio of 1 and a Reynolds number of 500.

taneous contour plots in (a) and (b), there is strong similarity visible with the time-averaged flow field in (c), which is indicative of predominantly steady flow. Therefore, the use of time-averaged contour plots will allow for the uncertainty in the statistical calculations of velocity magnitude to be minimised, and will not result in any unsteady flow features being lost. In the low velocity regions, such as in the ambient fluid surrounding the jet, the streamlines for the instantaneous plots can be seen to be coarse in comparison to the high velocity regions. This is a result of a disadvantage associated with the application of PIV, as the time step chosen was to capture the important high velocity jet regions, and would result in insufficient pixel displacements in the low velocity regions. Due to the large sample size associated with the time-averaged contour plot, these low velocity regions were seen to become much smoother.

Figure 4.2 displays the normalized velocity magnitude contour plots for a slot jet with an aspect ratio of 1, over the investigated Reynolds number range. The shear-driven interaction between the high velocity jet discharging from the nozzle and the surrounding ambient fluid – as well as the presence of the wall jet – resulted in local flow entrainment and formation of a recirculating vortex. This is denoted as the primary vortex. In line with what was reported in the literature [6; 7; 93], the primary vortex was seen to elongate and move downstream with

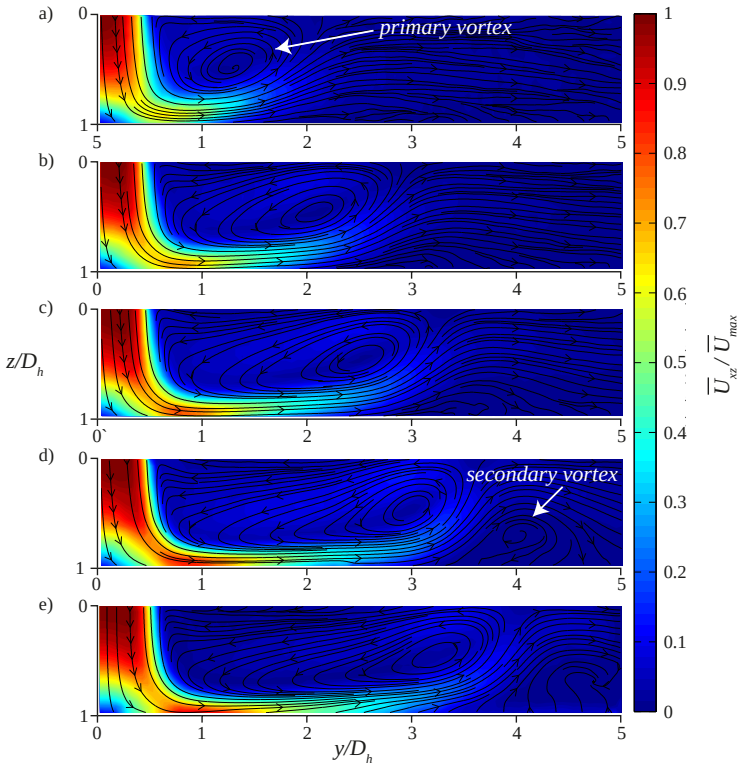

Figure 4.2: Normalized velocity magnitude contour plots and streamlines for an aspect ratio of 1 slot jet along $x/D_h = 0$, at a Reynolds number and $\bar{U}_{Max}$ of a) 100 & 13.1mm/s, b) 200 & 25.9mm/s, c) 300 & 34.5mm/s, d) 400 & 44.8mm/s, and e) 500 & 57.1mm/s.

increasing jet exit Reynolds number. Sivasamy *et al.* [6] concluded that the size of this primary vortex increased with increasing Reynolds number, and that the inverse is true for vortex strength. As the impinging jet approaches the target surface, the axial velocity components decelerate, and the jet began to spread radially outwards, resulting in the formation of a wall jet along the impingement surface. In the absence of the positive pressure gradient found within the stagnation zone, the hydrodynamic and thermal boundary layers between the wall jet and the impingement surface began to develop and thicken. This behaviour is typically associated with a monotonic decrease in Nusselt number [78], and will be discussed further in Section 4.2.1.

Due to the adverse pressure gradient caused by the expansion of the jet as it

progressed radially outwards, the wall jet reached a point where its momentum was unable to overcome the opposing frictional effects of the impingement surface and the flow retarding effects of the primary vortex [6]. This resulted in the wall jet detaching from the impingement surface within the investigated region for all tested Reynolds numbers. The location of the wall jet detachment was determined to be sensitive to jet exit Reynolds number, and this was in good agreement with what was reported in the literature [6; 7; 28]. By observing the velocity streamlines, it is evident that for $Re_{Dh} \leq 300$, the wall jet had reattached to the impingement surface within the investigated region. For $Re_{Dh} \geq 400$, a secondary recirculating vortex, such as that described by Sivasamy *et al.* [6] and Lee and Lee [7], was observed – and the onset of wall jet reattachment was evident downstream of the secondary vortex. Figure 4.3 displays the radial velocity profiles (v) along the impingement surface for a slot jet with an aspect ratio of 1 and a jet exit Reynolds number of 200. It is important to note that, by its nature, PIV is limited in resolving near wall measurements and, at $z/D_h = 0$, the velocity values were not presented. Consequently, as the boundary layer fluid dynamics is not critical within this investigation, this was deemed acceptable. Between $1 \leq y/D_h \leq 2$, the development of the wall jet as it progressed radially outward was evident.

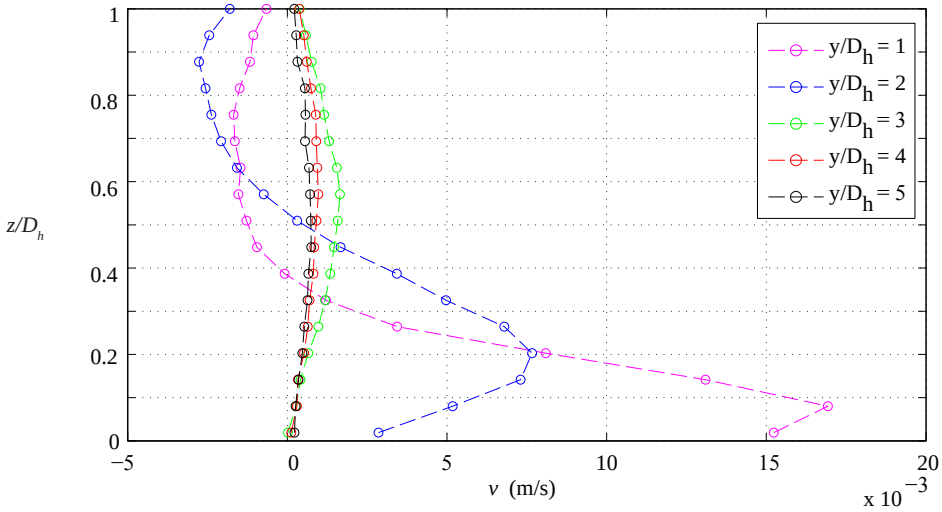

Figure 4.3: Radial velocity profiles for the slot jet with an aspect ratio of 1 at a Reynolds number of 200. As seen in Figure 4.1 (b).

The negative velocity values were as a result of the entrainment of ambient fluid radially inwards towards the impinging jet, and the associated formation of the primary vortex. The wall jet appeared to have detached from the impingement surface prior to $y/D_h = 3$ and, for $y/D_h \geq 4$, the wall jet had reattached to the impingement surface, and the shape of the velocity profiles were indicative of hydrodynamically developing flow between two flat plates [127]. This was in good agreement with the radial velocity flow profiles observed by Sivasamy *et al.* [6], due to the progression towards fully developed flow beyond the point of wall jet reattachment. The characteristics of developing, and fully developed flow, will be studied further in Section 4.2.1, when examining the distribution of local heat transfer coefficient along the impingement surface.

4.1.2 Jet nozzle aspect ratio of 4

Figure 4.4 displays the normalized velocity magnitude contour plots for the aspect ratio of 4 jet, along the minor (x/D_h) and major (y/D_h) axes. Along both axes, the interaction of the discharging jet with the surrounding ambient fluid resulted in flow entrainment radially inwards towards the impinging jet, and the formation of a recirculating vortex. As with the slot jet with an aspect ratio of 1, the vortex is seen to elongate and progress further downstream with increasing jet exit Reynolds number. The recirculating vortex is considerably larger along the major axis, and located in close proximity to the jet exit. Utilizing the lateral and spanwise PIV configuration, Figure 4.5 a) to c) displays the normalized velocity magnitudes and streamlines along the jet development region between $0.1 < z/D_h < 0.3$, for a slot jet with an aspect ratio of 4 and a Reynolds number of 500. It is evident from the velocity magnitude and streamlines that the entrainment of the surrounding fluid was predominant along the major axis, contributing to the larger recirculating vortex.

Along the minor axis, the velocity profiles appeared quite uniform within the impinging jet, and the wall jet which formed along the target surface develops up to and beyond the investigated region of $5D_h$, for all Reynolds numbers. However, along the major axis in Figure 4.4, off-center peaks are evident in the velocity profile of the impinging jet. When examining the hydrodynamic behaviour of

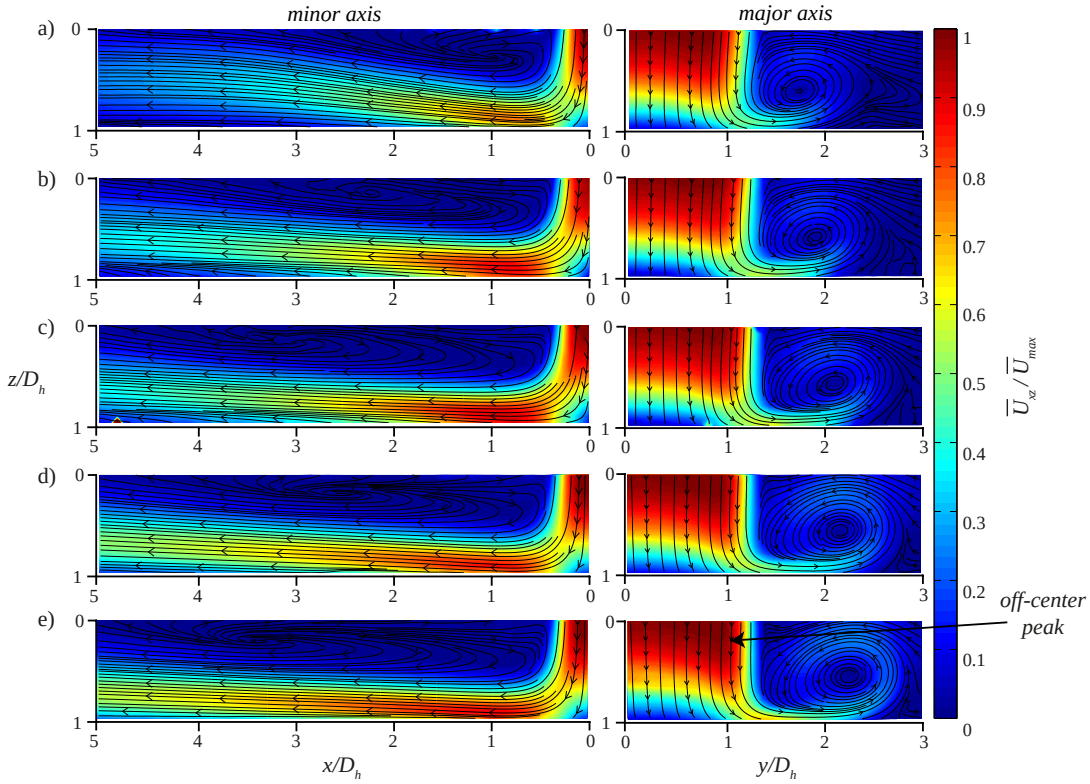

Figure 4.4: Normalized velocity magnitude contour plots and streamlines for an aspect ration of 4 slot jet, along the major and minor axes, at a Reynolds number and $\bar{U}_{Max}$ of a) 100, 13.6mm/s b) 200, 24.36mm/s c) 300, 35.3mm/s d) 400, 45.0mm/s and e) 500, 56.8mm/s.

slot jets, Lee and Lee [55] and Ashforth-Frost and Jumbanathan [37] observed the presence of similar peaks in the velocity profile along the major axis. They attributed these peaks to the flow contraction effects or, *vena contracta*, caused by the use of a thin orifice plate – with plate thickness to diameter ratios (t/D) of 0.2 and 0.15, respectively – upstream of a flow conditioning plenum. Lee and Lee [55] expanded further upon this, by confirming the relationship between the off-center peaks in the jet exit velocity profile and associated peaks in Nusselt number along the impingement surface. Based on these studies, the jet exit velocity profile along the major axis of the aspect ratio of 4 slot jet and a $Re_{Dh} = 500$, was plotted in Figure 4.6. Unlike the previously mentioned studies, the exit velocity profile was mostly uniform, and without any off-center peaks. Therefore, as with the findings

of Sezai and Mohamad [8], the observed off-center peaks were not attributable to upstream flow effects and, instead, must be caused by some downstream fluidic mechanism.

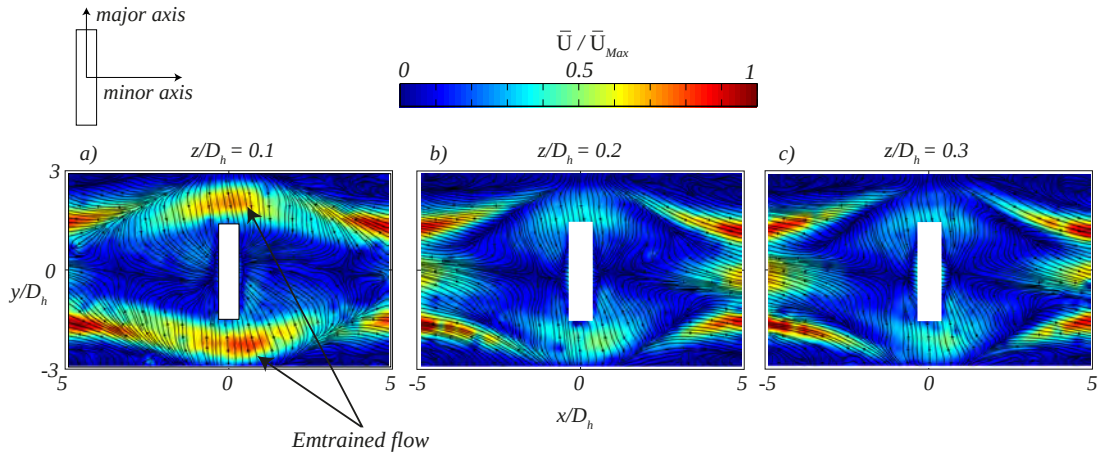

Figure 4.5: Lateral and spanwise velocity contour plots at z/D_h distances of b) 0.1, c) 0.2, and d) 0.3, for a slot jet with an aspect ratio of 4 and a Reynolds number of 500.

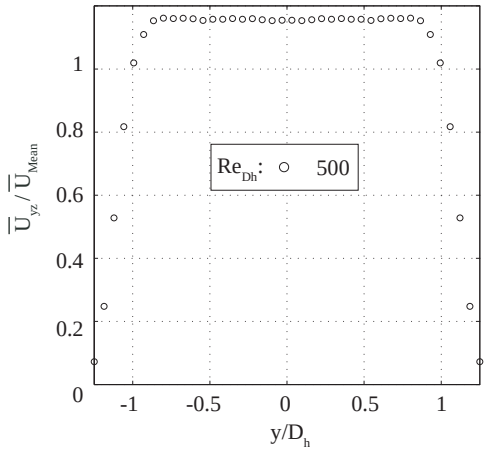

Figure 4.6: Jet exit velocity profile along the major axis at $z/D_h = 0.0625$, for the slot jet with an aspect ratio of 4 and at a Reynolds number of 500, normalized against the mean jet exit velocity.

When investigating the stagnation zone fluid dynamics of a submerged and confined axisymmetric water jet, Jeffers *et al.* [128] found that, in the presence of potential core impingement, the positive pressure gradient imposed along the impingement surface would result in a corresponding backpressure effect. They determined that this backpressure phenomenon would result in increased axial deceleration of the impinging jet – significantly influencing the centerline velocity profile of both laminar and turbulent impinging jets. It is postulated that, along the major axis of the slot jet, this backpressure effect would be prevalent within the stagnation zone, and would retard the velocity along the center of the impinging jet. This would lead to a deceleration in axial velocity along the center of the jet and, consequently, the appearance of off-center peaks in the jet velocity profile. The backpressure effect, coupled with the entrainment of the ambient surrounding fluid radially inwards towards the jet, would result in an enhancement in the mass flow of the impinging jet towards the edge of the major axis and, thus, an increase in thermal energy removal from the target surface. For all jet exit Reynolds numbers investigated, the wall jet along the major axis detaches from the impingement surface within the studied region of $3D_h$ – resulting in a significantly shorter wall jet when compared to the minor axis. This shortened wall jet is postulated to be due to the radial expansion of the jet as it progressed outwards, as well as the flow retarding influence of the larger recirculating vortex.

Figure 4.7 displays the radial velocity profiles (v) along the impingement surface, for a slot jet with an aspect ratio of 4 and a Reynolds number of 500. As previously mentioned, the strong negative velocities were associated with the entrainment of the ambient flow radially inwards and, consequently, the presence of the recirculating vortex. By examining the radial velocity profiles, the point of wall jet detachment is seen to occur between $2.5 < y/D_h < 3$ – resulting in the significantly shorter wall jet when compared to the minor axis; which is postulated to be due to the expansion of the jet as it progressed radially outwards, as well as the flow retarding influence of the larger primary recirculating vortex.

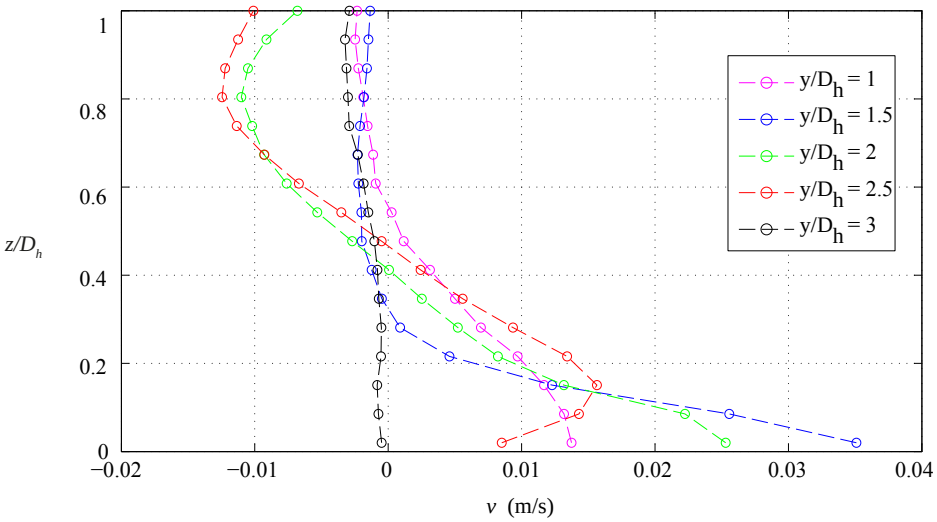

Figure 4.7: Radial velocity profiles for the slot jet with an aspect ratio of 4 at a Reynolds number of 500, along the major axis. As seen in Figure 4.3 (e).

4.2 Heat Transfer

Figures 4.8 and 4.10 detail the local Nusselt number distributions for all geometries investigated. These will be discussed in the context of the fluidic mechanisms detailed in the velocimetry section. Overall, the heat transfer coefficient for the slot jet was influenced the jet exit velocity – with the Nusselt numbers increasing with Reynolds number.

4.2.1 Jet nozzle aspect ratio of 1

It has been reported that for slot jets with confinement ratios (H/D_h) of less than 4 – such as in this investigation – the potential core of the jet impinges upon the target surface [41; 129]. This results in what is defined as potential core impingement, and has been found to induce a strong pressure gradient within the stagnation zone. This pressure gradient suppresses the growth of the boundary layer, resulting in a thermal boundary layer of near constant thickness [46]. As the velocity distribution within the potential core is uniform, and equal to that of the jet exit, the Nusselt number distribution can be seen to be reflective of the jet exit velocity profile in the presence of potential core impingement. By

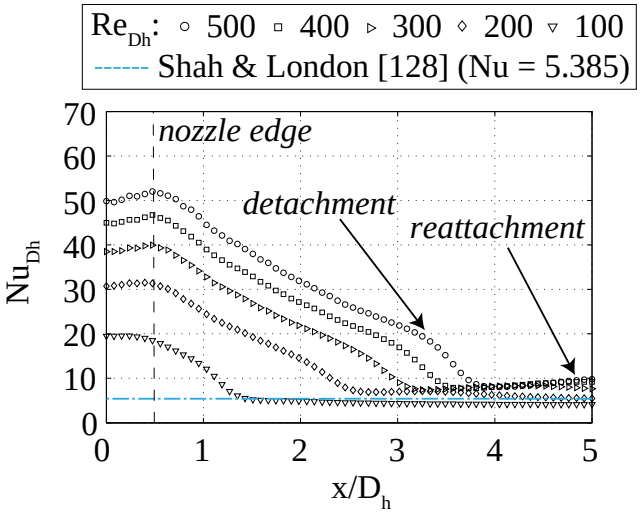

Figure 4.8: Local Nusselt number distributions for a slot jet with an aspect ratio of 1.

examining Figure 4.8 it was seen that, for all Reynolds numbers investigated, the Nusselt number distributions had an invariant profile within the stagnation zone, reflective of the jet exit velocity profile and, hence, indicative that the potential core was striking the impingement surface [28]. The appearance of any off-center peaks were found to be within the experimental uncertainty in Nusselt number.

Moving radially outwards beyond the stagnation zone, the local Nusselt number is seen to decrease. This thermal behaviour is indicative of the formation of a wall jet along the impingement surface [78] – as was seen in Figure 4.2 – and the associated thickening of the thermal boundary layer between the wall jet and the impingement surface. Interesting to note, however, is the presence of inflection points in the local Nusselt number distributions. These features were similar to those found by Sahoo and Sharif [93] and Lee *et al.* [7] and, as with both studies, their location and magnitudes were sensitive to jet exit Reynolds number. In line with what was found in both these studies, and the velocimetry data presented in Figures 4.2 and 4.3, it is evident that these inflection points were a result of the flow detachment from the impingement surface, and reattachment downstream. As was denoted in Figure 4.8, the point of wall jet detachment was associated with a sharp decrease in Nusselt number, and the observed local maximum in

Nusselt number, evident between $4.5 < x/D_h < 5$ for $Re_{Dh} \geq 300$, corresponded to the wall jet reattachment in Figure 4.2.

In the previously mentioned work of Sivasamy *et al.* [6], it was noted that once the wall jet reattached to the impingement surface, it progressed towards a fully developed flow profile downstream. For fully developed laminar flow between two flat plates, with a constant heat flux boundary condition applied to one surface, Shah and London [130] determined the Nusselt number to be 5.385, and this is represented by the blue line in Figure 4.8. The correlation provided by Shah and London [130] was based on two-dimensional flow between flat plates, and it is believed that along the captured PIV planes the flow is two-dimensional at the point of reattachement. Based on this, it appeared that for $Re_{Dh} \leq 200$, the wall jet reattached to the impingement surface and achieves a fully thermally developed profile within the investigated region. For $Re_{Dh} = 300$, the wall jet reattached to the impingement surface but is still developing and, for $Re_{Dh} \geq 400$, the wall jet has begun to reattach between $4.5 < x/D_h \leq 5$. This thermal behaviour is in very good agreement with the local velocity flow fields detailed in Figure 4.2.

Figure 4.9 details the fluidic mechanisms present for the slot jet with an aspect ratio of 1 at a Reynolds number of 200 – and how these influence the distribution of local Nusselt number along the impingement surface. Within the stagnation zone, the Nusselt number has an initially flat profile due to the uniform jet exit velocity profile and the presence of potential core impingement. Outside of the stagnation zone, a wall jet begins to develop. This results in a decrease in Nusselt number moving radially outwards, as both the thermal and hydrodynamic boundary layers begin to develop simultaneously. Detachment of the wall jet from the impingement surface, and the subsequent reattachment downstream, results in the observed inflection points in local Nusselt number. The location and magnitude of these inflection points are found to be sensitive to jet exit Reynolds number. Beyond reattachment, the flow then begins to develop until it achieves a fully thermally developed flow profile, and converges towards the Nusselt number value established by Shah and London [130].

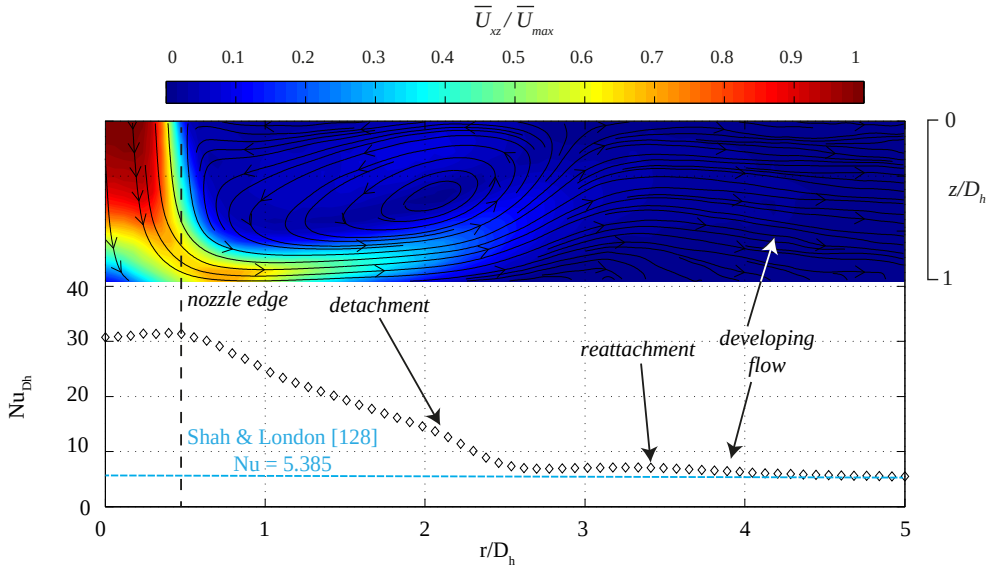

Figure 4.9: Illustration of the fluidic mechanisms present for an aspect ratio of 1 slot jet at $Re_{Dh} = 200$, as well as their associated influence on the local Nusselt number distribution.

4.2.2 Jet nozzle aspect ratios of 2 to 8

Figure 4.10 presents the local Nusselt number distributions along both axes, for slot jets with aspect ratios of 2 to 8. Along the minor axis, the local Nusselt number distribution is quite similar to the slot jet with an aspect ratio of 1. Initially, the Nusselt number has an invariant profile within the stagnation zone, before then decreasing monotonically outwards as the wall jet developed. Based on the results presented by Shah and London [130], for $Re_{Dh} = 100$, all slot jet aspect ratios investigated achieve a fully thermally developed flow profile within $5D_h$. For higher Reynolds numbers, the wall jet is still developing up to and beyond the investigated region. Along the major axis, off-center peaks in Nusselt number are present within the stagnation zone, resulting in a saddle-back Nusselt number profile, as was discussed in Section 2.3. The location and magnitude of these peaks are found to be Reynolds number dependent, and are in good agreement with what was observed by Sezai and Mohamad [8] and Lee and Lee [56], when examining the Nusselt number behaviour of slot jets as a function of increasing aspect ratio. As previously mentioned, Lee and Lee [56] concluded

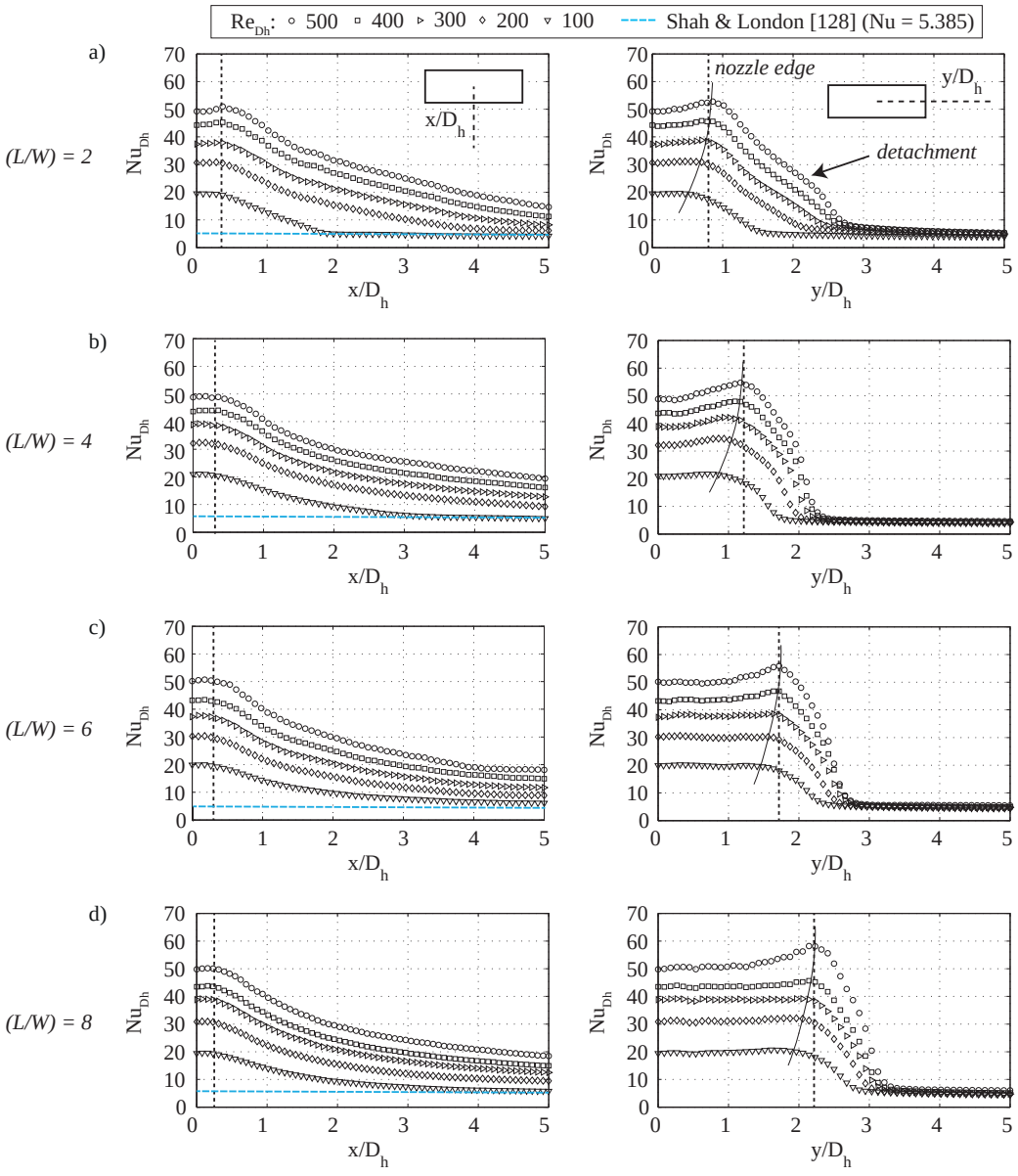

Figure 4.10: Local Nusselt number distributions along the x and y axes, for slot jets with aspect ratios of a) 2, b) 4, c) 6, and d) 8. The dashed lines inset represent the geometric edge of each nozzle.

that these peaks were a result of off-center peaks in the jet exit velocity profile. However, based on the uniform jet exit velocity profile in Figure 4.6, upstream flow conditions are not a factor in this study. Instead, it is postulated that these peaks in Nusselt number are due to the stagnation zone backpressure effect, coupled with the entrainment of the ambient surrounding fluid radially inwards towards the impinging jet. Thus, resulting in off-center peaks in the velocity profile of the impinging jet, corresponding to a local increase in heat transfer along the target surface. Beyond the stagnation zone, the Nusselt number decay is much steeper when compared to the minor axis. This is indicative of a diminished wall jet, with earlier detachment, and is in very good agreement with the velocimetry data previously detailed in Figure 4.7.

The appearance of saddle-back profiles have been observed when investigating the thermal and hydrodynamic behaviour of confined, laminar slot jets. Figure 4.11 presents a surface plot of Nusselt number along the impingement surface, with a slot jet aspect ratio of 4 and a Reynolds number of 500, for (a) this study and (b) the work presented by Sezai and Mohamad [8]. The presence of the saddle-back behaviour is evident in both images. Sezai and Mohamad [8] did not

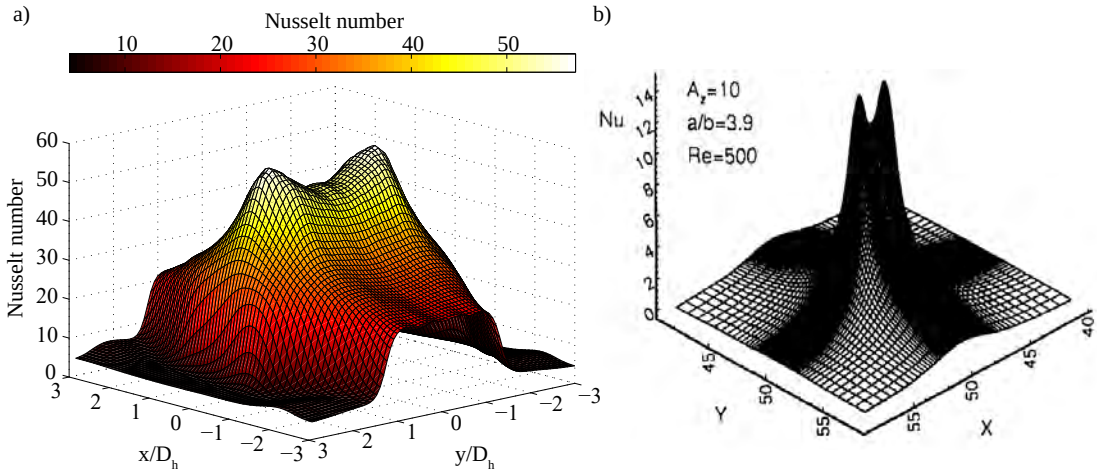

Figure 4.11: a) Surface plot of Nusselt number for $Re_{Dh} = 500$ and an aspect ratio of 4, to illustrate the recorded saddle-back behaviour, and b) the saddle-back behaviour recorded by Sezai and Mohamad [8].

present any definitive conclusions as to the cause of this behaviour but, with the application of a uniform exit velocity profile, they were able to determine that upstream flow conditions did not cause the saddle-back behaviour, in agreement with what was observed in this thesis.

For the range of Reynolds numbers investigated ($100 \leq Re_{Dh} \leq 500$), a product power-law relationship between stagnation point Nusselt number (Nu_0), Reynolds number (Re_{D_h}), and slot jet aspect ratio (L/W), taking the form: $Nu_0/Pr^{0.4} = aRe^b(L/W)^c$, is derived here. The resulting correlation has an R^2 value of 0.993, and is detailed in eq. (4.1):

$$Nu_0/Pr^{0.4} = 0.815Re^{0.55}(L/W)^{-0.004} \tag{4.1}$$

The Prandtl number exponent of 0.4 is based on that most widely used in the literature for water jets [28; 66]. In the presence of potential core impingement, the positive pressure gradient formed within the stagnation zone has been shown to suppress the growth of the boundary layer [46], and establish a laminar boundary layer of constant thickness within the stagnation zone [131; 132]. Based on previous studies on impinging jets, the presence of a laminar boundary layer was associated with a Reynolds number exponent of $\leq$0.59 [28; 56; 83] – and, therefore, the Reynolds number exponent of 0.55 found in this study is consistent with the presence of a laminar boundary layer within the stagnation zone, and potential core impingement. It is also determined from eq. (4.1) that the stagnation point Nusselt number had a very weak dependency on the aspect ratio of the slot jet.

By examining the area-averaged heat transfer results in Figure 4.12, over an area of $36D_h^2$ around the stagnation point, it was noted that increases in both Reynolds number and jet nozzle aspect ratio resulted in a corresponding increase in area-averaged Nusselt number (Nu_{Avg}). For the range of Reynolds numbers investigated, it is found that increasing the aspect ratio from 1 to 8 results in an increase in Nu_{Avg} of up to 68%. A surface fit was applied to the area-averaged Nusselt number results presented in Figure 4.12. A correlation extrapolated from the surface fit has a resultant R^2 value of 0.993, and is detailed in eq. (4.2):

$$Nu_{Avg}/Pr^{0.4} = 0.0747Re^{0.775}(L/W)^{0.182} \tag{4.2}$$

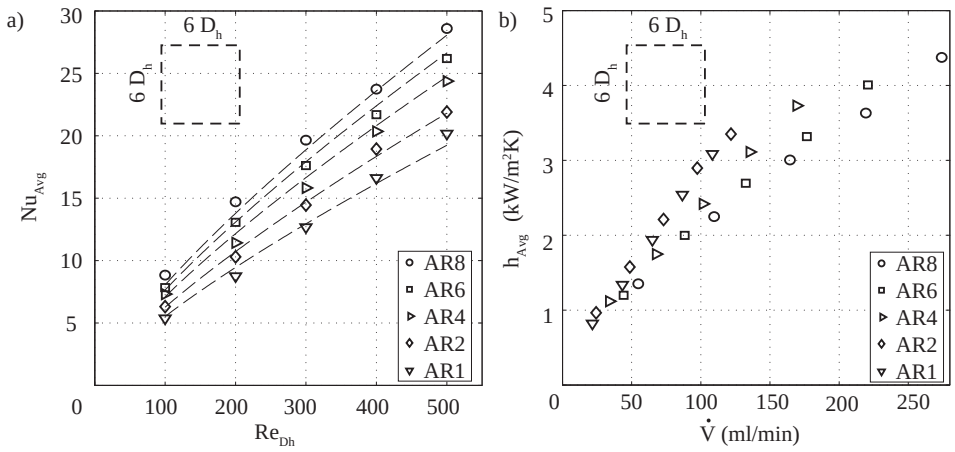

Figure 4.12: a) Area-averaged Nusselt number as a function of Reynolds number, and b) Area-averaged heat transfer coefficient as a function of volumetric flow rate.

Based on previous jet studies, a Reynolds number exponent of > 0.7 for Nu_{Avg} is typically indicative of predominantly turbulent flow along the impingement surface. However, the majority of research conducted into slot jets has been confined to high Reynolds number ranges, and there are no appropriate correlations reported for confined, submerged, laminar, liquid slot jets, which can be compared with eq. (4.2).

Combining the jet development planes captured through the application of the lateral and spanwise PIV configuration, with the streamwise PIV planes along both axes, and local Nusselt number distributions along the impingement surface, allowed for a full visualisation of the confined slot jet temperature and velocity flow fields – which is presented in Figure 4.13. The important fluidic structures associated with the confined liquid slot jet, and their corresponding influence on the temperature distributions along the impingement surface, can be seen in Figure 4.13. These include:

- The presence of the off-center peak in the velocity profile of the impinging jet, and the corresponding off-center peak in Nusselt number along the target surface.

- The formation and development of a wall jet along both axes, and the decrease in Nusselt number seen along the target surface – as well as the

earlier detachment of the wall jet along the major axis in comparison to the minor axis.

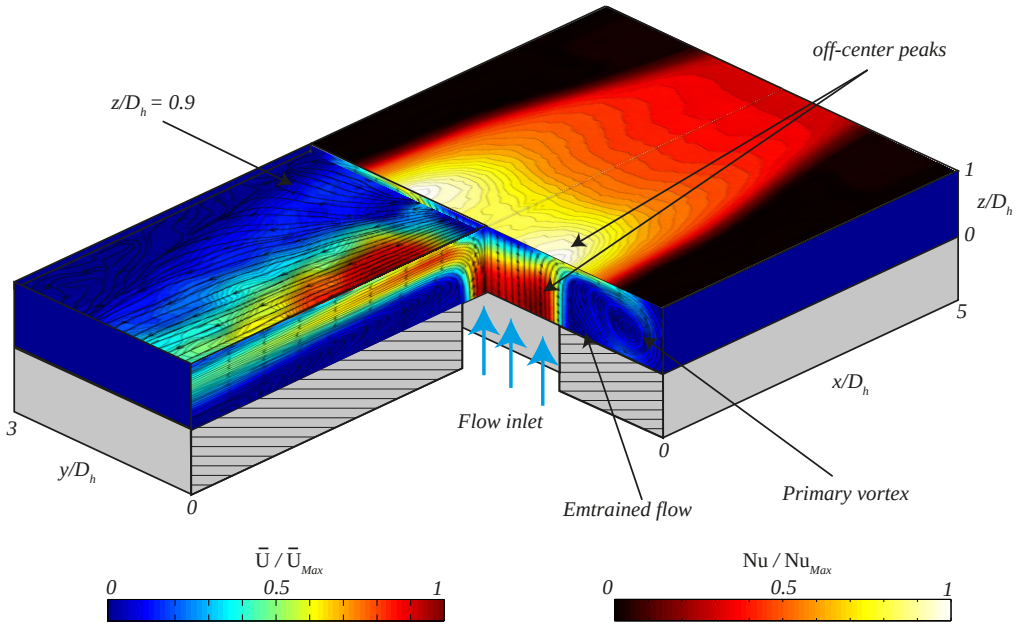

Figure 4.13: Combined local Nusselt number distributions and normalized velocity contour plots for an aspect ratio of 4 slot jet at a Reynolds number of 500.

4.3 Head Loss

In order to fully characterise the practical costs of any possible enhancements in slot jet heat transfer, a pressure drop (ΔP) analysis was carried out on all geometries and flow rates investigated. From the results of this analysis, presented in Figure 4.14, it is evident that the pressure drop across the nozzles is sensitive to nozzle aspect ratio, with a slight decrease in pressure drop found with increased nozzle aspect ratio – promoting the benefits of higher nozzle aspect ratios. Using eq. (3.12), the head loss coefficients (K) for each Reynolds number and aspect ratio were calculated and presented in Figure 4.15. From Poiseuilles law it has been stated that for laminar flow the pressure drop is directly proportional to velocity [127] and, therefore, $K \propto Re^{-1}$. For higher Reynolds numbers, as inertia

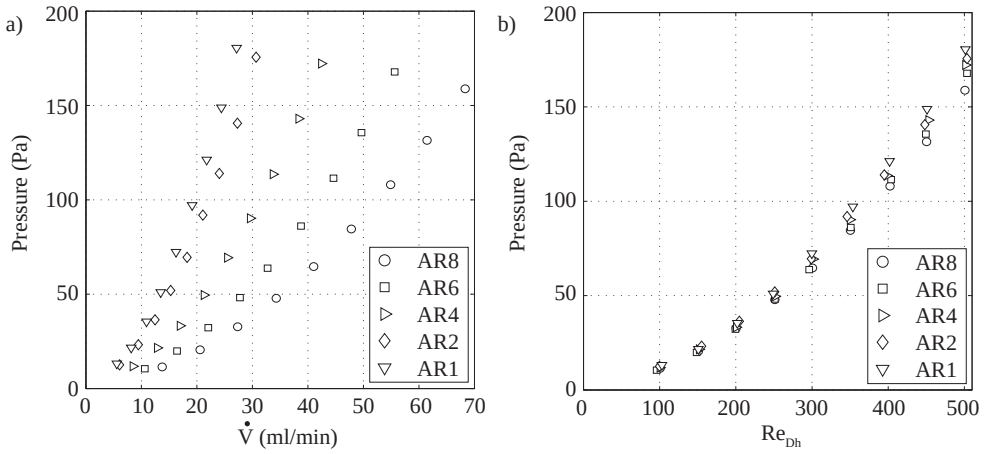

Figure 4.14: Pressure drop as a function of a) volumetric flow rate and b) Reynolds number.

forces begin to dominate and the flow transitions from laminar to turbulent, the pressure drop is proportional to the velocity squared, and K will then approach a constant value [133]. It can be seen from Figure 4.15, that as the Reynolds number increases the plot begins to asymptote towards a constant head loss coefficient. Suggesting that from $200 \leq Re_{Dh} \geq 500$, the flow regime through the nozzle is transitioning from laminar to turbulent. Similar to eq. (4.2), a product power-law relationship between K, Re_{Dh}, and aspect ratio (L/W) was developed.

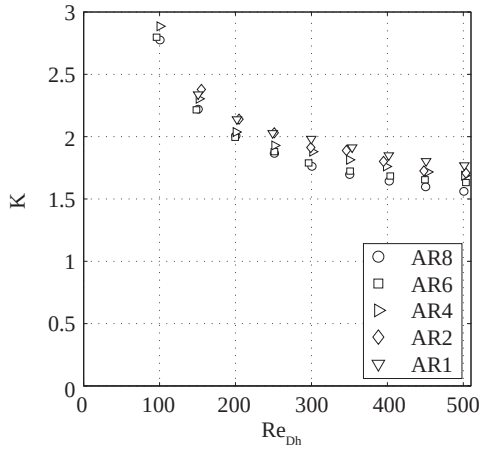

Figure 4.15: Head loss coefficient as a function of Reynolds number for all geometries investigated.

The correlation has a resultant R^2 value of 0.99 and is presented in eq. (4.3):

$$K = 10.74Re^{-0.29}(L/W)^{-0.052} \tag{4.3}$$

Once the head loss coefficients were known, it allowed for a new design variable, Nu_{Avg}/K, to be established. Nu_{Avg}/K was plotted as a function of Reynolds number and aspect ratio, and presented in Figure 4.16. From this, it was possible to determine the ratio of area-averaged heat transfer enhancement to the associated hydrodynamic loss, for each aspect ratio and flow rate. It is determined that for the range of Reynolds numbers investigated, increasing the aspect ratio from 1 to 8 results in decreases in K of up to 12%, and increases in Nu_{Avg}/K of 63.5%. A correlation between Nu_{Avg}/K, Re_{Dh} and aspect ratio (L/W), with an R^2 value of 0.994 was developed, and given by eq. (4.4):

$$Nu_{Avg}/K = 0.0078Re^{1.048}(L/W)^{0.236}Pr^{0.4} \tag{4.4}$$

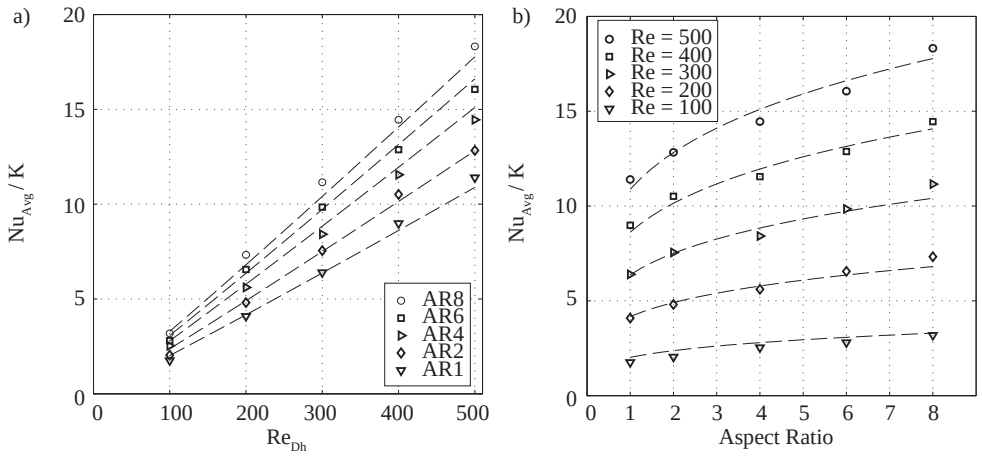

Figure 4.16: Ratio of area-averaged Nusselt number against head loss coefficient (K) as a function of a) Reynolds number and b) aspect ratio, for all geometries and flow rates investigated.

By combining the heat transfer results from Section 4.2 with the results of the pressure drop analysis, it is evident that increasing slot jet aspect ratio is an effective means of achieving passive enhancement for the thermal and hydrodynamic behaviour of confined and impinging slot jets.

4.4 Closure

In this chapter, the influence of jet nozzle aspect ratio on the thermal and hydrodynamic behaviour of confined, impinging liquid slot jets was experimentally investigated. The experiments were conducted over a Reynolds number range of 100 to 500, with a fixed confinement ratio (H/D_h) of 1. The results were presented in terms of local velocity flow fields, as well as Nusselt number and head loss coefficient as a function of the jet exit Reynolds number and aspect ratio.

Using PIV, the streamwise and jet development velocity profiles were captured. These allowed for the velocity profile of the impinging jet, and the interaction of the jet with the surrounding ambient fluid and the target surface, to be analyzed. For all geometries and flow rates investigated, the shear-driven interaction between the discharging jet and the ambient surrounding fluid was found to result in the entrainment of ambient fluid radially inwards towards the jet, and the formation of a recirculating vortex. This vortical structure was found to elongate and move downstream with increasing jet exit Reynolds number. For slot jets with aspect ratios of greater than 1, off-center peaks in velocity were observed along the major axis. These were found to be independent of the upstream flow conditions and were postulated to be as a result of the stagnation zone fluid dynamics – more specifically, the stagnation zone backpressure effect – and the entrained flow. Moving radially outwards beyond the stagnation zone, the formation and development of a wall jet along the impingement surface was observed for each geometry and flow rate, and the length of the wall jet was found to be dependent on the jet exit Reynolds number. For the slot jet with an aspect ratio of 1, detachment of the wall jet from the impingement surface, and reattachment further downstream, was observed within the studied region. This was found to be in good agreement with what was reported in the literature. Increasing the slot jet aspect ratio to 4, the wall jet demonstrated very different hydrodynamic behaviour, with a significantly longer wall jet along the minor axis when compared to the major axis of the jet.

The local heat transfer coefficients along the impingement surface were captured using the Joule-heated foil technique and presented in terms of Nusselt number as a function of jet exit Reynolds number – to allow for correlations

of the stagnation point and area-averaged Nusselt numbers to be extrapolated. Overall, the local Nusselt number distributions were found to correspond quite well with the velocimetry data. From the resulting correlations, it was found that the stagnation point Nusselt number (Nu_0) had a very weak dependency on the jet nozzle aspect ratio (L/W), but scaled with $Re_{Dh}^{0.55}$. This Reynolds number scaling was consistent with the presence of a laminar boundary layer within the stagnation zone and, therefore, in agreement with what was previously discussed in the literature. The area-averaged Nusselt number (Nu_{Avg}) was taken as the averaged Nusselt number over an area of $3D_h$ from the stagnation point outwards along both axes, and was found to have a stronger dependency on both jet exit Reynolds number ($Re_{Dh}^{0.775}$) and aspect ratio ($(L/W)^{0.182}$). Over the range of Reynolds numbers investigated, it was determined that increasing the aspect ratio of a confined laminar slot jet from 1 to 8 resulted in an increase in area-averaged heat transfer removal of up to 68%. For slot jets with aspect ratios greater than 1, off-center peaks were observed in the local Nusselt number distributions along the major axis, leading to the presence of saddle-back behaviour. The cause of these peaks was postulated to be a result of the off-center peaks in the velocity profile.

Measurements of the pressure drop through each slot jet geometry found that the head loss coefficient (K) was also sensitive to the jet exit Reynolds number and, to a lesser extent, the slot jet aspect ratio – with a surface plot fitted to the data determining that K= $f(Re_{Dh}^{-0.29}(L/W)^{-0.052})$. Increasing the aspect ratio of the slot jets from 1 to 8 was found to lead to a decrease in the head loss coefficient of up to 12%. Given the associated increase in area-averaged Nusselt number, it can be concluded that the higher aspect ratio nozzles are the preferred design for achieving practical heat transfer enhancements.

Chapter 5

Results & Discussion: Part II – Outlet Modifications

This chapter details the results of the passive control and enhancement of a confined impinging slot jet, through the use of tab and chevron outlet modifications. The influence of the outlet modifications was characterised both thermally and hydrodynamically, by capturing the local velocity flow fields, surface temperature distributions, and nozzle pressure drops – and comparing them to the baseline case. The results are presented in terms of the velocity flow fields produced by each geometry, as well as the local and area-averaged Nusselt numbers and head loss coefficients as a function of jet exit Reynolds number.

5.1 Velocimetry

To understand the influence of jet outlet structures on the hydrodynamic behaviour of the confined slot jets, 2D velocity flow fields were captured along the major and minor axes for each investigated geometry and flow rate. These are presented in the form of velocity contour plots with streamlines overlaid. The hydrodynamic behaviour of the baseline case (aspect ratio of 4 slot jet) was previously demonstrated in Figures 4.4, 4.6 and 4.7. The important fluidic mechanisms influencing surface heat transfer were identified as the stagnation zone fluid dynamics, flow entrainment, wall jet formation, and the length of the wall

jet before detachment. The influence of the outlet structures on these features will be investigated and compared to the baseline case in this section.

5.1.1 Modifications to the Minor Axis

Figures 5.1 to 5.3 detail the jet exit velocity profiles along the major axis, and the full field velocity contour plots for the minor double tab and minor triangle tab geometries, respectively. Along the minor axis, it is evident that both tab geometries are similar to the baseline case, with the jet expanding radially outwards and the formation of a wall jet along the target surface. For both geometries, the wall jet continued to develop up to and beyond the investigated region of $5D_h$. Along the major axis, off-center peaks in the velocity profile of the impinging jet are observed for both geometries. Figure 5.1 plots the jet exit velocity profiles along the major axis for the (a) minor double tab (b) and minor triangle tab geometries. The exit velocities have been normalized against the mean jet exit velocity ($\bar{U}_{Mean}$) for the $Re_{Dh} = 500$ configuration. Similar to the baseline jet, the exit velocity profiles are mostly uniform, with any semblances of off-center peaks found to be within the uncertainty present in velocity measurement. Consequently, it is evident that the cause of these off-center peaks could not be attributable to

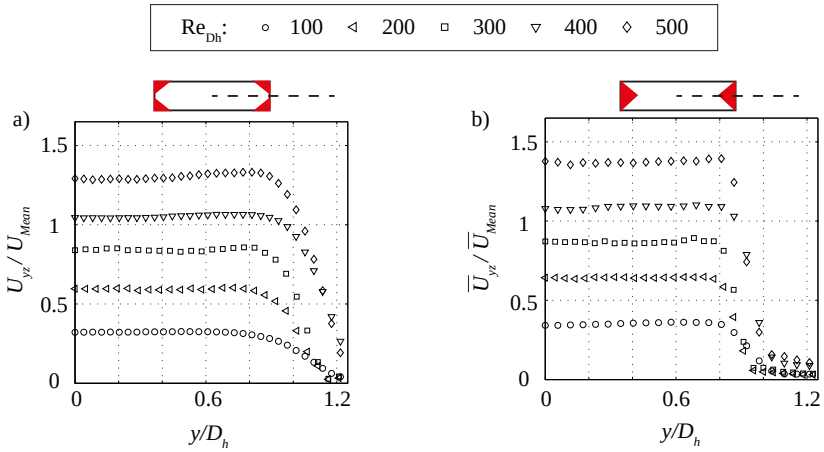

Figure 5.1: Jet exit velocity profiles normalised against the mean jet exit velocity $\bar{U}_{Mean}$ (based on the baseline case with an aspect ratio of 4) for the $Re_{Dh} = 500$ configuration, for the (a) Minor double tab (b) and Minor triangle geometries.

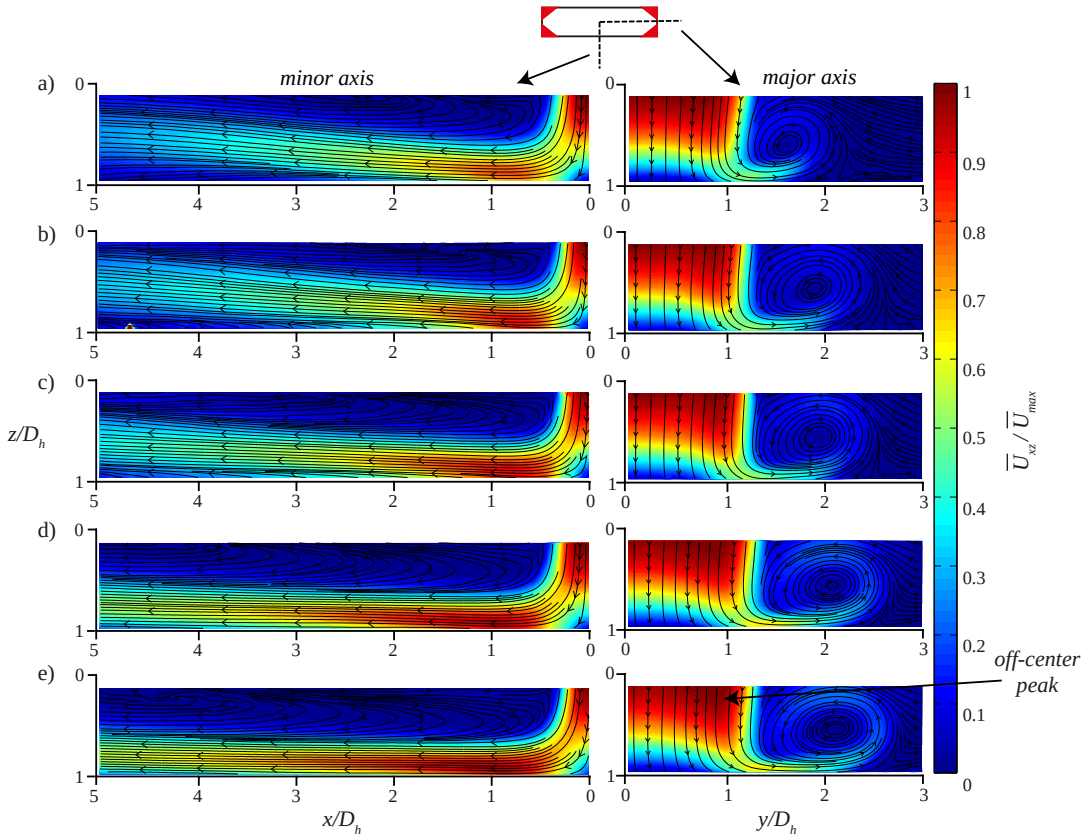

Figure 5.2: Normalised velocity magnitude contour plots and streamlines for the minor double tabs case, along the major and minor axes, at a Reynolds number and $\bar{U}_{Max}$ of a) 100, 14.7mm/s b) 200, 27.1mm/s c) 300, 38.6mm/s d) 400, 48mm/s and e) 500, 59.9mm/s.

upstream flow conditions, or the tab geometries. Instead, as with the off-center peaks along the major axis of the baseline jet, these are postulated to be a result of the stagnation zone backpressure effect, and the local flow entrainment along the major axis. Moving radially outwards beyond the impinging jet, the resulting velocity flow field behaviour is quite different, and the influence of the tab geometries is prevalent. The minor double tab geometry resulted in similar behaviour to the baseline case, as the flow entrainment due to the shear-driven interaction between the exiting jet and the ambient surrounding fluid resulted in the formation of a recirculating vortex. The vortex is then seen to grow and move further downstream with increasing jet exit Reynolds number. However,

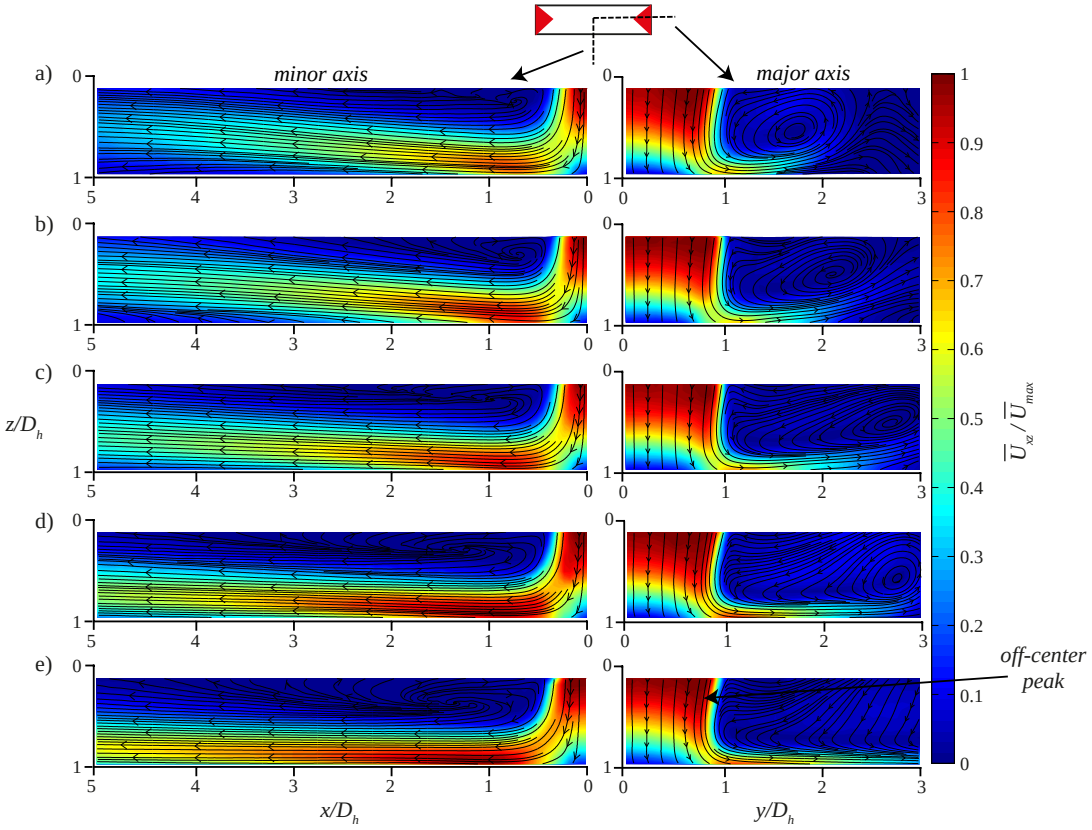

Figure 5.3: Normalised velocity magnitude contour plots and streamlines for the minor triangle tab, along the major and minor axes, at a Reynolds number and $\bar{U}_{Max}$ of a) 100, 16.3mm/s b) 200, 29.5mm/s c) 300, 40.2mm/s d) 400, 49.6mm/s and e) 500, 62.7mm/s.

the wall jet which formed along the major axis detaches from the impingement surface within $y/D_h = 2.5$, for all jet exit Reynolds numbers. This is postulated to be a result of the enhanced spanwise spreading caused by the tab geometry, and will be investigated further in Section 5.2. For the minor triangle geometry, the shape and location of the tabs resulted in a significant increase in the length of the wall jet and, for $Re_{Dh} \geq 400$, it appears to detach from the impingement surface beyond the studied region of $3D_h$.

5.1.2 Modifications to the Major Axis

Figures 5.4 to 5.7 detail the jet exit velocity profiles along the major axis, and the full field velocity contour plots for the major triangle, chevron and contour tab geometries, respectively. For the major triangle tab geometry, the shape of the tab results in a much different velocity distribution along the minor axis to all previous geometries. The entrainment of surrounding ambient fluid radially inwards towards the jet, as well as the presence of the wall jet, results in a recirculating vortex. Unlike the previous tab geometries, the vortex does not progress downstream with increasing Reynolds number, instead, it remains adjacent to the impinging jet. This is believed to be as a result of the tab geometry causing the wall jet to be deflected away from the impingement surface, which also results in the shortened wall jet observed. The geometry and location of the outlet tabs appears to cause the jet to bifurcate into two individual jets, located either side of the tabs, and this is evident in the jet exit velocity profiles plotted in Figure 5.4 (a). As the Reynolds number is increased to $Re_{Dh} \geq 300$, it is postulated that a region of enhanced mixing is created in the center of the stagnation zone (y/D_h = 0), where the bifurcated jets meet. This would lead to what is referred to as jet crossflow, a fluidic mechanism associated with the behaviour of neighbouring jets

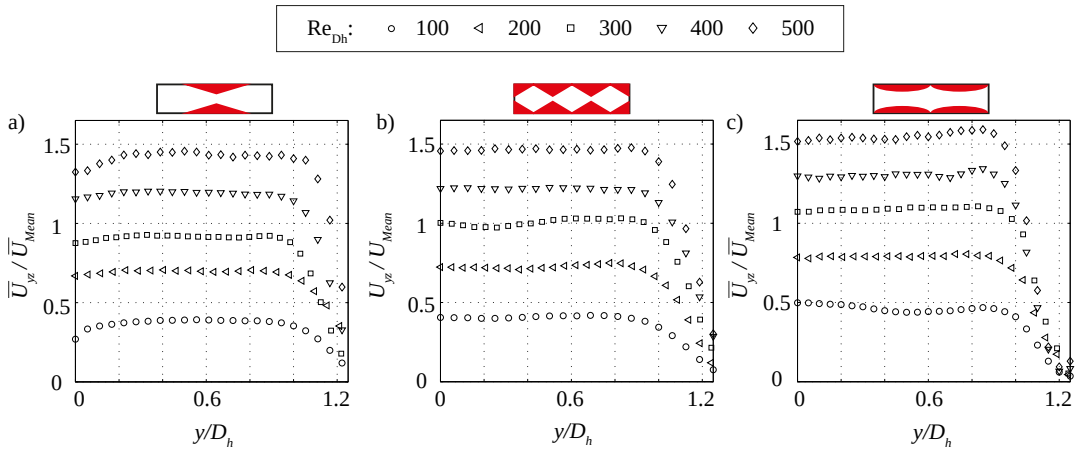

Figure 5.4: Jet exit velocity profiles normalised against $\bar{U}_{Mean}$ for the Re_{Dh} = 500 configuration, for the (a) Major triangle, (b) Chevron, and (c) Contour tab geometries.

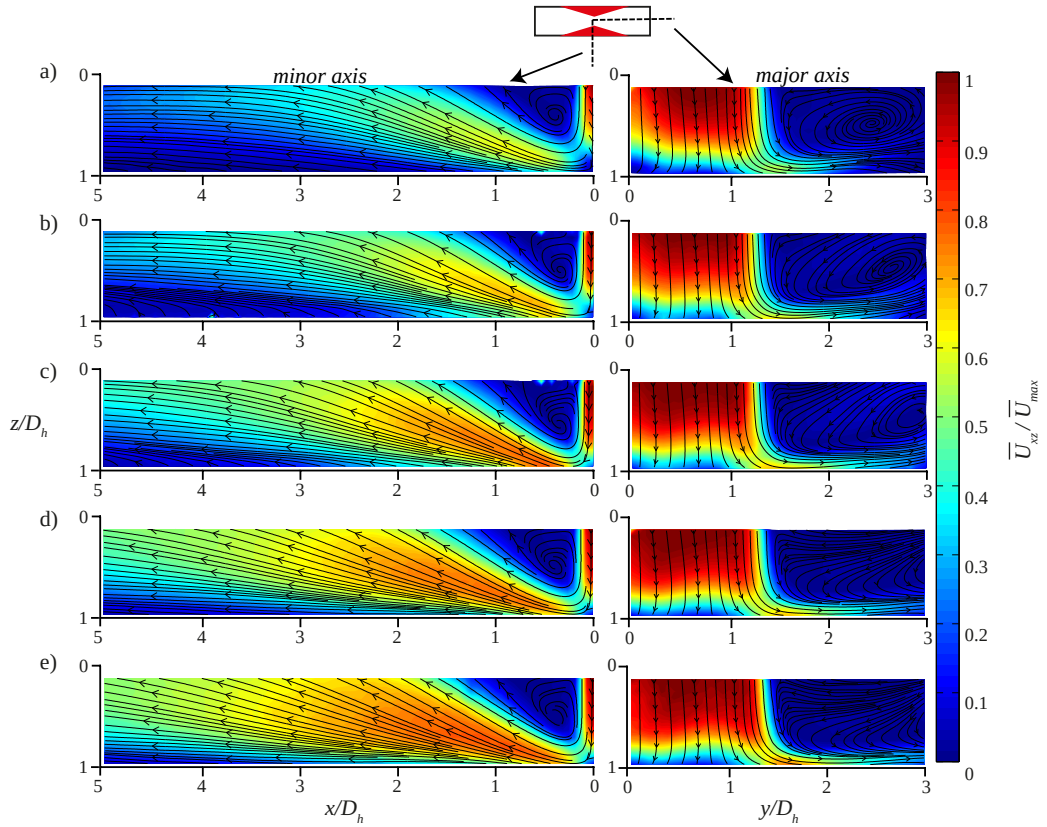

Figure 5.5: Normalised velocity magnitude contour plots and streamlines for the major triangle tab, along the major and minor axes, at a Reynolds number and $\bar{U}_{Max}$ of a) 100, 17.6mm/s b) 200, 32.6mm/s c) 300, 42.1mm/s d) 400, 54.2mm/s and e) 500, 65.8mm/s.

in an array [54; 134]. Crossflow can have a dominant effect on the thermal energy removal from the impingement surface, due to increased mixing and the formation of turbulent structures. However, it is dependent on many design variables, such as jet to jet spacing, the number of jets, and the removal of spent fluid [134; 135]. As with the minor triangle geometry, for $Re_{Dh} \geq 300$, the major triangle outlet structure results in the wall jet extending beyond the studied region of $3D_h$ along the major axis.

The chevron outlet modification results in similar flow fields along both axes to the baseline case, and the only significant change is the increase in velocity magnitude due to the influence of the flow blockage. Along the minor axis,

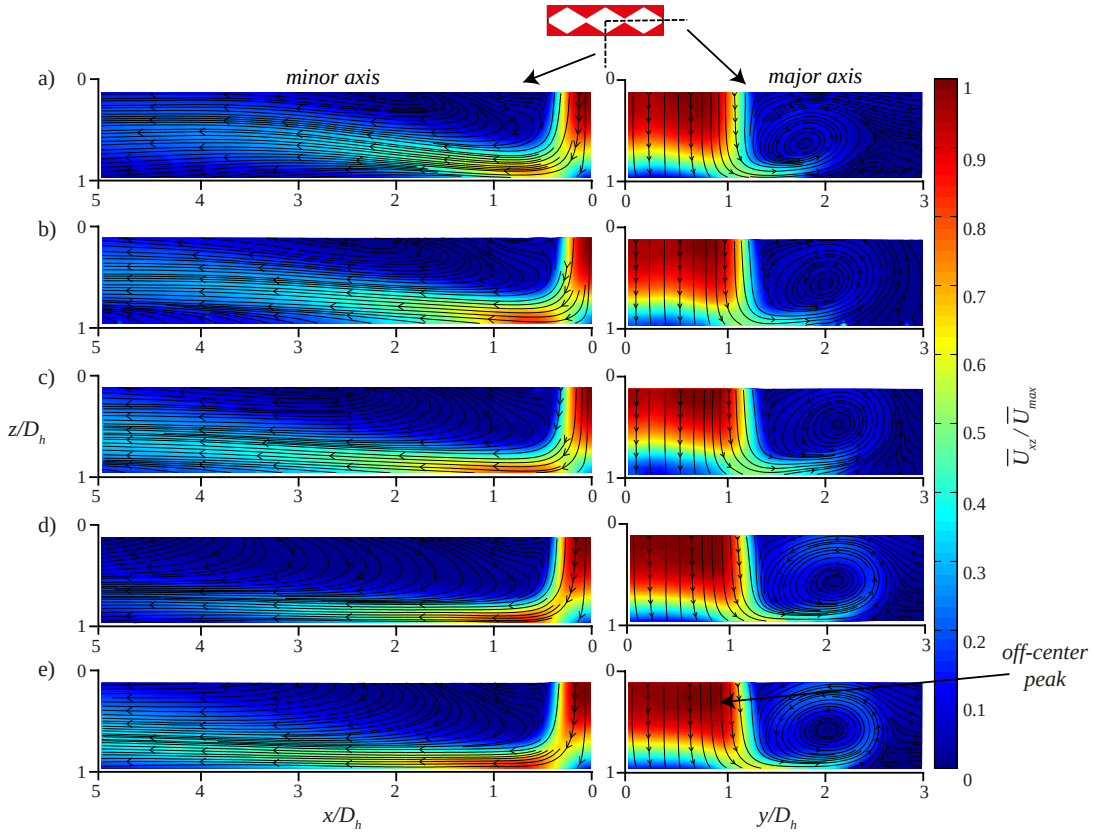

Figure 5.6: Normalised velocity magnitude contour plots and streamlines for the major chevron tab, along the major and minor axes, at a Reynolds number and $\bar{U}_{Max}$ of a) 100, 18.7mm/s b) 200, 33.9mm/s c) 300, 46.5mm/s d) 400, 55.2mm/s and e) 500, 67.62mm/s.

the wall jet develops up to and beyond the studied region of $5D_h$ and, when examining the velocity flow field along the major axis, the presence of off-center velocity peaks are evident within the impinging jet. Based on the uniform jet exit velocity profiles in Figure 5.4 (b), the off-center peaks are attributed to the same downstream fluid dynamics as the baseline case. In the wall jet zone, the length of the wall jet along the major axis is found to be shorter than that of the baseline case, for example at $Re_{Dh} = 500$, the wall jet detaches at $y/D_h \approx 2.25$, compared to $y/D_h \approx 2.5$ for the baseline case. As with the minor double tabs geometry, this is attributed to the enhanced spanwise spreading caused by the triangular tab geometry, and the associated location along the minor axis. For the contour tab

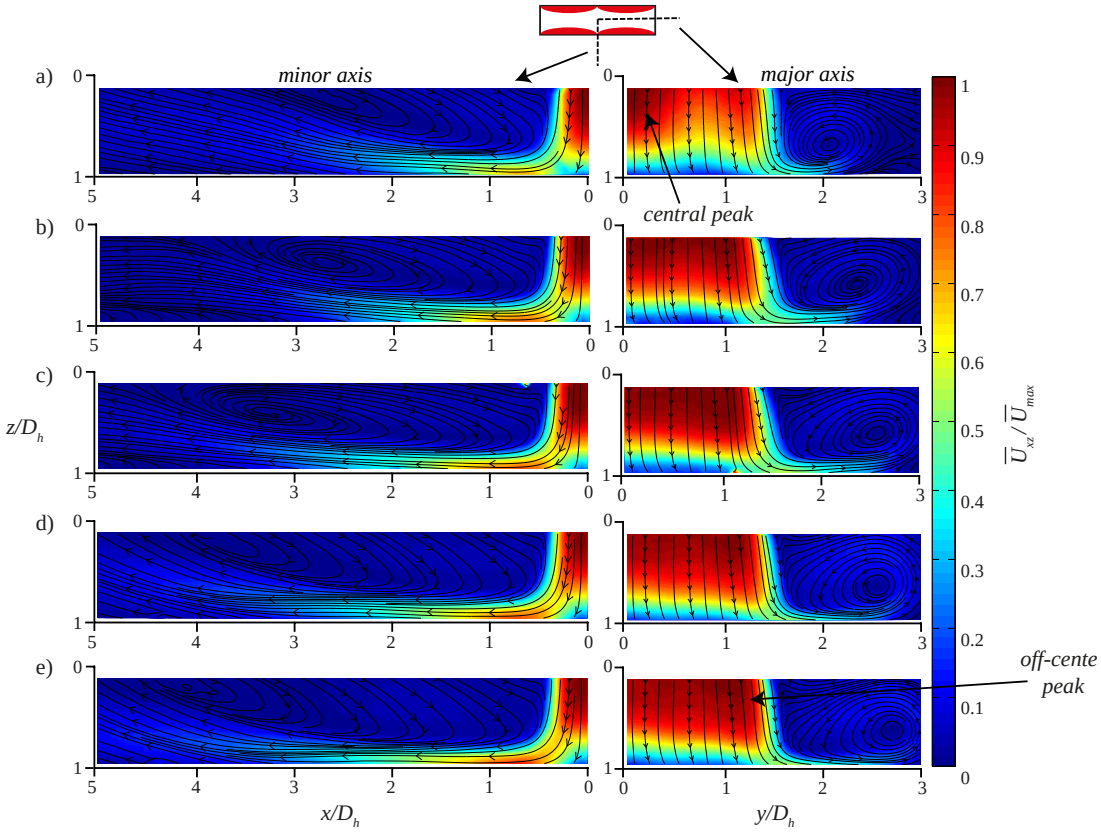

Figure 5.7: Normalised velocity magnitude contour plots and streamlines for the major contour tab, along the major and minor axes, at a Reynolds number and $\bar{U}_{Max}$ of a) 100, 22.4mm/s b) 200, 36.3mm/s c) 300, 49.9mm/s d) 400, 60.5mm/s and e) 500, 71.6mm/s.

geometry, the velocity field along the minor axis is also similar to the baseline slot jet, with the wall jet developing up to and beyond $5D_h$. Along the major axis, for $Re_{Dh} = 100$, a centrally located peak in maximum velocity is evident, and is also observed in the jet exit velocity profile in Figure 5.4 (c). Therefore, the presence of this peak is attributed to the tab geometry and location. Upon increasing the jet exit Reynolds number to $Re_{Dh} \geq 200$, the jet exit velocity profiles took on a more uniform distribution, without any local peaks; and off-center peaks are now evident in the velocity profile of the impinging jet. It is postulated that for $Re_{Dh} > 100$, the decrease in the axial velocity along the center of the jet, caused by the stagnation zone backpressure effect, would retard the centrally located

peak in the jet exit velocity and, thus, result in the formation of the off-center peak in velocity towards the edge of the major axis.

The velocity profiles detailed in this section, give an insight into the fluidic mechanisms resulting from the application of tabs at the jet outlet. In the next section, these will be compared to the local Nusselt numbers recorded, to see if they aid in understanding the distribution of the heat transfer coefficient along the impingement surface.

5.2 Heat Transfer

Figure 5.8 details the local Nusselt number distributions for all tested geometries and flow rates investigated. The differences in peak Nusselt number magnitude between geometries are as a result of the increased exit velocity caused by the larger blockage ratios. For the baseline case in Figure 5.8 (a), the existence of off-center peaks in the local Nusselt number are observed for all flow rates. These have been previously discussed in Chapter 4, and were attributed to the stagnation zone backpressure effect, and the entrainment of the ambient fluid surrounding the jet radially inwards – resulting in the presence of off-center peaks in the velocity profile of the impinging jet and, hence, enhanced removal of thermal energy from the heated surface. Outside of the stagnation zone, in the wall jet region, the monotonic decrease in Nusselt number due to the wall jet development is evident. Along the major axis, the local Nusselt number decreases sharply beyond the off-centre peaks – and is in good agreement with the wall jet profile observed in Figure 4.7.

5.2.1 Modifications to the Minor Axis

Figure 5.8 (b) and (c) give the corresponding local Nusselt number distributions for the minor double tabs and minor triangle cases, respectively. For the minor double tabs geometry, off-center peaks in Nusselt number are observed within the stagnation zone for all investigated flow rates. Based on the shape and location of these, as well as the velocimetry data in Figures 5.1 and 5.2 (a), these are attributed to the same fluidic mechanisms present in the baseline case. Outside

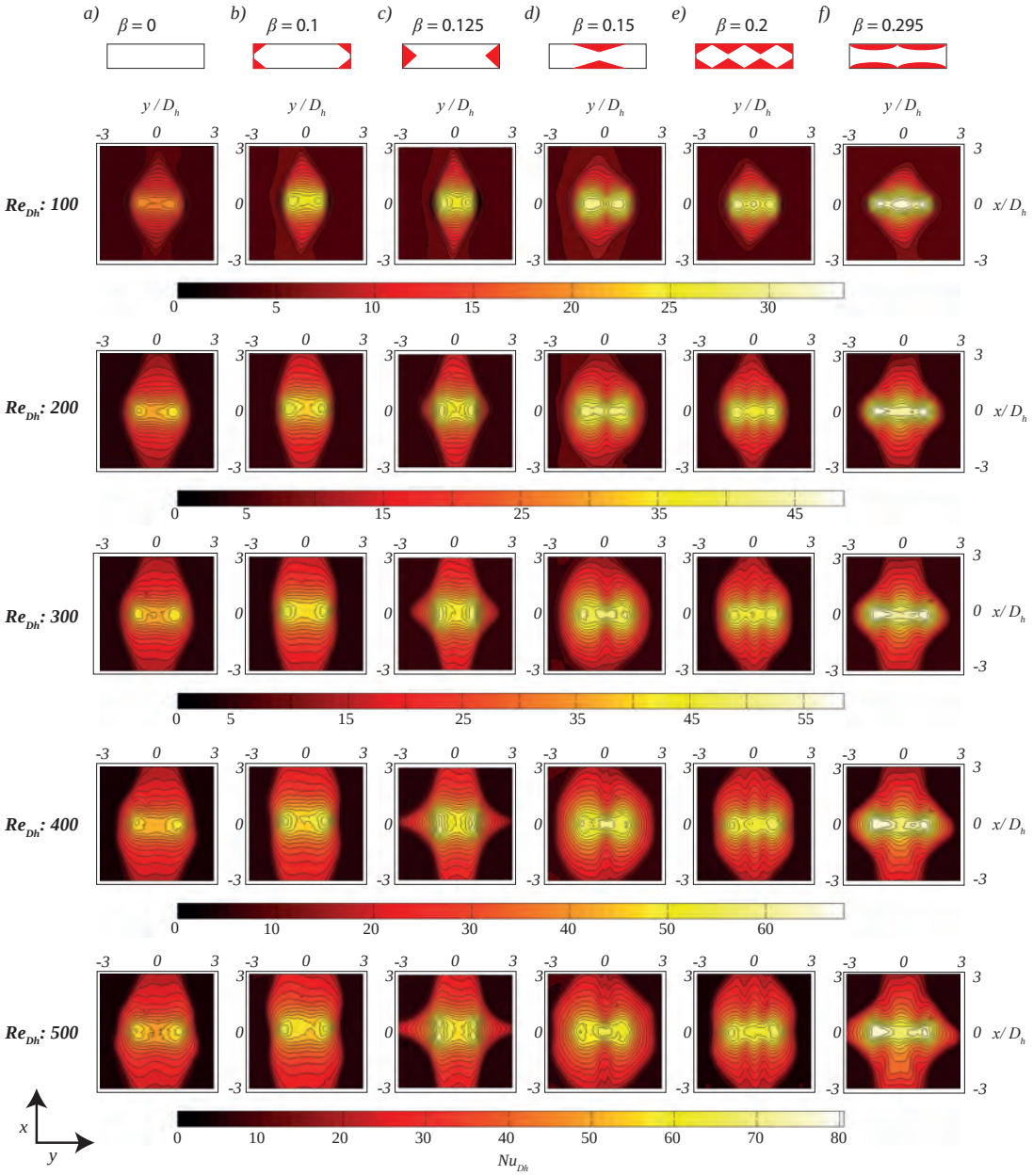

Figure 5.8: Local Nu_{Dh} distributions for all geometries $(a - f)$ as a function of Re_{Dh}, with a constant heat flux applied for all configurations. Nu_{Dh} and Re_{Dh} length scales are based off the hydraulic diameter of the non-tab case.

of the stagnation zone, along the wall jet zone, the triangular geometry of the tabs and their location along the minor axis, results in enhanced spanwise spreading of the wall jet when compared to the baseline case. However, this behaviour leads to a diminished wall jet along the major axis, and is in good agreement with what was previously discussed when examining Figure 5.2. Despite the small difference in flow blockage and tab design, the minor triangle case results in a much different local Nusselt number distribution to both the baseline case and the minor double tab geometry. Within the stagnation zone, for $Re_{Dh} \leq 300$, off-center peaks are present in Nusselt number, and these are attributed to the off-center peaks in the velocity profile of the impinging jet. However, upon increasing the Reynolds number to $Re_{Dh} \geq 400$, the local Nusselt number peaks split from two distinct off-centre peaks to four. This behaviour is postulated to be a result of the formation of regions of peak local velocity either side of the triangular tabs, and could also indicate that the potential core of the jet is impinging upon the target surface. These peaks were also noted in the work Gao *et al.* [99], when examining axisymmetric jets with triangular outlet tabs. They found that high velocity regions formed either side of the triangular tabs, which corresponded to regions of peak Nusselt number. Outside the stagnation zone, the minor triangle tab geometry promotes jet shear layer spreading in the major axis, with the wall jet extending further than that of the baseline and minor double tab geometries, and it appears to separate from the impingement surface beyond $y/D_{\mathrm{h}} = 3$ – as was observed in Figure 5.3. This behaviour is consistent with what was reported by Zaman *et al.* [102], when comparing the shear layer spreading characteristics of a slot jet against a slot jet with triangular tabs along the minor axis, for supersonic flow.

5.2.2 Modifications to the Major Axis

Figure 5.8 (d) - (f) detail the influence of outlet modifications to the major axis on the local heat transfer distribution. For all Reynolds numbers investigated, the local Nusselt number distributions are sensitive to the application of tabs along the major axis. The major triangle tab geometry, detailed in (d), creates a much different local Nusselt number distribution to all other tested geometries.

Within the stagnation region, for $Re_{Dh} \leq 200$, there exists two large regions of peak Nusselt number either side of the tab geometry. These differ in both shape and location to the off-center peaks found in the other geometries, and their existence is postulated to be as a result of the tab causing the jet to bifurcate into two separate jets – as was seen in Figure 5.5. Increasing the Reynolds number to $Re_{Dh} \geq 300$, there is a large centrally located peak in local Nusselt number observed. It postulated that an area of crossflow would be created where the bifurcated jets meet in the center, and the associated region of enhanced mixing was the fluidic mechanism resulting in the centrally located peak in Nusselt number. Outside the stagnation zone, the triangular geometry and location of the tabs appears to promote spreading of the jet shear layer along both axes – with a wall jet travelling outwards from the stagnation zone in all directions. The major triangle tab geometry completely negates the traditional saddle-back profile associated with slot jets [8; 95], and results in a Nusselt number distribution similar to the behaviour of jets in an array [54].

For the major chevron and contour tab geometries in Figure 5.8 (e) and (f), at $Re_{Dh} = 100$, three peaks in Nusselt number are observed within the stagnation, and the shape and magnitude of these are attributed to the tab geometry. Upon increasing the Reynolds number to $Re_{Dh} \geq 200$, however, the number of Nusselt number peaks reduces to two, which are located off-center. This is postulated to be as a result of the stagnation zone backpressure effect, and the resulting increased deceleration in the axial velocity at the center of the jet. Beyond the stagnation zone, the presence of the triangular tabs along the minor axis in (e), results in enhanced spanwise spreading of the wall jet along the impingement surface, and an associated diminution in the wall jet length along the major axis. This is in good agreement with what was observed for the minor double tab geometry, and corroborates the velocimetry data presented in Figure 5.6. The local Nusselt number distribution indicates that the major chevron tab results in similar jet shear layer spreading to the baseline and minor double tab geometries, with the wall jet in the minor axis providing the dominant heat transfer, and the major axis wall jet detaches from the impingement surface within the investigated region of $3D_h$. Along the major axis, the major contour tab geometry creates a similar surface heat transfer distribution to that of the minor triangle case in

Figure 5.8 (c), as there is a longer wall jet along the major axis, which appears to separate from the target surface outside of the investigated region of $3D_h$ for $Re_{Dh} \geq 300$ – consistent with the velocimetry data in Figure 5.7.

5.2.3 Area-averaged heat transfer

From the local Nusselt number distributions detailed in Figure 5.8, it is evident that the geometry and axial locations of the tabs has a considerable impact on the heat transfer distribution within the stagnation and wall jet zones. As modifications of similar flow blockage and axial location, result in very different local Nusselt number distributions within these zones. For $Re_{Dh} = 500$, Figure 5.10 presents the area-averaged Nusselt number as a function of the studied surface area along the impingement surface. The surface areas investigated are defined in regards to the hydraulic diameter (D_h), such that a square with sides of length $2D_h$ centered on the stagantion point ($x/D_h = y/D_h = 0$), results in a area of $4D_h^2$. It can be seen that for all surface areas, the application of an outlet tabs results in increased area-averaged heat transfer, when compared to the baseline case. For surface areas of $\leq 16D_h^2$, the contoured tab results in the greatest area-averaged Nusselt number. This is a result of the increased peaks in Nusselt

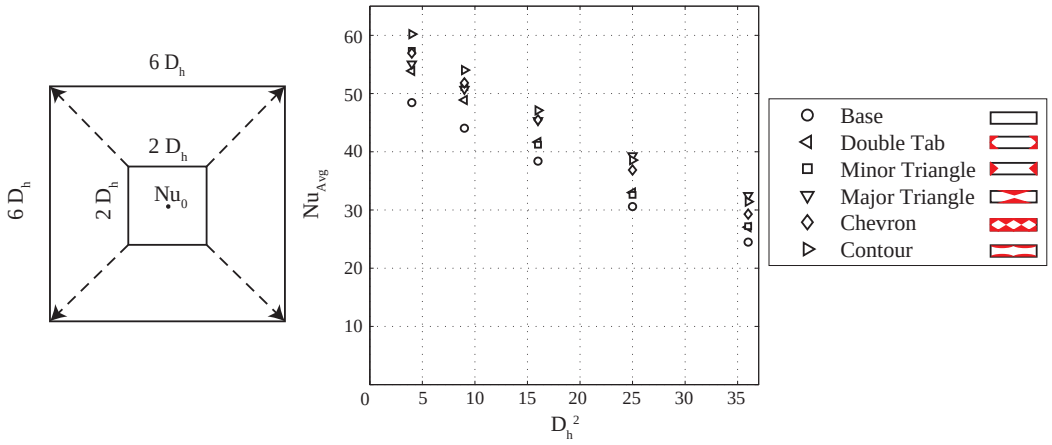

Figure 5.9: Nu_{Avg} as a function of the defined surface area along the impingement surface, for $Re_{Dh} = 500$.

number magnitude within the stagnation zone, caused by the higher blockage ratio resulting in greater peak velocities. However, it is interesting to note that despite having a lower open area ratio, increasing the surface area beyond $16D_h^2$ results in the major triangle geometry achieving the highest area-averaged Nusselt number. Therefore, it can be concluded that the area-averaged heat transfer is dependent on both tab geometry and the surface area over which the average is performed.

Figure 5.10 presents the area-averaged heat transfer for all geometries and flow rates studied, over a surface area of $36D_h^2$. When examining the modifications to the minor axis, there is no discernible advantage to either as – despite the differences in the local Nusselt number distributions – the maximum difference in area-averaged heat transfer is only 1.9%. For the tabs located on the major axis, all three resulted in higher area-averaged heat transfer coefficients than those located on the minor axis. The major triangle outperformed all geometries and achieved enhancements in area-averaged heat transfer of up to 47%, when compared to the baseline case. This is believed to be as a result of the increased wall jet spreading along both axes and the centrally located region of increased mixing, as a consequence of the tab geometry.

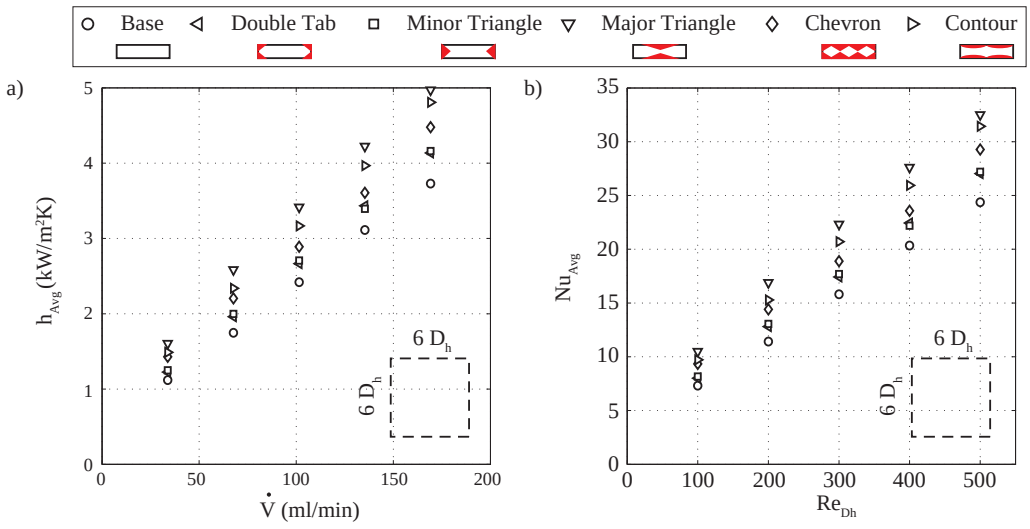

Figure 5.10: a) h_{Avg} as a function of $\dot{V}$ and b) Nu_{Avg} as a function of Re_{Dh}, for all geometries tested over an area of $36D_h^2$ along the major and minor axes.

5.3 Head loss

Given that the major triangle achieved higher area-averaged heat transfer coefficients than the major chevron and major contour tabs, while having a lower blockage ratio, indicated that it was the preferred tab geometry of all those tested. Nevertheless, an effective characterisation of a liquid cooling solution must also investigate the hydrodynamic losses associated with each geometry, to understand the practical cost of any enhancements achieved. Therefore, a pressure drop (ΔP) analysis was carried out on all tab geometries and flow rates investigated, and the results of which are presented in Figure 5.11.

In line with the literature [99], U_{mean} was based on that of the baseline case in calculating K for all geometries. As with the analysis of head loss coefficient in Figure 4.15, with increasing Reynolds number, the head loss coefficients in Figure 5.11 (b) begin to asymptote towards a constant value. It can seen that for all geometries, the flow begins to trantion towards turbulent flow for $Re_{Dh} \geq 150$. Given its significant impact on the design and performance of microscale liquid cooling systems, the required pumping power ($P_{Pump} = \dot{V}\Delta P$) was calculated for each geometry. By determining the head loss coefficient as

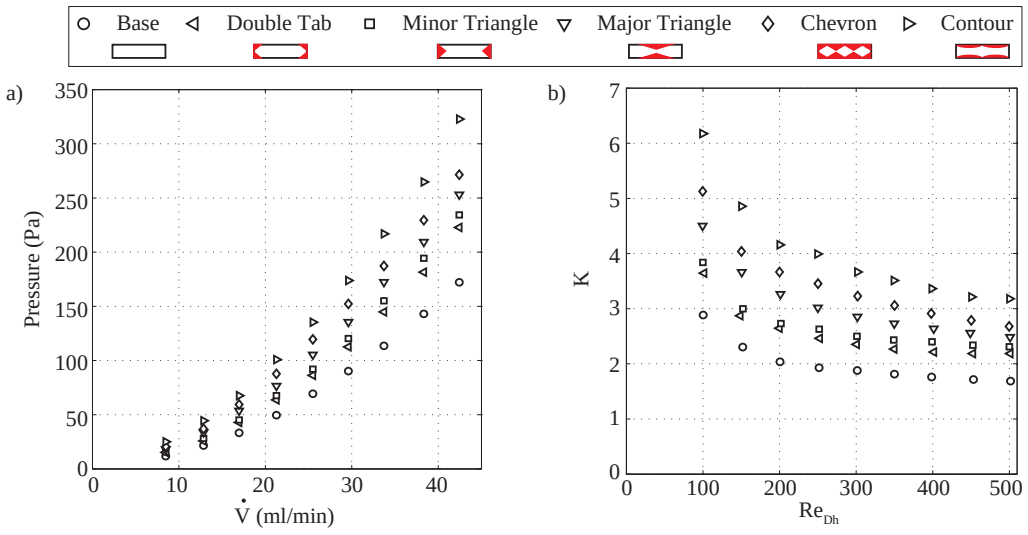

Figure 5.11: (a) Pressure drop (ΔP) as a function of volumetric flow rate ($\dot{V}$) and (b) Head loss coefficient (K) as a function of Re_{Dh}.

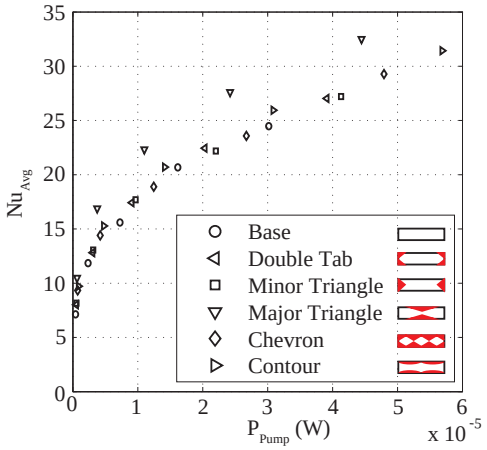

Figure 5.12: Area-averaged Nusselt number (Nu_{Avg}) as a function of pumping power (P_{Pump}) for all geometries tested, over an area of $3D_h$ along both axes.

a function of Reynolds number, in Figure 5.11 (b), nozzle pressure drop values for the heat transfer measurement facility were determined through dimensionless scaling techniques. Once the pressure drops and volumetric flow rates were known, it was then possible to plot Nu_{Avg} as a function of the required pumping power ($P_{Pump} = \dot{V}\Delta P$) in Figure 5.12. From an examination of Figure 5.12, it is evident that the major triangle geometry outperformed all tested geometries and, for the same pumping power, achieves enhancements in area-averaged heat transfer removal of up to 29% over the baseline case.

5.4 Closure

This chapter investigated the influence of jet outlet structures, in the form of tabs and chevrons, on the thermal and hydrodynamic behaviour of low Reynolds number, confined, liquid slot jets. Using PIV, it was possible to capture the 2D velocity flow fields associated with each geometry, along the major and minor axes. When examining the jet exit velocity profiles along the major axis, the geometry and location of the outlet structures influenced the shape of the profiles, but did not result in the presence of the observed off-center peaks in the velocity profile. Instead, the off-center peaks were postulated to be as a result of the stagnation zone backpressure effect and local flow entrainment, previously

discussed in Chapter 4. For the major triangle tab, the shape and location of the tab geometry was seen to cause the jet to bifurcate into two separate jets, located either side of the tab geometry.

The Joule-heated foil technique was successful in capturing influence of tab geometry and open area-ratio (β) on the distribution of local Nusselt number along the target surface. The differences in peak Nusselt number magnitude between geometries were a result of the increased local exit velocity, caused by the larger blockage ratios. Within the stagnation zone, regions of peak Nusselt number were recorded for all geometries and flow rates investigated. The shape and magnitude of these peaks were found to be sensitive to the location and geometry of the tabs, as well as the jet exit Reynolds numbers. The major triangle tab geometry resulted in a very different local Nusselt number distribution to all other tested geometries. For $Re_{Dh} \leq 200$, two large regions of peak Nusselt number existed within the stagnation zone, which were different in both shape and location to the off-center peaks observed with all other geometries. These were concluded to be a result of the bifurcating jet caused by the tab geometry, and recorded in the jet exit velocity profiles. A centrally located peak was then found for $Re_{Dh} \geq 300$, and postulated to be a result of a region of enhanced mixing at the center of the stagnation zone, due to jet crossflow. All jet outlet tabs resulted in enhancements in area-averaged heat transfer when compared to the baseline slot jet. Over the studied region of $3D_h$, the major triangle tab geometry resulted in an enhancement of area-averaged Nusselt number of up to 47%, when compared to the baseline jet.

Through a pressure drop analysis, it was possible to determine the hydrodynamic cost of any enhancements in heat transfer achieved. Given the significance of required pumping in the design and specification of a microelectronics cooling solution, the area-averaged heat transfer was plotted as a function of required pumping power for each geometry and flow rate investigated. From this, it was found that the major triangle geometry was the most favourable for the TIPS project, as it outperformed all tested geometries and, for the same pumping power, it achieved enhancement in area-averaged heat transfer of up to 29% in comparison with the baseline case.

The appearance of saddle-back profiles and off-center peaks along the impingement surface for confined slot jets can result in spatial temperature gradients, which can induce thermomechanical stresses in semiconductor materials. Unless these off-center peaks are utilised for targeted hot-spot cooling, they are unsuitable for a critical microelectronics cooling solution. Due to the absence of the saddle-back behaviour – and enhancement in area-averaged heat transfer without incurring additional hydrodynamic losses – the application of a confined slot jet featuring the major triangle tab geometry could be a potential primary or secondary heat exchanger for the TIPS project.

Chapter 6

Conclusions and Future Directions

6.1 Summary

The influence of jet nozzle geometry modification on the thermal and hydrodynamic behavior of confined and normally impinging slot jets was investigated in this thesis. To enable this, experimental test facilities were manufactured to measure the 2D velocity flow fields, local and area-averaged heat transfer coefficients along the impingement surface, and pressure drops across each investigated nozzle geometry. The slot jets investigated featured five different nozzle aspect ratios (L/W), and five different outlet structures in the form of tabs and chevrons. The slot jet nozzle orifice plates had a plate thickness to hydraulic diameter ratio (t/D_h) of 1, and were maintained at a fixed confinement ratio within the test section of $H/D_h = 1$. The geometries were tested over a Reynolds number range, based on jet nozzle hydraulic diameter, of between $100 \leq Re_{Dh} \leq 500$. In all cases, the velocimetry data was found to agree very closely with the local Nusselt number distributions, and the head loss measurements determined the practical cost of any enhancements in heat transfer achieved. The main findings are detailed in this chapter.

6.2 Conclusions

6.2.1 Aspect Ratio Investigation

- For the slot jet with an aspect ratio of 1, as the jet discharged from the nozzle exit, the shear-driven interaction between the jet and the surrounding fluid results in the entrainment of ambient fluid in towards the jet exit, and the formation of a recirculating vortex (denoted as the primary vortex). The primary vortex was found to move radially outwards with increasing jet exit Reynolds number.

- As the jet expanded radially outwards from the stagnation zone, a wall jet formed along the impingement surface. In the absence of the positive pressure gradient found within the stagnation zone, the thermal and hydrodynamic boundary layers began to develop and thicken, resulting in a corresponding monotonic decrease in Nusselt number – and convergence towards a fully thermally developed profile.

- As the wall jet progressed radially outwards along the impingement surface, it reached a point where it was unable to overcome the frictional effects of the wall, and the flow retarding influence of the primary vortex. This resulted in the wall jet detaching from the impingement surface, and a corresponding sharp decrease in Nusselt number. The point of wall jet detachment was found to be dependent on the jet exit Reynolds number. For all flow rates investigated, the wall jet was found to reattach to the impingement surface downstream and, at higher Reynolds numbers, the detachment and reattachment was associated with a secondary recirculating vortex and a local maximum in Nusselt number. Beyond the point of reattachment, the wall jet continued to develop as it progressed radially outwards.

- For the slot jet with aspect ratios greater than 1, off-center peaks were observed in the local Nusselt number distributions along the major axis. Unlike in previous studies, these were not found to be a result of off-center

peaks in the jet exit velocity profiles, caused by upstream flow conditions. Instead, they were postulated to be a result of the stagnation zone fluid dynamics resulting in deceleration of the centerline axial velocity. This, coupled with the entrainment of fluid radially inwards towards the jet, would result in enhanced mass flow rate towards the edge of the major axis of the impingement region and, consequently, an increase in the removal of thermal energy from a heated surface.

- Correlations developed from the experimental results showed that the stagnation point Nusselt number (Nu_0) had a very weak dependency on the jet nozzle aspect ratio ($(L/W)^{-0.004}$), but scaled with $Re_{Dh}^{0.55}$. This Reynolds number scaling was consistent with the presence of a laminar boundary layer within the stagnation zone and, consequently, the presence of potential core impingement.

- The area-averaged Nusselt number (Nu_{Avg}) was found to have a stronger dependency on both jet exit Reynolds number ($Re_{Dh}^{0.775}$) and aspect ratio ($(L/W)^{0.182}$). Over the range of Reynolds numbers investigated, it was determined that increasing the aspect ratio of a confined laminar slot jet from 1 to 8 resulted in an increase in area-averaged heat transfer removal of up to 68%.

- Measurements of the pressure drop through each slot jet geometry found that the head loss coefficient (K) was also sensitive to the jet exit Reynolds number ($Re_{Dh}^{-0.29}$) and, to a lesser extent, aspect ratio ($(L/W)^{-0.052}$). It was concluded that increasing the aspect ratio from 1 to 8, resulted in a reduction of up to 12% in head loss coefficient and, consequently, an increase in Nu_{Avg}/K of 63.5%.

6.2.2 Tabs & Chevrons

- Within the stagnation zone, the application of passive structures resulted in the control and enhancement of peak heat transfer regions. The magnitudes of these peaks were sensitive to jet exit Reynolds number and open area

ratio β, whereas the shape and number of peaks was dependent on tab geometry and Reynolds number.

- By examination of the local temperature and velocity flow fields, it was found that in the wall jet zone, passive structures would significantly impact the formation and spanwise spreading of the jet shear layer when compared to a conventional slot jet. Therefore, tabs and chevrons can be utilized to control the formation, strength, and location of wall jets along the impingement surface.

- Compared to the baseline case, all tab geometries resulted in enhancements in area-averaged Nusselt number. Through the pressure drop analysis, however, it was found that the major triangle tab geometry outperformed all others and achieved enhancements in area-averaged heat transfer coefficient of up to 29%, without incurring any significant additional hydrodynamic penalties.

- With regards to the TIPS project, the major triangle tab geometry showed the greatest potential for a primary or secondary heat exchanger. This was as a result of the absence of the traditional saddle-back behavior associated with confined and impinging slot jets, as well as the enhancements achieved in area-averaged heat transfer without incurring additional hydrodynamic losses

The results of this investigation provided an insight into the thermal and hydrodynamic behaviour of confined laminar liquid slot jets, and will allow designers of slot jet systems a method of achieving flexibility, enhancement, and control for targeted hot-spot cooling, to negate the spatial non-uniformities and saddle-back profiles associated with conventional slot jets – without incurring additional hydrodynamic losses. Due to their scalability, ease of manufacture, and geometric compatibility, one particular application of these jets would be as primary heat exchangers for the thermal management of microelectronics, such as required in the proposed TIPS architecture.

6.3 Future Work

This section details the future work recommended based on the results of this thesis.

- The PIV measurement facility was successful in capturing the velocity fields along the major and minor axes, and aided in understanding some of the observed local Nusselt number features. Slot jets can feature complex 3D flow fields, however, especially in the presence of jet outlet structures generating spanwise vortices. In order to fully understand the fluidic mechanisms present – such as the appearance of off-center peaks – the use of Stereo PIV is recommended. Stereo PIV would allow for the simultaneous measurement of all three velocity components, and the generation of 3D velocity vector fields. Together with the measured local Nusselt number distributions, Stereo PIV would further the understanding of nozzle geometry modification and outlet structures on the thermal and hydrodynamic behaviour of slot jets.

- Based on the correlations provided for the local and area-averaged heat transfer coefficients, numerical simulations of heat transfer along the impingement surface could be validated. Once validated, these models would allow for a parametric study of various jet nozzle geometries, and the potential to achieve further enhancements in heat transfer without the expense of extensive experimentation. Similarly, if Stereo PIV is not feasible, a three-dimensional transient simulation of the impinging jet could be validated with the captured 2D flow fields. This would then allow for the complex flow phenomenon to be captured and understood.

- The application of this research is to aid in the design of a heat exchanger for a microfluidic cooling package in the TIPS project. Therefore, it is recommended to realise the proposed slot jet designs at the microscale, using microfabrication techniques. Their integration into the TIPS project as either a primary or secondary heat exchanger could then be investigated, prior to the use of the cooling solution in a critical application.

References

[1] D. Evans, The internet of things: How the next evolution of the internet is changing everything, Cisco White Paper (2011). v, 2

[2] Cisco, The zettabyte era: Trends and analysis, Cisco white paper (2016). v, 2

[3] Cisco, Connections counter: The internet of everything in motion (2013). URL https://newsroom.cisco.com/feature-content?type=webcontent&articleId=1208342 v, 2

[4] N. Jeffers, J. Stafford, K. Nolan, B. Donnelly, R. Enright, J. Punch, A. Waddell, L. Ehrlich, J. O'Connor, A. Sexton, R. Blythman, D. Hernon, Microfluidic cooling of photonic integrated circuits (pics), in: 4th European Conference on Microfluidics 10th -12th December 2014 Limerick, Ireland, Limerick, Ireland, 2014. v, 3, 4, 7, 10, 28

[5] R. Enright, S. Lei, K. Nolan, I. Mathews, A. Shen, G. Levaufre, R. Frizzell, G.-H. Duan, D. Hernon, A vision for thermally integrated photonics systems, Bell Labs Technical Journal 19 (2014) 31–45. v, 5, 6, 7, 28

[6] A. Sivasamy, V. Selladurai, P. Rajesh Kanna, Numerical simulation of two-dimensional laminar slot-jet impingement flows confined by a parallel wall, International Journal for Numerical Methods in Fluids 55 (10) (2007) 965–983. v, 29, 30, 73, 74, 75, 76, 82

[7] H. Lee, b. Yoon, M. Ha, A numerical investigation on the fluid flow and heat transfer in the confined impinging slot jet in the low reynolds number region for different channel heights, International Journal of Heat and Mass Transfer 51 (15) (2008) 4055–4068. v, 30, 73, 75, 81

[8] I. Sezai, A. Mohamad, Three-dimensional simulation of laminar rectangular impinging jets, flow structure, and heat transfer, Journal of heat transfer 121 (1) (1999) 50–56. v, viii, 31, 32, 72, 78, 83, 85, 104

[9] N. Alliance, 5g white paper, Next Generation Mobile Networks, White paper. 2

[10] M. Ellsworth, L. Campbell, R. Simons, M. Iyengar, R. Schmidt, R. Chu, The evolution of water cooling for ibm large server systems: Back to the future, in: Thermal and Thermomechanical Phenomena in Electronic Systems, 2008. ITHERM 2008. 11th Intersociety Conference on, IEEE, 2008, pp. 266–274. 8

[11] V. Singhal, S. V. Garimella, A. Raman, Microscale pumping technologies for microchannel cooling systems, Applied Mechanics Reviews 57 (3) (2004) 191–221. 9

[12] P.-S. Lee, S. V. Garimella, D. Liu, Investigation of heat transfer in rectangular microchannels, International Journal of Heat and Mass Transfer 48 (9) (2005) 1688–1704. 10

[13] I. Hassan, P. Phutthavong, M. Abdelgawad, Microchannel heat sinks: an overview of the state-of-the-art, Microscale thermophysical engineering 8 (3) (2004) 183–205. 10

[14] S. V. Garimella, C. B. Sobhan, Transport in microchannels-a critical review, Annual review of heat transfer 13 (13). 10

[15] C. B. Sobhan, S. V. Garimella, A comparative analysis of studies on heat transfer and fluid flow in microchannels, Microscale Thermophysical Engineering 5 (4) (2001) 293–311. 10

[16] A. Robinson, A thermal-hydraulic comparison of liquid microchannel and impinging liquid jet array heat sinks for high-power electronics cooling, Components and Packaging Technologies, IEEE Transactions on 32 (2) (2009) 347–357. 10, 11, 28

[17] S. Choi, R. F. Barron, R. Warrington, Fluid flow and heat transfer in microtubes, in: ASME DSC, Vol. 32, 1991, pp. 123–134. 10

[18] X. Peng, G. Peterson, B. Wang, Heat transfer characteristics of water flowing through microchannels, Experimental Heat Transfer An International Journal 7 (4) (1994) 265–283. 10

[19] X. Peng, G. Peterson, Convective heat transfer and flow friction for water flow in microchannel structures, International journal of heat and mass transfer 39 (12) (1996) 2599–2608. 10

[20] G. L. Morini, Single-phase convective heat transfer in microchannels: a review of experimental results, International Journal of Thermal Sciences 43 (7) (2004) 631–651. 10

[21] E. Gutmark, F. Grinstein, Flow control with noncircular jets 1, Annual review of fluid mechanics 31 (1) (1999) 239–272. 11, 28, 34

[22] P. Gulati, V. Katti, S. Prabhu, Influence of the shape of the nozzle on local heat transfer distribution between smooth flat surface and impinging air jet, International Journal of Thermal Sciences 48 (3) (2009) 602 – 617. 11, 28

[23] W. Tabakoff, W. Clevenger, Gas turbine blade heat transfer augmentation by impingement of air jets having various configurations, Journal of Engineering for power 94 (1) (1972) 51–58. 14

[24] D. E. Hall, F. P. Incropera, R. Viskanta, Jet impingement boiling from a circular free-surface jet during quenching: Part 1single-phase jet, Journal of heat transfer 123 (5) (2001) 901–910. 14

[25] F. Monnoyer, D. Lochegnies, Heat transfer and flow characteristics of the cooling system of an industrial glass tempering unit, Applied Thermal Engineering 28 (17) (2008) 2167–2177. 14

[26] L. F. Geers, M. J. Tummers, K. Hanjalić, Experimental investigation of impinging jet arrays, Experiments in fluids 36 (6) (2004) 946–958. 15

[27] N. Zuckerman, N. Lior, Jet impingement heat transfer: Physics, correlations, and numerical modeling, Advances in heat transfer 39 (06) (2006) 565–631. 15, 44

[28] S. V. Garimella, R. Rice, Confined and submerged liquid jet impingement heat transfer, Journal of Heat Transfer 117 (4) (1995) 871–877. 15, 16, 22, 23, 24, 25, 28, 58, 59, 75, 81, 86

[29] J. Lienhard, Liquid jet impingement, Annual Review of Heat Transfer 6 (6). 15

[30] B. Webb, C.-F. Ma, Single-phase liquid jet impingement heat transfer, Advances in heat transfer 26 (1995) 105–217. 15, 28

[31] H. Martin, Heat and mass transfer between impinging gas jets and solid surfaces, Advances in heat transfer 13 (1977) 1–60. 15, 16, 17, 24, 25, 28

[32] R. S. Snedeker, et al., A study of free jet impingement. part 1. mean properties of free and impinging jets, Journal of fluid Mechanics 45 (02) (1971) 281–319. 15

[33] S. Polat, B. Huang, A. S. Mujumdar, W. Douglas, Numerical flow and heat transfer under impinging jets: a review, Annual Review of Heat Transfer 2 (2). 15

[34] M. D. Deshpande, R. N. Vaishnav, Submerged laminar jet impingement on a plane, Journal of Fluid Mechanics 114 (1982) 213–236. 16

[35] D. Womac, S. Ramadhyani, F. Incropera, Correlating equations for impingement cooling of small heat sources with single circular liquid jets, Journal of heat transfer 115 (1) (1993) 106–115. 16

[36] D. H. Lee, J. Song, M. C. Jo, The effects of nozzle diameter on impinging jet heat transfer and fluid flow, Journal of Heat Transfer 126 (4) (2004) 554–557. 16

[37] S. Ashforth-Frost, K. Jambunathan, Effect of nozzle geometry and semi-confinement on the potential core of a turbulent axisymmetric free jet, International Communications in Heat and Mass Transfer 23 (2) (1996) 155–162. 16, 20, 77

[38] W. Quinn, Turbulent free jet flows issuing from sharp-edged rectangular slots: the influence of slot aspect ratio, Experimental thermal and fluid science 5 (2) (1992) 203–215. 16

[39] S. Ashforth-Frost, K. Jambunathan, C. Whitney, Velocity and turbulence characteristics of a semiconfined orthogonally impinging slot jet, Experimental Thermal and Fluid Science 14 (1) (1997) 60–67. 16, 19

[40] D. Lee, R. Greif, S. Lee, J. Lee, Heat transfer from a flat plate to a fully developed axisymmetric impinging jet, Journal of heat transfer 117 (3) (1995) 772–776. 16

[41] D. Zhou, S.-J. Lee, Forced convective heat transfer with impinging rectangular jets, International Journal of Heat and Mass Transfer 50 (910) (2007) 1916 – 1926. 16, 26, 80

[42] A. Sfeir, The velocity and temperature fields of rectangular jets, International Journal of Heat and Mass Transfer 19 (11) (1976) 1289–1297. 16

[43] S. Akaike, M. Nemoto, Potential core of a submerged laminar jet, Journal of fluids engineering 110 (4) (1988) 392–398. 16

[44] P. Hrycak, Experimental flow characteristics of a single turbulent jet impinging on a flat plate, National Aeronautics and Space Administration, 1970. 16

[45] H. Miyazaki, E. Silberman, Flow and heat transfer on a flat plate normal to a two-dimensional laminar jet issuing from a nozzle of finite height, International Journal of Heat and Mass Transfer 15 (11) (1972) 2097–2107. 17

[46] R. Gardon, J. C. Akfirat, The role of turbulence in determining the heat-transfer characteristics of impinging jets, International Journal of Heat and Mass Transfer 8 (10) (1965) 1261–1272. 17, 24, 80, 86

[47] C. O. Popiel, O. Trass, Visualization of a free and impinging round jet, Experimental Thermal and Fluid Science 4 (3) (1991) 253–264. 17, 18

[48] M. Poreh, Y. Tsuei, J. E. Cermak, Investigation of a turbulent radial wall jet, Journal of Applied Mechanics 34 (2) (1967) 457–463. 18

[49] J. Fitzgerald, S. Garimella, Flow field effects on heat transfer in confined jet impingement, Journal of heat transfer 119 (3) (1997) 630–632. 19

[50] M. Behnia, S. Parneix, Y. Shabany, P. Durbin, Numerical study of turbulent heat transfer in confined and unconfined impinging jets, International Journal of Heat and Fluid Flow 20 (1) (1999) 1–9. 19

[51] N. Gao, D. Ewing, Investigation of the effect of confinement on the heat transfer to round impinging jets exiting a long pipe, International journal of heat and fluid flow 27 (1) (2006) 33–41. 19

[52] D. Wolf, R. Viskanta, F. Incropera, Local convective heat transfer from a heated surface to a planar jet of water with a nonuniform velocity profile, Journal of Heat Transfer 112 (4) (1990) 899–905. 20

[53] S. V. Garimella, B. Nenaydykh, Nozzle-geometry effects in liquid jet impingement heat transfer, International Journal of Heat and Mass Transfer 39 (14) (1996) 2915–2923. 20

[54] L. F. G. Geers, Multiple impinging jet arrays. An experimental study on flow and heat transfer, TU Delft, Delft University of Technology, 2004. 20, 98, 104

[55] J. Lee, S.-J. Lee, The effect of nozzle configuration on stagnation region heat transfer enhancement of axisymmetric jet impingement, International Journal of Heat and Mass Transfer 43 (18) (2000) 3497–3509. 20, 23, 72, 77

[56] J. Lee, S.-J. Lee, The effect of nozzle aspect ratio on stagnation region heat transfer characteristics of elliptic impinging jet, International Journal of Heat and Mass Transfer 43 (4) (2000) 555 – 575. 20, 28, 31, 59, 83, 86

[57] N. D. Mohan, D. Greenblatt, C. Nayeri, C. Paschereit, N. Panchapakesan, Vortex-enhanced mixing through active and passive flow control methods, Experiments in Fluids 56 (3) (2015) 1–16. 20

[58] D. A. Tamburello, M. Amitay, Active control of a free jet using a synthetic jet, International Journal of Heat and Fluid Flow 29 (4) (2008) 967–984. 20

[59] C.-M. Ho, E. Gutmark, Vortex induction and mass entrainment in a small-aspect-ratio elliptic jet, Journal of Fluid Mechanics 179 (1987) 383–405. 21

[60] J. Foss, S. Kleis, Mean flow characteristics for the oblique impingement of an axlisymmetric jet, AIAA journal 14 (6) (1976) 705–706. 21

[61] J. F. Foss, Measurements in a large-angle oblique jet impingement flow, AIAA Journal 17 (8) (1979) 801–802. 21

[62] T. S. ODonovan, D. B. Murray, Fluctuating fluid flow and heat transfer of an obliquely impinging air jet, International Journal of Heat and Mass Transfer 51 (25) (2008) 6169–6179. 21

[63] K. Choo, T. Y. Kang, S. J. Kim, The effect of inclination on impinging jets at small nozzle-to-plate spacing, International Journal of Heat and Mass Transfer 55 (13) (2012) 3327–3334. 21

[64] D. Zhou, S.-J. Lee, Heat transfer enhancement of impinging jets using mesh screens, International journal of heat and mass transfer 47 (10) (2004) 2097–2108. 21

[65] P. Nakod, S. Prabhu, R. Vedula, Heat transfer augmentation between impinging circular air jet and flat plate using finned surfaces and vortex generators, Experimental thermal and fluid science 32 (5) (2008) 1168–1187. 21

[66] H. Sun, C. Ma, W. Nakayama, Local characteristics of convective heat transfer from simulated microelectronic chips to impinging submerged round water jets, Journal of Electronic Packaging 115 (1) (1993) 71–77. 22, 23, 58, 86

[67] C. Chang, G. Kocamustafaogullari, F. Landis, S. Downing, Single and multiple liquid jet-impingement heat transfer, Heat transfer in turbulent flows- 1993 (1993) 43–52. 22

[68] C. Ma, A. Bergles, Convective heat transfer on a small vertical heated surface in an impinging circular liquid jet, Heat Transfer Science and Technology 1988 (1988) 193–200. 22, 23

[69] C.-Y. Li, S. V. Garimella, Prandtl-number effects and generalized correlations for confined and submerged jet impingement, International Journal of Heat and Mass Transfer 44 (18) (2001) 3471–3480. 23, 25

[70] D. Lytle, B. Webb, Air jet impingement heat transfer at low nozzle-plate spacings, International Journal of Heat and Mass Transfer 37 (12) (1994) 1687–1697. 23

[71] J. Holman, Heat Transfer, McGraw-Hill Education, 2009. 24, 49, 62, B2

[72] D. Vader, F. Incropera, R. Viskanta, Local convective heat transfer from a heated surface to an impinging, planar jet of water, International Journal of Heat and Mass Transfer 34 (3) (1991) 611–623. 24

[73] Y. Chen, C.-F. Ma, M. Qin, Y. Li, Forced convective heat transfer with impinging slot jets of meso-scale, International journal of heat and mass transfer 49 (1) (2006) 406–410. 24, 27, 28, 31, 35

[74] K. S. Choo, Y. J. Youn, S. J. Kim, D. H. Lee, Heat transfer characteristics of a micro-scale impinging slot jet, International Journal of Heat and Mass Transfer 52 (1314) (2009) 3169 – 3175. 24, 26, 28

[75] R. Goldstein, A. Behbahani, K. K. Heppelmann, Streamwise distribution of the recovery factor and the local heat transfer coefficient to an impinging circular air jet, International journal of heat and mass transfer 29 (8) (1986) 1227–1235. 25

[76] Z. Lin, Y. Chou, Y. Hung, Heat transfer behaviors of a confined slot jet impingement, International Journal of Heat and Mass Transfer 40 (5) (1997) 1095–1107. 26, 28, 31, 35

[77] S. Al-Sanea, A numerical study of the flow and heattransfer characteristics of an impinging laminar slot-jet including crossflow effects, International journal of heat and mass transfer 35 (10) (1992) 2501–2513. 26

[78] D. Colucci, R. Viskanta, Effect of nozzle geometry on local convective heat transfer to a confined impinging air jet, Experimental Thermal and Fluid Science 13 (1) (1996) 71–80. 25, 74, 81

[79] D. H. Lee, J. R. Bae, H. J. Park, J. S. Lee, P. Ligrani, Confined, milliscale unsteady laminar impinging slot jets and surface nusselt numbers, International Journal of Heat and Mass Transfer 54 (11) (2011) 2408–2418. 27, 28, 31

[80] D. H. Lee, J. R. Bae, M. Ryu, P. Ligrani, Confined, milliscale unsteady laminar impinging slot jets: Effects of slot width on surface stagnation point nusselt numbers, Journal of Electronic Packaging 134 (4) (2012) 041004. 27, 28, 31

[81] Y. Shi, M. Ray, A. Mujumdar, Effects of prandtl number on impinging jet heat transfer under a semi-confined turbulent slot jet, International communications in heat and mass transfer 29 (7) (2002) 929–938. 27

[82] H. Sun, C. Ma, Y. Chen, Prandtl number dependence of impingement heat transfer with circular free-surface liquid jets, International journal of heat and mass transfer 41 (10) (1998) 1360–1363. 27

[83] C. Y. Li, S. V. Garimella, Prandtl-number effects and generalized correlations for confined and submerged jet impingement, International Journal of Heat and Mass Transfer 44 (18) (2001) 3471–3480. 27, 59, 86

[84] Q. Li, Y. Xuan, F. Yu, Experimental investigation of submerged single jet impingement using cu–water nanofluid, Applied Thermal Engineering 36 (2012) 426–433. 27

[85] T. Yousefi, E. Shojaeizadeh, H. Mirbagheri, B. Farahbaksh, M. Saghir, An experimental investigation on the impingement of a planar jet of al 2 o 3–water nanofluid on a v-shaped plate, Experimental Thermal and Fluid Science 50 (2013) 114–126. 27, 28

[86] O. Manca, P. Mesolella, S. Nardini, D. Ricci, Numerical study of a confined slot impinging jet with nanofluids, Nanoscale research letters 6 (1) (2011) 1–16. 27

[87] V. A. Chiriac, A. Ortega, A numerical study of the unsteady flow and heat transfer in a transitional confined slot jet impinging on an isothermal surface, International Journal of Heat and Mass Transfer 45 (6) (2002) 1237–1248. 28, 31, 35

[88] M. Zukowski, Heat transfer performance of a confined single slot jet of air impinging on a flat surface, International Journal of Heat and Mass Transfer 57 (2) (2013) 484–490. 28

[89] Q. Li, Y. Xuan, F. Yu, Experimental investigation of submerged single jet impingement using cu–water nanofluid, Applied Thermal Engineering 36 (2012) 426–433. 28

[90] B. P. Whelan, A. J. Robinson, Nozzle geometry effects in liquid jet array impingement, Applied Thermal Engineering 29 (11) (2009) 2211–2221. 28

[91] L. A. Brignoni, S. V. Garimella, Effects of nozzle-inlet chamfering on pressure drop and heat transfer in confined air jet impingement, International Journal of Heat and Mass Transfer 43 (7) (2000) 1133–1139. 28

[92] K. Jambunathan, E. Lai, M. Moss, B. Button, A review of heat transfer data for single circular jet impingement, International Journal of Heat and Fluid Flow 13 (2) (1992) 106 – 115. 28

[93] D. Sahoo, M. Sharif, Numerical modeling of slot-jet impingement cooling of a constant heat flux surface confined by a parallel wall, International Journal of Thermal Sciences 43 (9) (2004) 877 – 887. 30, 73, 81

[94] G. Masters, Spanwise velocity distributions in jets from rectangular slots, AIAA Journal 19 (2) (1981) 148–152. 31

[95] N. Chen, H. Yu, Mechanism of axis switching in low aspect-ratio rectangular jets, Computers & Mathematics with Applications 67 (2) (2014) 437–444. 32, 104

[96] H. Yu, S. S. Girimaji, Study of axis-switching and stability of laminar rectangular jets using lattice Boltzmann method, Computers and Mathematics with Applications 55 (7) (2008) 1611–1619. 32

[97] K. Kataoka, M. Suguro, H. Degawa, K. Maruo, I. Mihata, The effect of surface renewal due to largescale eddies on jet impingement heat transfer, International Journal of Heat and Mass Transfer 30 (3) (1987) 559–567. 33

[98] T. Iwana, K. Suenaga, K. Shirai, Y. Kameya, M. Motosuke, S. Honami, Heat transfer and fluid flow characteristics of impinging jet using combined device with triangular tabs and synthetic jets, Experimental Thermal and Fluid Science 68 (2015) 322–329. 33

[99] N. Gao, H. Sun, D. Ewing, Heat transfer to impinging round jets with triangular tabs, International Journal of Heat and Mass Transfer 46 (14) (2003) 2557–2569. 33, 34, 103, 107

[100] T. Hayashi, J. Taki, Y. Nakanishi, M. Motosuke, S. Honami, Experimental study on control of an impinging jet heat transfer using triangular tabs, Journal of Fluid Science and Technology 4 (2) (2009) 292–303. 33, 34

[101] K. B. Zaman, Streamwise vorticity generation and mixing enhancement in free jets by'delta-tabs', Vol. 106235, National Aeronautics and Space Administration, 1993. 34

[102] K. Zaman, Spreading characteristics of compressible jets from nozzles of various geometries, Journal of Fluid Mechanics 383 (1999) 197–228. 34, 37, 103

[103] H. Rahai, Near-field characteristics of wall jets with tabs, Ph.D. thesis, University of California, Irvine (2010). 34

[104] M. Samimy, M. Reeder, K. Zaman, Supersonic jet mixing enhancement by vortex generators, in: AIAA 27th Joint Propulsion Conference, no. AIAA-91-2261-CP, AIAA Meeting Papers, 1991. 34

[105] D. Violato, A. Ianiro, G. Cardone, F. Scarano, Three-dimensional vortex dynamics and convective heat transfer in circular and chevron impinging jets, International Journal of Heat and Fluid Flow 37 (2012) 22–36. 37

[106] K. Zaman, J. Bridges, D. Huff, Evolution from tabs to chevron technology-a review, International Journal of Aeroacoustics 10 (5-6) (2011) 685–710. 37

[107] B. Lindgren, A. V. Johansson, Design and evaluation of a low-speed wind-tunnel with expanding corners, Department of Mechanics, KTH, Report No. TRITA-MEK 14. 42, 44

[108] R. D. Keane, R. J. Adrian, Optimization of particle image velocimeters. i. double pulsed systems, Measurement science and technology 1 (11) (1990) 1202. 43

[109] TSI, Insight 4g- tutorial guide (June 2011). 43

[110] J. Stafford, E. Walsh, V. Egan, A statistical analysis for time-averaged turbulent and fluctuating flow fields using particle image velocimetry, Flow Measurement and Instrumentation 26 (2012) 1–9. 44, 67

[111] R. D. Mehta, P. Bradshaw, Design rules for small low speed wind tunnels, The Aeronautical Journal (1968) 83 (827) (1979) 443–453. 45

[112] K. Wieghardt, On the resistance of screens, Aeronautical Quarterly 4 (02) (1953) 186–192. 45

[113] K. Azar, B. Tavassoli, Qpedia Thermal Management – Electronics Cooling Book, Volume 3, Advanced Thermal Solutions, Incorporated, 2009.
URL https://books.google.ie/books?id=QeAQAPWyslMC 46

[114] Siemens, STAR-CCM+ User's Guide, Release 9.06, Siemens PLM, Plano, Texas, U.S. (2014). 49

[115] N. M. R. Jeffers, On the heat transfer and fluid mechanics of a normally-impinging, submerged and confined liquid jet, Ph.D. thesis, University of Limerick (2009). 53

[116] J. Stafford, E. Walsh, V. Egan, Characterizing convective heat transfer using infrared thermography and the heated-thin-foil technique, Measurement Science and Technology 20 (10) (2009) 105401. 54, 56

[117] J. Sanghera, S. Bayya, G. Villalobos, W. Kim, J. Frantz, B. Shaw, B. Sadowski, R. Miklos, C. Baker, M. Hunt, et al., Transparent ceramics for high-energy laser systems, Optical Materials 33 (3) (2011) 511–518. 55

[118] GoodFellow, Stainless Steel AISI 304 (Fe/Cr18/Ni10) Datasheet (2016). 55

[119] O. Raghu, J. Philip, Thermal properties of paint coatings on different backings using a scanning photo acoustic technique, Measurement science and technology 17 (11) (2006) 2945. 55

[120] J. Stafford, On the miniaturisation of convection cooling solutions applicable to portable electronic devices, Ph.D. thesis, University of Limerick (2009). 56

[121] S. Sargent, C. Hedlund, P. Ligrani, An infrared thermography imaging system for convective heat transfer measurements in complex flows, Measurement Science and Technology 9 (12) (1998) 1974. 57

[122] A. Waddell, J. Punch, J. Stafford, N. Jeffers, The heat transfer performance in a square channel downstream of a representative shape memory alloy structure for microfluidics applications, in: Thermal Measurement, Modeling & Management Symposium (SEMI-THERM), 2015 31st, IEEE, 2015, pp. 273–279. 57

[123] B. Munson, D. Young, T. Okiishi, W. Huebsch, Fundamentals of fluid mechanics, Wiley, 2009. 60

[124] S. J. Kline, F. McClintock, Describing uncertainties in single-sample experiments, Mechanical engineering 75 (1) (1953) 3–8. 64

[125] J. Holman, Experimental Methods for Engineers, McGraw-Hill series in mechanical engineering, McGraw-Hill, 2001. 65

[126] D. Forliti, P. Strykowski, K. Debatin, Bias and precision errors of digital particle image velocimetry, Experiments in Fluids 28 (5) (2000) 436–447. 67

[127] Y. Çengel, J. Cimbala, Fluid Mechanics: Fundamentals and Applications, Si Version, McGraw-Hill series in mechanical engineering, McGraw-Hill Education, 2006. 76, 88

[128] N. Jeffers, J. Stafford, C. Conway, J. Punch, E. Walsh, The influence of the stagnation zone on the fluid dynamics at the nozzle exit of a confined and submerged impinging jet, Experiments in Fluids 57 (2) (2016) 1–15. 79

[129] H. Martin, Heat and mass transfer between impinging gas jets and solid surfaces, Advances in heat transfer 13 (1977) 1–60. 80

[130] R. Shah, A. London, Thermal boundary conditions and some solutions for laminar duct flow forced convection, Journal of Heat Transfer 96 (2) (1974) 159–165. 82, 83

[131] F. P. Incropera, Liquid cooling of electronic devices by single-phase convection, Vol. 3, Wiley-Interscience, 1999. 86

[132] N. M. Jeffers, J. Punch, E. J. Walsh, M. McLean, Heat transfer from novel target surface structures to a normally impinging, submerged and confined water jet,

Journal of Thermal Science and Engineering Applications 1 (3) (2009) 031001. 86

[133] B. Schmandt, H. Herwig, Loss coefficients in laminar flows: essential for the design of micro flow systems, PAMM 11 (1) (2011) 27–30. 89

[134] M. Fabbri, A. Wetter, B. Mayer, T. Brunschwiler, B. Michel, H. Rothuizen, R. Linderman, U. Kloter, Microchip cooling module based on fc72 slot jet arrays without cross-flow, in: Semiconductor Thermal Measurement and Management Symposium, 2006 IEEE Twenty-Second Annual IEEE, IEEE, 2006, pp. 54–58. 98

[135] G. J. Michna, E. A. Browne, Y. Peles, M. K. Jensen, The effect of area ratio on microjet array heat transfer, International Journal of Heat and Mass Transfer 54 (9) (2011) 1782–1790. 98

[136] F. Incropera, Fundamentals of heat and mass transfer, no. v. 1 in Fundamentals of Heat and Mass Transfer, John Wiley, 2007. B2

Appendix A

A.1 Articles in Review

Sexton, A.*, Punch, J., Jeffers, N., & Stafford, J. (2017). **The thermal and hydrodynamic behaviour of confined, normally impinging laminar slot jets**. *International Journal of Heat & Mass Transfer*.

Sexton, A.*, Punch, J., Jeffers, N., & Stafford, J. (2017). **Passive control and enhancement of low Reynolds number slot jets through the use of tabs and chevrons**. *Journal of Heat Transfer*.

A.2 Published Work

Sexton, A.*, Punch, J., Jeffers, N., & Stafford, J. (2016). **Passive control and enhancement of low Reynolds number slot jets through the use of tabs and chevrons**. International Mechanical Engineering Congress & Exposition, Phoenix, AZ, November 13 - 17.

Jeffers, N.*, Stafford, J., Nolan, K., Donnelly, B., Enright, R., Punch, J., Waddell, A. M., Ehrlich, L., OConnor, J., Sexton, A., Blythman, R., & Hernon D. (2014). **Keynote Paper: Microfluidic Cooling of Photonic Integrated Circuits (PICS)**. Proc. 4th European Conf. on Microfluidics, Limerick, Ireland, December 10 – 12

Appendix B

B.1 Analysis of the Joule-heated foil technique

Once the heat transfer mechanisms present in the control volume detailed in Figure 3.12 were identified, a thermal resistance network was compiled and detailed in Figure B.1. As previously mentioned, the analysis was carried out with a single pixel captured by the IR camera ($\delta x = \delta y = 0.333mm$) for $Re_{Dh} = 100$ and the slot jet aspect ratio of 1 geometry. The thermal resistance to forced convection (R_{th-fc}) was determined using eq. (B.1), and found to be $\sim O(10^4$ °C/W).

$$R_{th-fc} = \frac{1}{h\Delta x^2} \tag{B.1}$$

The thermal resistance to lateral conduction between the foil elements was found using eq. (B.2). Where the area (A) is $\Delta x t_f$, the thermal resistance was found

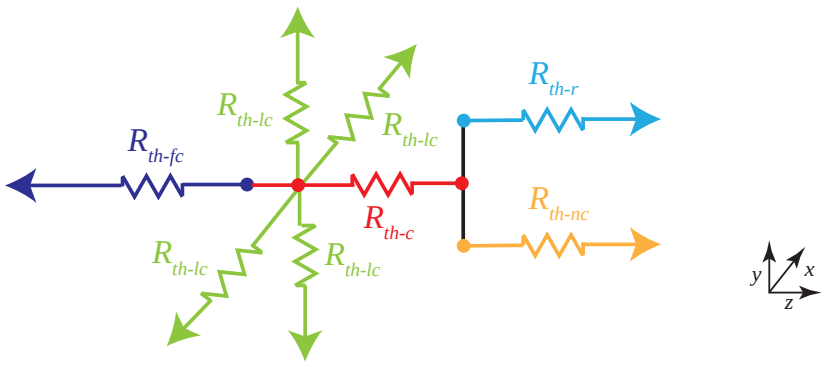

Figure B.1: Thermal resistance network for a single element in the Joule-heated foil analysis.

to be $\sim O(10^3$ °C/W).

$$R_{th-lc} = \frac{\delta x}{KA} \tag{B.2}$$

Equation (B.3) was used to determine the conduction along the Z axis through the foil (f), paint (p), and glass (g) layers:

$$R_{th-c} = \frac{1}{\Delta x^2}\left(\frac{t_f}{K_f} + \frac{t_p}{K_p} + \frac{t_g}{K_g}\right) \tag{B.3}$$

Where h_{nc} was the natural convection heat transfer coefficient (4.5 W/m^2K [71]), h_r was the radiation heat transfer coefficient [136], and the ambient (T_{amb}) and glass temperatures (T_g) were found to be 20°C and 30°C, respectively. Equations (B.4) and (B.5) were then applied to calculate the thermal resistance to natural convection and radiation to the surroundings:

$$R_{th-nc} = \frac{1}{hA_{nc}} \tag{B.4}$$

$$R_{th-r} = \frac{1}{h_r A} = \frac{1}{\varepsilon\sigma\Delta x^2(T_g + T_{amb})(T_g^2 + T_{amb}^2)} \tag{B.5}$$

In conclusion, the thermal resistance to lateral conduction was found to be one order of magnitude lower than that through forced convection and, therefore, it was included in the calculation of the convection heat transfer coefficient. The small temperature difference between elements, however, meant that this mode of heat transfer had a relatively low thermal potential and, thus, lateral conduction was included but had a negligible impact on the heat transfer coefficient.

Appendix C

C.1 Calibration certificates

CERTIFICATE OF CALIBRATION

Issued By
Calibration Specialists Ltd., Holland Rd., National Technology Pk., Castletroy, Limerick. Ireland.
Tel: +353 61 330333 - Fax: +353 61 330452 - website: www.calibrationspecialists.ie

Date of Calibration: 15TH JULY 2015 **Certificate No:** 1506152

Method:

Sources of known accuracy were applied to the input terminals of the meter.

DC CURRENT

Range (A)	Value (A)	Min (A)	Actual (A)	Max (A)	Uncertainty (±A)
40	39	38.6	39.2	39.4	0.01
400	390	386	389	394	0.1

AC CURRENT @ 1kHz

Range (A)	Value (A)	Min (A)	Actual (A)	Max (A)	Uncertainty (±A)
4	3.9	3.815	3.9	3.985	0.001
40	39	38.38	39.1	39.63	0.01
100	90	88.3	89.6	91.8	0.1
400	390	370.1	390	409.9	0.1

FREQUENCY

Range (Hz)	Value (Hz)	Min (Hz)	Actual (Hz)	Max (Hz)	Uncertainty (±Hz)
100	100.0	99.480	100.0	100.520	0.001

STANDARDS USED:

Asset No: 117 CALIBRATOR Cal Due: DEC - 2015

COMMENTS:

Upon receipt this unit was within the manufacturer's specification at all points tested.
No adjustments were nessecary.

----------End of Certificate----------

Figure C.1: Calibration certificate for the Tenma 72-6185 clamp meter (1 of 2).

CERTIFICATE OF CALIBRATION

Issued By
Calibration Specialists Ltd., Holland Rd., National Technology Pk., Castletroy, Limerick. Ireland.
Tel: +353 61 330333 - Fax: +353 61 330452 - website: www.calibrationspecialists.ie

Date of Calibration: 15TH JULY 2015 **Certificate No:** 1506152

Method:

Sources of known accuracy were applied to the input terminals of the meter.

DC CURRENT

Range (A)	Value (A)	Min (A)	Actual (A)	Max (A)	Uncertainty (±A)
40	39	38.6	39.2	39.4	0.01
400	390	386	389	394	0.1

AC CURRENT @ 1kHz

Range (A)	Value (A)	Min (A)	Actual (A)	Max (A)	Uncertainty (±A)
4	3.9	3.815	3.9	3.985	0.001
40	39	38.38	39.1	39.63	0.01
100	90	88.3	89.6	91.8	0.1
400	390	370.1	390	409.9	0.1

FREQUENCY

Range (Hz)	Value (Hz)	Min (Hz)	Actual (Hz)	Max (Hz)	Uncertainty (±Hz)
100	100.0	99.480	100.0	100.520	0.001

STANDARDS USED:

Asset No: 117 CALIBRATOR Cal Due: DEC - 2015

COMMENTS:

Upon receipt this unit was within the manufacturer's specification at all points tested.
No adjustments were nessecary.

----------End of Certificate----------

Figure C.2: Calibration certificate for the Tenma 72-6185 clamp meter (2 of 2).

CERTIFICATE OF CALIBRATION

Issued By
Calibration Specialists Ltd., Holland Rd., National Technology Pk., Castletroy, Limerick. Ireland.
Tel: +353 61 330333 - Fax: +353 61 330452 - website: www.calibrationspecialists.ie

An INAB Accredited Calibration Laboratory Reg No.001C

Certificate No: 1507004

Date of Issue: 13TH JULY 2015

Approved Signatory:

Timmy Davern (Head of Laboratory.)
Tony O'Mara(Technical Manager.)

Category: A - C.S.L, CO. LIMERICK

Customer: UNIVERSITY OF LIMERICK

Address: CO. LIMERICK

Details Of Unit Calibrated:

Manufacturer:	FLUKE	**Date Received:**	6TH JULY 2015
Model:	45	**Date Calibrated:**	10TH JULY 2015
Serial No:	7594003	**Calibrated By:**	MICHAEL KENNEDY
Ref No:	N/A	**Temperature:**	(23± 5) ºC
Description:	DUAL DISPLAY DIGITAL MULTIMETER	**Humidity:**	(50±25) %

The above instrument was tested against the manufacturer's accuracy specification at the points shown and the results are tabulated in the following report. This report relates solely to the instrument described above.

This certificate is issued in accordance with the conditions of accreditation laid down by the Irish National Accreditation Board, which has assesed the measurement capability of the Laboratory. The reported results are traceable to recognised National and International standards. The copyright of this report is reserved to Calibration Specialists Limited (CSL) and it shall not be used either in whole or in part for the purposes of advertising, publicity, litigation or otherwise without the prior consent of CSL. This calibration certificate contains information belonging to Calibration Specialists Ltd.,which is confidential and/or legally privileged. Information is intended only for the use of the entity named above. If you have received this certificate in error,please notify us by telephone immediately at the above number.

The reported expanded uncertainty is stated as the standard uncertainty of measurement multiplied by the coverage factor k=2, which for a normal distribution corresponds to a coverage probability of approximately 95%. The standare uncertainty of measurement has been determined in accordance with EAL Publication EA-4/02.

Figure C.3: Calibration certificate for the Fluke 45 multimeter (1 of 2).

CERTIFICATE OF CALIBRATION

Issued By
Calibration Specialists Ltd., Holland Rd., National Technology Pk., Castletroy, Limerick. Ireland.
Tel: +353 61 330333 - Fax: +353 61 330452 - website: www.calibrationspecialists.ie

Date of Calibration: 10TH JULY 2015 **Certificate No:** 1507004

Method: The unit under test was first allowed to stabilise. Precisely known values were then applied to the input of the unit under test and the resultant readings compared against manufacturer's specifications. The Manufacturer Published Performance Test Procedure is carried out in reference to the Fluke 45 Dual Display User Manual P/N 855981 Rev.2, 12/89 published in 1989.

DC Voltage Test

Range (V)	Value (V)	Min (V)	Actual (V)	Max (V)	Uncertainty (±V)
(slow) 100 m	Short	-0.006 m	0.002 m	0.006 m	0.0005 m
	90 m	89.971 m	89.981 m	90.029 m	0.004 m
(slow) 1000 m	900 m	899.71 m	899.79 m	900.29 m	0.02 m
300 m	Short	-0.02 m	0.00 m	0.02 m	0.005 m
	300 m	299.90 m	299.95 m	300.10 m	0.01 m
3	3	2.9990	2.9994	3.0010	0.0001
	-3	-3.0010	-2.9992	-2.9990	0.0001
30	30	29.990	29.994	30.010	0.001
300	300	299.90	299.94	300.10	0.01
1000	1000	999.5	999.7	1000.5	0.1

AC Voltage Test

Range (V)	Value (V)	Min (V)	Actual (V)	Max (V)	Uncertainty (±V)
300 m	#Short	-0.75 m	0.19 m	0.75 m	0.005 m
	15m, 1kHz	14.87 m	15.01 m	15.13 m	0.01 m
	15m, 100kHz	13.75 m	14.14 m	16.25 m	0.02 m
	300m, 1kHz	299.30 m	300.01 m	300.70 m	0.05 m
	300m,100kHz	284.50 m	293.08 m	315.50 m	0.07 m
3	3, 1kHz	2.9930	3.0002	3.0070	0.0005
30	30, 1kHz	29.930	30.002	30.070	0.005
300	300, 1kHz	299.30	300.01	300.70	0.09
750	750, 1kHz	747.5	750.0	752.5	0.3

DC Current

Range (A)	Value (A)	Min (A)	Actual (A)	Max (A)	Uncertainty (±A)
30 m	30.000 m	29.982 m	**FAULTY** m	30.018 m	0.007 m
100 m	90.00 m	89.93 m	**FAULTY** m	90.07 m	0.007 m
10	1.900	1.891	1.899	1.909	0.001

Figure C.4: Calibration certificate for the Fluke 45 multimeter (2 of 2).

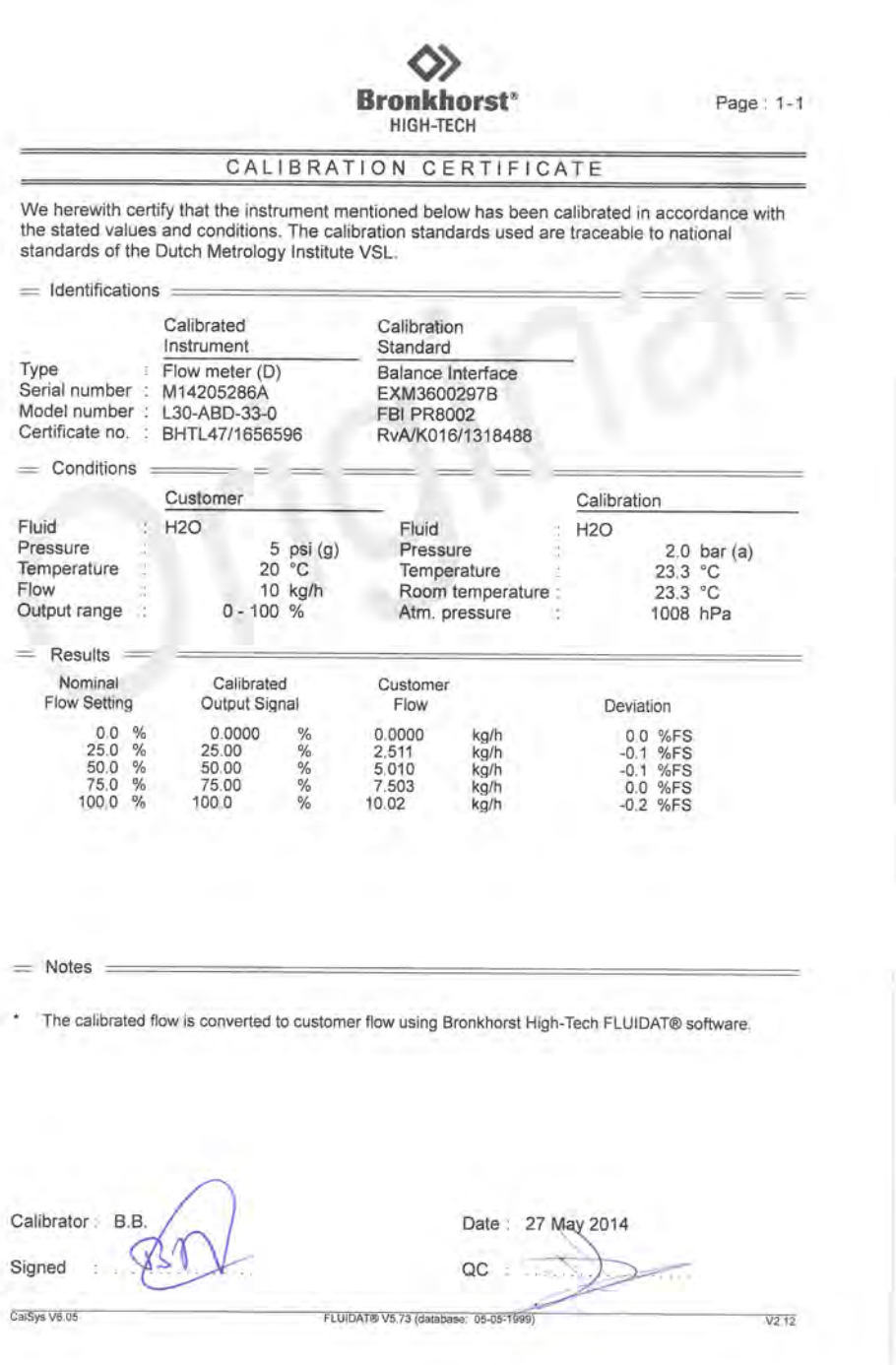

Bronkhorst®
HIGH-TECH

Page : 1-1

CALIBRATION CERTIFICATE

We herewith certify that the instrument mentioned below has been calibrated in accordance with the stated values and conditions. The calibration standards used are traceable to national standards of the Dutch Metrology Institute VSL.

Identifications

	Calibrated Instrument	Calibration Standard
Type	Flow meter (D)	Balance Interface
Serial number	M14205286A	EXM3600297B
Model number	L30-ABD-33-0	FBI PR8002
Certificate no.	BHTL47/1656596	RvA/K016/1318488

Conditions

	Customer		Calibration	
Fluid	H2O	Fluid	H2O	
Pressure	5	psi (g)	2.0	bar (a)
Temperature	20	°C	23.3	°C
Flow	10	kg/h	23.3	°C
Output range	0 - 100	%	1008	hPa

Results

Nominal Flow Setting		Calibrated Output Signal		Customer Flow		Deviation	
0.0	%	0.0000	%	0.0000	kg/h	0.0	%FS
25.0	%	25.00	%	2.511	kg/h	-0.1	%FS
50.0	%	50.00	%	5.010	kg/h	-0.1	%FS
75.0	%	75.00	%	7.503	kg/h	0.0	%FS
100.0	%	100.0	%	10.02	kg/h	-0.2	%FS

Notes

* The calibrated flow is converted to customer flow using Bronkhorst High-Tech FLUIDAT® software.

Calibrator : B.B.

Date : 27 May 2014

Signed : . . . . . .

QC : . . . . . .

CalSys V6.05 FLUIDAT® V5.73 (database: 05-05-1999) V2.12

Figure C.5: Calibration certificate for the Bronkhurst Liqui-Flow mass flow meter.

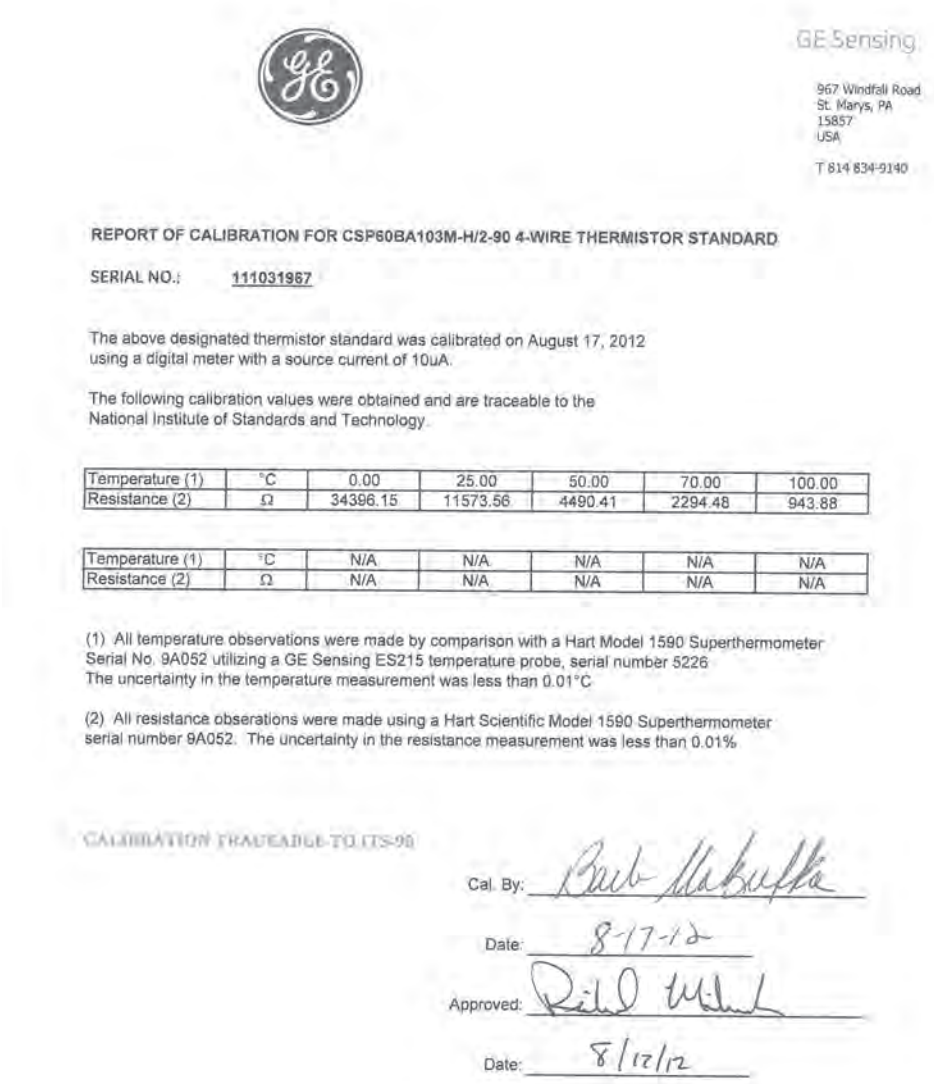

GE Sensing

967 Windfall Road
St. Marys, PA
15857
USA

T 814 834-9140

REPORT OF CALIBRATION FOR CSP60BA103M-H/2-90 4-WIRE THERMISTOR STANDARD

SERIAL NO.: 111031967

The above designated thermistor standard was calibrated on August 17, 2012 using a digital meter with a source current of 10uA.

The following calibration values were obtained and are traceable to the National Institute of Standards and Technology.

Temperature (1)	°C	0.00	25.00	50.00	70.00	100.00
Resistance (2)	Ω	34396.15	11573.56	4490.41	2294.48	943.88

Temperature (1)	°C	N/A	N/A	N/A	N/A	N/A
Resistance (2)	Ω	N/A	N/A	N/A	N/A	N/A

(1) All temperature observations were made by comparison with a Hart Model 1590 Superthermometer Serial No. 9A052 utilizing a GE Sensing ES215 temperature probe, serial number 5226 The uncertainty in the temperature measurement was less than 0.01°C

(2) All resistance obserations were made using a Hart Scientific Model 1590 Superthermometer serial number 9A052. The uncertainty in the resistance measurement was less than 0.01%

CALIBRATION TRACEABLE TO ITS-90

Cal. By: Barb Mabuffa

Date: 8-17-12

Approved: Richard Mitchell

Date: 8/17/12

Figure C.6: Calibration certificate for the Fluke 1504 Thermistor Probe.